

DEVELOPMENT OF A MULTIPLEXED CONFOCAL FLUORESCENCE  
LIFETIME IMAGING MICROSCOPE FOR SCREENING  
APPLICATIONS

Ph.D. Thesis - Nehad Hirmiz

McMaster University – Biomedical Engineering

DEVELOPMENT OF A MULTIPLEXED CONFOCAL FLUORESCENCE  
LIFETIME IMAGING MICROSCOPE FOR SCREENING  
APPLICATIONS

By

Nehad Hirmiz

A Thesis

Submitted to the School of Graduated Studies

In Partial Fulfillment of the Requirements for the Degree

Doctor of Philosophy

McMaster University

© Copyright by Nehad Hirmiz, December 2019

DOCTOR OF PHILOSOPHY (2019)  
School of Biomedical Engineering

McMaster University  
Hamilton, Ontario

TITLE:                   Development of a Highly Multiplexed Confocal  
Fluorescence Lifetime Imaging Microscope for  
Screening Applications

AUTHOR:               Nehad Hirmiz, McMaster University

SUPERVISOR:         Qiyin Fang, Ph.D.

NUMBER OF PAGES:   xiv, 94

## Lay Abstract

Inside a cell, proteins are the “workers” and they interact with each other, doing that work. Many of these interactions are important for the cell to live. Pharmaceutical companies may design drugs that can interfere with a specific interaction in order to cause an effect in the cell. Scientists are interested in measuring these interactions and we can do this by “taking a picture” of the interaction using a specialized microscope. One of the major issues with these microscopes is that it takes scientists a long time to collect pictures of these interactions. This means only a few drugs can be tested in a day. To speed up the drug discovery and testing we want to design faster microscopes that can test hundreds of drugs in a day. In my thesis I contributed to building a state-of-the-art super fast microscope. We made progress in steps, and by the third attempt we successfully measured interactions in cells in seconds! Our new microscope is ~400x faster than current technologies. We hope that this research will be useful to speed up drug discovery in the future.

## Abstract

Protein-protein interactions are important for biological processes. Therefore, many small molecules target a specific protein or interaction in the cell to have biological consequence. While we can measure some protein-protein interactions in a test tube, many proteins cannot be purified making it difficult to properly test that a drug is “on target”. An alternative is to measure these interactions in live cells. We express the proteins of interest fused to fluorophores allowing the use of fluorescence techniques. Förster Resonance Energy Transfer (FRET) provides a molecular level ruler to measure the distance, within a few nanometers, between two proteins. FRET indicates binding. The gold standard for measuring FRET in live cells is by quantifying changes in fluorescence lifetime using Fluorescence lifetime imaging microscopy (FLIM). The change in fluorescence lifetime is inversely proportional to the ratio of bound to non-bound proteins. Tradition FLIM-FRET microscopy is too slow for screening applications. Our aim was to develop a highly multiplexed confocal system for rapid FLIM-FRET acquisition.

We present the development of multiple prototypes for confocal multiplexing. In this work, our final design includes  $32 \times 32$  multiplexed excitation points which scan the sample using refractive window scanners. We coupled this excitation scheme to a  $64 \times 32$  time-gated single-photon avalanche photodiode (SPAD) sparse array detector. This multiplexed setup allows the use of the sparse array with high frame rate and sub-nanosecond time-gating to achieve high throughput FLIM acquisition. Using our multiplexed FLIM prototype we measured Bcl-2 family protein-protein interactions in live cells ( $310 \times 310 \mu\text{m}$  FOV) with two-channel confocal FLIM in 1.5 s. Protein binding affinities were estimated by measuring the changes in FRET as a function of acceptor to donor ratio. The resulting speed of this system meets requirements for implementation in screening applications.

## Acknowledgements

During my Ph.D. journey at McMaster University, I had the privilege of meeting and working with some of the most brilliant scientists and engineers. Their passion, kindness and support never failed to inspire and motivate me to carry on.

I am grateful to my Ph.D. supervisor, Dr. Qiyin Fang, for his guidance, patience, thoughtfulness and for providing me with many opportunities during my time in his lab. It was an honour and a pleasure being one of your students. I am certain that our collaboration will last a lifetime.

I would also like to thank my committee members Dr. David W Andrews, Dr. Joseph E Hayward, Dr. Richard Berman, Dr. Cécile Fradin, and Dr. Ray Truant for their insightful discussions during each project meeting. Special thanks to Dr. David W. Andrews for welcoming me into his lab and providing me with a nurturing collaborative environment.

I would like to express my deepest thanks to my colleague and mentor, Dr. Anthony Tsikouars for being an amazing role model and for many laughs during the long hours building optical instruments.

I would like to thank all my colleagues at the Biophotonics Lab and the DWA Lab for their helpfulness, care and team spirit. It is thanks to them that I had amazing years of research experience. Special thanks to Jessica Kun and Morgan Richards for their helpful discussions and editing my manuscripts.

To my amazing co-author, partner and wife Elizabeth J. Osterlund. Meeting you was my greatest achievement. You are the best energy ‘donor’ that ever excited me. Your resonating love will always make me shine so bright.

I would love to thank my parents, my siblings and my close family members for their love, prayers and support. This was your journey and your achievement as well. I could not have done this without your encouragement.

And finally, thanks to McMaster University for accepting me to their scientific playground. I am always grateful to live in Canada, a haven for scientists like me to pursue their dreams and change the world.

# Table of Contents

Lay Abstract	iv
Table of Contents	vii
List of Abbreviations	ix
List of Figures	x
Chapter 1. Introduction	1
1.1 Motivation	1
1.2 Proposed Solution	1
1.4 Contributions	3
Chapter 2. Background	6
2.1 Bcl-2 family proteins and their role in regulating cell death	7
2.2 FRET for measuring protein-protein interactions	10
2.4 Confocal FLIM imaging and protein-protein binding affinities	17
2.5 Engineering solutions for faster confocal TD-FLIM	20
2.6 Multiplexed Confocal FLIM Systems for Screening Applications	22
2.7 Next generation detectors for multiplexed confocal FLIM	26
Chapter 3. Synchroscan Streak System	33
Introduction to paper	34
Contents of Paper I	35
Abstract	35
3.1 Introduction	35
3.2 Experimental design	36
3.3 Image processing and Lifetime estimation	39
3.4 Multiplexing FLIM with streak camera	42
3.5 Discussion and conclusion	45
References	48
Chapter 4. Multiplexed Confocal System	52
Introduction to paper II	53
Contents of Paper II	54
Abstract	54
4.1 Introduction	54

4.2 Optical Setup	56
4.3 Results and Discussion	57
References	62
Chapter 5. Multiplexed Confocal FLIM System	65
Introduction to paper III	66
Contents of Paper III	67
Abstract	67
5.1 Introduction	67
5.2 Results	69
5.3 Materials and Methods	77
5.4 Discussion	80
References	82
Chapter 6. Conclusions and Future Work	86
6.1 Summary	86
6.1 System Resolution – Theoretical and Experimental Consideration	87
6.3 Additions Needed to Make the System Screen Ready	88
References	95
Appendix A - Coupling dynamic segmentation with the phasor approach of lifetime estimation for fast and quantitative analysis of large FLIM-FRET datasets	98
Appendix B – Effect of photobleaching on fused mCerulean3 fluorescent protein in live cells	102
Appendix C – Properties of Refractive Window Scanners	105

## List of Abbreviations

1D	one dimensional
2D	two dimensional
Bcl-2	B-cell lymphoma 2
BH	Bcl-2 homology
BMK	baby mouse kidney
CCD	charge coupled device
CMOS	complementary metal oxide semiconductor
CSU	Confocal spinning unit
DCR	dark count rate
FCS	fluorescence correlation spectroscopy
FD	frequency domain
FHS	FLIM Hyperspectral
FLIM	fluorescence lifetime imaging microscopy
FRAP	fluorescence recovery after photobleaching
FRET	Förster resonance energy transfer
galvo	galvanometer
GFP	green fluorescent protein
HCS	high content screening
ICCD	intensified CCD
IRF	instrument response function
MBD	membrane binding domain
MCP	multichannel plate
MLA	microlens array
MOM	mitochondrial outer membrane
MOMP	mitochondrial outer membrane permeabilization
NA	numerical aperture
PDE	photon detection efficiency
PLL	phased-locked loop
PMT	photomultiplier tube
PPI	protein-protein interaction
SNR	signal to noise ratio
SPAD	single-photon avalanche diode
TAC	time-to-amplitude converter
TCSPC	time correlated single photon counting
TD	time domain
TWMC	tilt window multiplexing confocal
USB	universal serial bus
WF	widefield

## List of Figures

- 2.1 *Diagram of Bcl-2 family homology domains.* Proteins (named in bold) are represented by a line, where boxes along the line show Bcl2 homology (BH) domains 1-4 and the Membrane Binding Region (MBR). To the left of this figure, the structural classification (multi-domain or BH3 only) as well as functional classification (*italics*) is indicated. This figure was modified from [14]. 9
- 2.2 **Figure 2.** *Schematic depiction of electron vibrational energy states that can occur during FRET.* A donor molecule gets excited to the higher electronic energy state through photon absorption (purple arrow). The molecule can relax to the excited state by emitting a photon. In the presence of a nearby molecule a non-radiative energy transfer can take place between the ‘donor’ and the ‘acceptor’. The excitation energy of the acceptor must be equal to the energy difference between the excited state and the ground state for the donor. 11
- 2.3 *Spectral emission and excitation profiles for mCerulean3 and Venus.* Purified mCerulean3 and Venus proteins (1  $\mu$ M) used to measure spectra on a Tecan microplate reader in a 96 well quartz plate. mCerulean3 excitation was measured with emission at 515 nm, and mCerulean3 emission was measured with a fixed excitation at 440 nm. Venus excitation was measured with emission at 550 nM and Venus emission was measured with a fixed excitation wavelength of 520 nm. Background from buffer alone was subtracted, and raw data was normalized to the maximum for each spectral. 12
- 2.4 *Bcl-XL binding to Bad in live baby mouse kidney (BMK) cells.* (top) FD Wide field FLIM images acquired on a LIFA FLIM instrument. (bottom) TD confocal FLIM images acquired on our multiplexed confocal setup using time gated SPAD array (Chapter 4). Donor is mCerulean3 fused to Bcl-XL, and this protein is stably expressed in all BMK cells (left panel). Venus-Bad is transiently transfected into some cells (middle panel). Binding of Bcl-XL to Bad can be seen by change in lifetime (Right panel). Lifetime is represented on a pseudocolor scale. 16

- 2.5 **Figure 5.** *Example of fluorescence lifetime imaging used to measure binding between two Bcl-2 proteins.* (left) Bcl-XL labelled using a cyan fluorescent protein (mCerulean3). (middle) Bad labelled with a yellow fluorescent protein variant (Venus). These images were acquired on the ISS-Alba single point confocal microscope. 100×100 field of view (256×256 pixels) acquired using 0.5 ms pixel dwell time. The total acquisition time was 32s. The lifetime image was generated using a 7×7 nearest neighbour binning to reconstruct well sampled decays. Each decay was fit to a single exponential curve to estimate the lifetime. 17
- 2.6 *A schematic depicting how the average lifetime changes as a function of the acceptor to donor ratio.* 2 proteins of interest are represented by the red and yellow shapes. Donor (blue pentagon) is fused to one protein of interest, and acceptor (green circle) is fused to another. Each large oval represents a confocal volume containing a number of donor- and acceptor-fusion proteins, and below each is the corresponding calculation of average lifetime. Unbound lifetime in this theoretical model is 3.8ns whereas bound lifetime (FRET) is 3.0ns. 19
- 2.7 *Schematic representation of the parallelized TCSPC detector in the INO-FHS microscope.* A set of 8 silver mirrors (black rectangles) are used to divide the collected fluorescence signal across 8 SPADs, controlled by a single TCSPC card. 21
- 2.8 *Schematic for the spinning disk confocal FLIM system.* This diagram was copied from Grant et al., [ref]. This system included a pulsed white laser source, with a diffraction gradient to select the excitation wavelength. The excitation multiplexing was achieved using the CSU-19 Nipkow disk scan(right), which was coupled to the Olympus 1X81 microscope (not shown). FLIM imaging was performed using a photocathode gated optical image intensifier (GOI) coupled to a scientific grade CCD camera. Rapid FLIM imaging can be achieved with this system using only two time-gates (1 nanosecond gate width, not shown). 24
- 2.9 *Schematic of our multiplexed approach using microlens arrays and refractive window scanners.* MLAs are used to create a foci array, focused at the conjugate plane of the side port of an inverted fluorescence microscope. The foci array can be shifted along the x and y axes using a pair of refractive window scanners [52]. The collected fluorescence signal is de-scanned and relayed to a second MLA to recreate the fluorescence image collected from the sample. 25

- 3.1 (a) Optical setup of the multifocal confocal streak system. (b) Schematic illustrating inward (left) and outward (right) scanning modes. The generated streaks in both modes are illustrated above, with a blue-red pseudoscale (left) representing intensity of generated streaks in that image. The sinusoidal sweeping voltage profile is shown below each image; black and white triangles indicate the start of the streaks from alternating fibers, blue and red lines indicate the near-linear section of the sweep profile, which is used to generate the streaks in the above image. The black and white arrows in the image above correspond to arrows indicated on the sinusoidal profile below 37
- 3.2 (a) Normalized intensity map of a single streak. The black line shows the normalized intensity profile of the maximum intensity point on the streak perpendicular to the sweeping direction. The red dashed lines indicate the positions of the two adjacent streak to the central streak in inward scanning mode. The cyan solid lines indicate the positions of two streaks adjacent to the central streak in the outward scanning mode. This profile is used to determine the crosstalk as a function of distance away from the streak (in pixels). (b) Examples indicating corresponding location of the streaks of interest (yellow arrow) and the adjacent streaks (red dash lines and cyan solid lines). Pixel size: 6.5  $\mu\text{m}$  39
- 3.3 (a) Left and right sweep time maps generated by interpolating the simulated grid using a delay generator. (b) Lag time map generated by taking each map and subtracting the time axis for the central horizontal line. Transient time asymmetry is observed when comparing the left map to the right map. Pixel size: 6.5  $\mu\text{m}$  41
- 3.4 (a) Sample streaks for quenched fluorescein (IRF), Coumarin-6 and Fluorescein are shown above. Corresponding linearized lifetime decays for the average of several of these streaks is plotted below. The IRF has a second hump, which is a characteristic of the pulsed diode laser operated at high power [26]. These humps were excluded from the delay experiments used to generate the time maps. (b) Fluorescence lifetime image of Coumarin-6 and Fluorescein solutions. Images were acquired at room temperature using a 10 $\times$ 10 confocal scan. The dark squares are a result of dead fibers and were excluded from the analysis. 43
- 3.5 Confocal images for live MCF-7 cells expressing mCerulean3-Bcl-XL. Images of the same sample were acquired using our multiplexed streak system (left), compared images acquired on an ISS-Alba in single point confocal mode (middle) and wide field mode (right). Dark squares in the streak image indicate the positions of the dead fibers, mentioned in Fig. 4. Scalar bar: 15  $\mu\text{m}$ . 44
- 3.6 Intensity weighted lifetime maps generated by fitting extracted lifetimes from data acquired on the streak microscope. Scalar bar: 15  $\mu\text{m}$ . (a) Confocal FLIM images of *Convallaria* and (b) live MCF-7 cells expressing mCerulean3-Bcl-XL. 3 $\times$ 3 binning was used for the *Convallaria* FLIM cube, while 7 $\times$ 7 binning was used for the MCF-7 FLIM cube. 45

4.1	The Multifocal Confocal. (a) Schematic diagram of our multiplexed confocal system attached to a microscope equipped with spinning disk unit. (b) Diagram illustrating multiplexed scanning in our Multifocal Confocal setup. Each red circle represents an excitation spot, and the dotted line is the path each spot takes when scanning the sample. Only 4x4 spots are shown for simplicity. (c) Illustration of how confocal scanning is performed in a spinning disk. The square grid indicates the imaging field of view determined by the size of the dense pixel detector. (d) Sample image of live cells scanned obtained on the system by the tilt window scanner.	57
4.2	Confocal imaging of fixed <i>Convallaria</i> slide in Multifocal Confocal and spinning disk unit. Different areas of the same fixed <i>Convallaria</i> slide were imaged (a-c). The full image for each is shown to the left. A 30x30 $\mu\text{m}$ area, from each image, is enlarged to the right, with the corresponding line intensity profile. For (a) and (c) the intensity measured in arbitrary units while the SPAD detector measures single photon counts (b). We used the Multifocal Confocal with Ximea CMOS camera (a) and with an SPC3 SPAD detector(b). In (c) we used the Spinning disk confocal. All scale bars are set to 30 $\mu\text{m}$	60
4.3	(a) Confocal image of live MCF-7 cells expressing mCerulean3-Bcl-XL. Field of view is 240x240 $\mu\text{m}$ scanned in 30x30 steps (960x960 pixels), in 500ms total scan time (550 $\mu\text{s}$ pixel dwell time). (b) An enlarged version of the indicated region of interest in (a). Scale bars are set to 30 $\mu\text{m}$	61
5.1	The Multifocal Confocal FLIM Setup. Schematic diagram of our multiplexed confocal system attached to an inverted commercial microscope	71
5.2	Time-gates position and size. Normalized profile IRF (black) and Fluorescein in 0.1 mM NaOH (red). For rapid lifetime imaging, we choose two time-gates (TG0 and TG1). The position of the two 4ns time-gates is also indicated above the time axis. The permitted observation window for the SPC3 is 16 nanoseconds presented as the time axis limits.	72
5.3	Lifetime maps of (a) Fluorescein in 0.1 M NaOH, 10 $\mu\text{M}$ , (b) Coumarin6 in ethanol 10 $\mu\text{M}$ . (c) Histogram of both lifetime maps.	73
5.4	Photon weighted FLIM confocal image of <i>Convallaria</i> . Scale bar 30 $\mu\text{m}$ .	73
5.5	FLIM imaging of FRET Controls. Lifetime maps of HEK293 expressing mCerulean3 fluorescent protein only (a), mCerulean3 and Venus together (b), and mCerulean3 tethered to Venus using a 13 amino-acids linker (c). (d) shows the lifetime distribution of the three FOVs. The presented maps in (a,b and c) represent a 78x78 $\mu\text{m}$ cropped regions of the full FOVs (310x310 $\mu\text{m}$ )	74

- 5.6 Confocal FLIM imaging of live MCF-7 stably expressing mCerulean3-BclXL. 75  
The top panel shows a zoomed region of cells transiently transfected with Venus-Bad (positive binding control). The bottom panel also shows a magnified region of cells transiently transfected with Venus-Bad2A (negative binding control). In the left panel we see the confocal image for the mCerulean3 channel. In the middle, we see confocal images for the Venus channel. The photon weighted FLIM image of the mCerulean3 is shown in the right panel. The fluorescence lifetime decreases (cells appear in red) when FRET is observed.
- 5.7 Binding information extracted from FLIM FRET images for positive and 76  
negative binding controls. (left) Acceptor to donor ratio image constructed by dividing acceptor intensity over donor intensity. (center) FRET efficiency map calculated from the lifetime image by comparing to the lifetime of mCerulean3-Bcl-XL without any acceptor. (right) plot of FRET efficiency vs acceptor:donor ratio obtained by plotting the non-zero pixels from FRET efficiency maps(center) and acceptor:donor maps(left) . A rapid increase in FRET efficiency, for the negative binding control, is caused by cells overexpressing Venus-Bad2A (red circle). The blue circle highlights the region where acceptor: donor ratio information is not acquired for a single FOV. The dots with bar are the average and standard deviation for the FRET efficiency at different Acceptor to Donor ratio bins
- 5.8 Effect of two Bcl-2 inhibitors (Abbvie ABT263 and A1331852) on 77  
binding between Bcl-XL and Bad. The binding curves were generated by binning data from 4 FOVs. The data points are averages obtained from each bin. The error bars represent the standard error. Each binding curve is fit a single site Hill equation (solid lines) to estimate the apparent  $K_d$ . The untransfected well was treated with dilution media (DMSO) used for the drugs to ensure that the media does not change the lifetime of the donor.

## List of Tables

2.1	<i>A comparison among three different commercial systems that use a single point confocal FLIM to image biological samples. The shown parameters are for images composed of 256×256 pixels.</i>	22
2.2	<i>Comparison of highly multiplexed confocal FLIM setups</i>	26
2.3	<i>Example fluorescence lifetimes of different classes of fluorophores. Modified from [53]</i>	27
4.1	Comparison of multiplexed confocal systems	55



# Chapter 1. Introduction

## 1.1 Motivation

Proteins have critical roles within the cell, often interacting in large networks or pathways to carry out a biological function. At one point in time, scientists believed it would not be possible to develop a drug that could specifically bind to and target a protein-protein interaction (PPI) [1]. Better understanding the mechanism of a drug can help clinicians predict and reduce side effects to improve therapeutic outcome. Advancements in biochemical methods, such as protein crystallography, combined with screening platforms and bioinformatics have now made this a reality. Drugs that target specific PPIs have been shown to have tremendous potential in variety of therapeutic treatments, such as oncology [2], cancer immunotherapy [3], infectious diseases [4], and neurological disorders [5]. Many of these compounds are designed based on the structure of the target protein's natural binding partner. The approval of the first Bcl-2 inhibitor ABT-199 for the treatment of chronic lymphocytic leukemia in 2016, marked a milestone for PPI targeted therapies. ABT-199 was realized after screening many variations of compounds that were designed to mimic Bad (another Bcl-2 family member) [6].

To claim that a small molecule targets a specific protein or protein-protein interaction, researchers must demonstrate competition with the native binding partner or direct binding to the target protein. However, measuring PPIs are challenging to model in a test tube due to purification difficulties. As we review in detail in our introduction, Fluorescence lifetime imaging microscopy (FLIM) for measuring Förster resonance energy transfer (FRET) offers an alternative to measure full length protein-protein interactions inside the cell. FLIM-FRET is not yet used for drug screening because this technique is extremely time consuming. On currently available instruments, only a few compounds can be tested in a workday. Thus, to make screening a possibility, our goal is to design an instrument for rapid FLIM-FRET data acquisition.

## 1.2 Proposed Solution

In commercial most systems, a single confocal point is scanned across a sample and the resulting signal is collected in a single detector. Therefore, increasing the number of excitation points and/or increasing the number of detectors can drastically increase the scanning speed. This is referred to as confocal multiplexing. The most commonly used multi-point confocal scanner is the Nipkow spinning disk [7], which does perform rapid confocal imaging but requires an intensified CCD detector (a dense pixel camera) [8,9]. The intensified CCD has low spatial and temporal resolution, low photon detection efficiency and high noise [10]. Thus, these systems are fast but limited in their application and accuracy. Here we built a highly multiplexed system that can be coupled to any

detector, including state of the art single photon avalanche detectors for high temporal resolution.

In our design, the number of excitation spots ( $32 \times 32$ ) is matched by the same number of time-resolved detectors. We use a microlens array (MLA) to create a 2D array of excitation beams. Scanning is achieved by using a pair of refractive windows to move each beam across a small region of the sample. The fluorescence signal is collected back onto a fixed 2D array of points (de-scanned). We demonstrate two different detection schemes; the collected signal can be relayed to a streak camera using a 2D fibre array (fibre core serves as the confocal pinhole), or directly coupled to a sparse array sensor (pixel aperture serves as the confocal pinhole). The final confocal image is reconstructed by stitching the scanned subregions together. This multiplexing scheme serves as an attachment that can be added to most commercially available microscopes. Using our third prototype, we can acquire a single FLIM image in less than a second, demonstrating the applicability of our solution for screening applications.

### 1.3 Thesis organization

The **Introduction** provides motivation and proposed solution for developing a multiplexed confocal FLIM system suitable for screening applications.

**Chapter 2** presents the Bcl-2 family proteins, which are used in this work to demonstrate our system. Bcl-2 protein-protein interactions are targeted by cancer therapeutics called BH3 mimetics. FLIM-FRET is the best method for measuring PPIs in live cells. Chapter 2 reviews the fundamentals of FRET and FLIM. The limitations of single point confocal TCSPC systems are discussed. Multiplexed solutions used to overcome the TCSPC limit are presented. Finally, the pros and cons of new single photon avalanche photodiode (SPAD) array detectors are summarized.

**Chapter 3** presents our second prototype which uses a  $10 \times 10$  multipoint excitation array. This system includes a 2D-1D fibre array to couple to a synchroscan streak camera. Two operation modes with different levels of cross-talk are presented. A novel calibration method to correct for transient time effects is presented. Our approach can be used to measure the asymmetry in the transient time effect as a function of sweeping direction. The system's performance is assessed. We imaged standard fluorescence dyes, fixed *Convallaria*, and Live MCF-7 cells expressing fluorescently labelled Bcl-XL (Bcl-2 family member). We conclude that further improvements to our system are required to reach speeds required for screening applications.

**Chapter 4** presents our third prototype with extended multiplexing ( $32 \times 32$  multipoint excitation array). This prototype is coupled to a dense CMOS sensor and SPAD array, to

perform confocal scanning. The quality of the images obtained in our system are compared to those acquired on a spinning disk confocal unit.

**Chapter 5** provides a proof of concept for using our third prototype to do rapid confocal FLIM imaging for screening applications. The system calibration and determination of the optimal position and size of time-gates are presented. FRET standards were used to ensure that the system can accurately measure changes in lifetime due to FRET. The interaction between “Bcl-XL” and “Bad” proteins was measured, using a mutant protein as a negative control. FLIM images were converted into binding curves and relative binding association constants were estimated. The efficacy of two small molecule Bcl-XL inhibitors were tested using our system. Two confocal FLIM channels can be acquired using our system in less than 1.5 seconds. Four field of views were required to construct binding curves. Thus, a sample can be measured in less than 6 seconds in our system. In theory a 384-well plate can be measured in less than 40 minutes using our multiplexed confocal approach and a SPAD array.

**Chapter 6** provides a summary of the major milestones achieved in this work. Current limitations of the current system are also discussed. This chapter also discusses the next steps required to make this prototype ready to perform a full 384-well plate screen. Additional imaging modalities that can be realized with our system are also presented including multipoint FCS and hyperspectral FLIM imaging.

#### **1. 4 Contributions**

The thesis is presented as three journal articles Chapters 3 to 5. I wrote the original drafts of each of the articles. Revisions were made based on feedback from listed authors.

The original prototype was designed by Dr. Qiyin Fang, Dr. Richard Berman and Dr. David Andrews. It was implemented by Dr. Anthony Tsikouras at McMaster University.

The window scanners were designed and implemented by Dr. Anthony Tsikouras. Live cell samples (seeding, transfection and treatment) for Papers I-III (and Appendix A & B) were prepared by Elizabeth J. Osterlund from Dr. David W. Andrews lab.

#### **Paper I**

The streak camera has unparalleled time resolution. Here we developed a time delay scheme in a multiplexed synchroscan streak camera, to minimize the crosstalk between input channels. We also create a novel method to correct for temporal nonlinearity. Combining our alternating fiber design and temporal corrections; enhances the streak as a multiplexed detector. We demonstrate, our multibeam generation method can be used to test and improve multiplexed detectors.

For this project, Dr. Anthony Tsikouras designed the 2D-1D fiber array with an alternating 12.5 ns delay to match the synchroscan scheme. The system was built by Dr. Tsikouras and me at Sunnybrook Research Institute, Dr. Andrews lab.

I prepared and image the Fluorescein, Coumarin-6 and quenched fluorescein solutions. Dr. Tsikouras imaged the convallaria and I reconstructed the lifetime image.

The original analysis code was built as a prototype in MatLab. I re-wrote it in C++. I have included the maximum likelihood library for lifetime estimation. The original barrel distortion code was written by Dr. Tsikouras in Matlab. I improved the algorithm and implemented it in C++.

I performed the experiments for Fluorescein and Coumarin-6 at different operation mode. The cross-talk analysis was also completed by me. The virtual grid search used to measure the temporal profile was co-developed with Dr. Tsikouras. I performed the experiments using quenched Fluorescein sample. I also scanned and reconstructed the FLIM images for the live cell experiments

### **Paper II**

In this article, we present a new multiplexing approach that rivals the spinning disk confocal. With higher sensitivity and exposure time, we believe this work is of interest to researchers looking to implement advanced imaging techniques.

Our third prototype (32x32 multiplexed system) was built by Dr. Anthony Tsikouras, at McMaster University. I made several alignment iterations with the help of another student, Morgan Richards (Master's student). The C++ software script was written by Dr. Anthony Tsikouras and Morgan Richards. Galvanometer (galvo) scanners software was for written by Bo Xiong (PhD student) then improved by Dr. Tsikouras. Convallaria scans were acquired by Dr. Tsikouras. I performed the live cell imaging, as well as laser power versus photobleaching experiments.

### **Paper III**

In this work, we provide a template for the next generation of confocal FLIM microscopes. Our designed system can collect binding information from a single sample within seconds. This bridges the gap between confocal FLIM imaging platforms and drug screening experiments.

I performed several the time-gate optimization experiments. Both contiguous and overlapped gate modes were tested. I imaged the *Convallaria* sample and reconstructed the lifetime maps. The performed and the imaging and the analysis for the FRET control samples.

I imaged the BMK cells expressing Bcl-XL and Bad. Reconstructed the lifetime scans. I have built the algorithm to reconstruct binding curves from FLIM images and extract binding dissociation constants.

## References

1. Ran, X., & Gestwicki, J. E. (2018). Inhibitors of protein–protein interactions (PPIs): an analysis of scaffold choices and buried surface area. *Current opinion in chemical biology*, 44, 75-86.
2. Nero, T. L., Morton, C. J., Holien, J. K., Wielens, J., & Parker, M. W. (2014). Oncogenic protein interfaces: small molecules, big challenges. *Nature Reviews Cancer*, 14(4), 248-262.
3. Li, Q., Quan, L., Lyu, J., He, Z., Wang, X., Meng, J., ... & Li, H. (2016). Discovery of peptide inhibitors targeting human programmed death 1 (PD-1) receptor. *Oncotarget*, 7(40), 64967.
4. Dawidowski, M., Emmanouilidis, L., Kalel, V. C., Tripsianes, K., Schorpp, K., Hadian, K., ... & Rodriguez, A. (2017). Inhibitors of PEX14 disrupt protein import into glycosomes and kill Trypanosoma parasites. *Science*, 355(6332), 1416-1420.
5. Hayes, M. P., Soto-Velasquez, M., Fowler, C. A., Watts, V. J., & Roman, D. L. (2017). Identification of FDA-Approved Small Molecules Capable of Disrupting the Calmodulin–Adenylyl Cyclase 8 Interaction through Direct Binding to Calmodulin. *ACS chemical neuroscience*, 9(2), 346-357.
6. T. Oltersdorf, S. W. Elmore, A. R. Shoemaker, R. C. Armstrong, D. J. Augeri, B. A. Belli, M. Bruncko, T. L. Deckwerth, J. Dinges, P. J. Hajduk, M. K. Joseph, S. Kitada, S. J. Korsmeyer, A. R. Kunzer, A. Letai, C. Li, M. J. Mitten, D. G. Nettesheim, S. C. Ng, P. M. Nimmer, J. M. O'Connor, A. Oleksijew, A. M. Petros, J. C. Reed, W. Shen, S. K. Tahir, C. B. Thompson, K. J. Tomaselli, B. Wang, M. D. Wendt, H. Zhang, S. W. Fesik, and S. H. Rosenberg, "An inhibitor of Bcl-2 family proteins induces regression of solid tumours," *Nature* (2005).
7. Oltersdorf, T., Elmore, S. W., Shoemaker, A. R., Armstrong, R. C., Augeri, D. J., Belli, B. A., ... & Joseph, M. K. (2005). An inhibitor of Bcl-2 family proteins induces regression of solid tumours. *Nature*, 435(7042), 677.
8. Cole, M. J., Siegel, J., Webb, S. E. D., Jones, R., Dowling, K., Dayel, M. J., ... & Neil, M. A. A. (2001). Time-domain whole-field fluorescence lifetime imaging with optical sectioning. *Journal of Microscopy*, 203(3), 246-257.
9. Agronskaia, A. V., Tertoolen, L., & Gerritsen, H. C. (2003). High frame rate fluorescence lifetime imaging. *Journal of Physics D: Applied Physics*, 36(14), 1655.
10. Hain, R., Kähler, C. J., & Tropea, C. (2007). Comparison of CCD, CMOS and intensified cameras. *Experiments in fluids*, 42(3), 403-411.

Commented [NH1]: References have been fixed

## Chapter 2. Background

### **Application of confocal fluorescence lifetime imaging microscopy in targeted molecule screening**

Many FDA approved drugs have an unknown mechanism at the molecular level [1]. Though these drugs can be highly effective, it is difficult to prevent side effects or make improvements to these compounds without knowing the target. Most diseases are complex: not caused by a single mutation, but rather many genetic variations can result in the same symptoms [2]. As a result of this and many other factors, two patients with the same respond completely differently to treatment due to disease heterogeneity [3]. Medicine is moving towards a more personalized approach, called precision medicine, where a doctor may use a patient's genetic disease profile to select a targeted therapy [4]. Drugs that target a known biological mechanism, called molecularly targeted therapies, will be useful in precision medicine.

Measuring binding of a compound to its target is necessary to demonstrate selectivity for molecularly targeted therapies. Knowing the exact drug target allows researchers to use intelligent design modify their hit compounds, improve binding affinity and reduce potential off target effects before proceeding to clinical trials. Most biological processes are steered by specific proteins interacting in a pathway within the cell. Proteins can interact with DNA, RNA, ions, lipids or other proteins. Any of these interactions may be feasible targets for small molecules to alter a disease state, but for the purposes of this work, we focus on protein-protein interactions (PPIs). Direct binding is commonly measured in a test tube, with the purified target. Researchers may also examine the efficacy of a compound to disrupt a desired protein-protein interaction. These experiments may give good evidence of direct binding for some soluble proteins, but poorly represent the physiological environment of the cell. Many proteins cannot be purified, making it more difficult to test drugs that target these proteins. Membrane proteins are well known to be difficult to purify and may fold/function differently in the absence of a membrane [5]. A solution to this is to use Fluorescence lifetime imaging microscopy (FLIM) to measure Forster resonance energy transfer (FRET) (described in Chapter 2.2) [6]. This technique allows scientists to measure full length PPIs inside a living cell.

However, drug discovery includes screening of thousands of small molecules for identification of 'hit' compounds. No microscope on the market can meet the need for accurate, high-throughput (1 second/sample), confocal, FLIM-FRET screening. TCSPC (described in section 2.4) is considered to be the most accurate method to measure fluorescence lifetime changes and determine binding in the cell. Data collection on traditional single point confocal FLIM instruments is very slow. A variety of engineering

designs have been proposed to address this challenge, including excitation multiplexing, detection multiplexing and the design of better detectors (described in section 2.6). We hypothesize that if FLIM-FRET microscopy can be made faster and more accessible, then the application of this technique will improve screening for compounds that selectively target PPIs in the cell.

Chapter, 2.1 describes the Bcl-2 family, a group of proteins containing many membrane-binding proteins. In order to measure Bcl-2 family binding interactions in a test tube most research to date has been done using truncated proteins (cutting off membrane binding region) and peptides (purified ligand binding domain only). The Andrews lab and others have shown that studying truncated Bcl-2 family proteins neglects the role of membrane interactions and the membrane binding domain, two factors that can contribute to resistance to drugs that target the Bcl-2 family (described later). To study these proteins and the drugs that target them specifically, David Andrews and Qiyin Fang labs have made a collaborative effort to advance FLIM-FRET microscopy.

## 2.1 Bcl-2 family proteins and their role in regulating cell death

Over 50 billion cells die and are replaced in the adult human body daily [7]. To ensure tissues do not shrink or grow, cell death and cell creation must be balanced. This balance is responsive, for example, increased cell death due to some environmental factor or injury will be combatted by increased proliferation in that tissue and vice versa. In the long term, tipping this balance results in serious health problems. For example, increased cell death has been associated with development of neurodegenerative diseases [8] and decreased cell death with tumorigenesis.

There are many ways a cell can die. For example, in the case of a physical injury cells die by *necrosis*. In this process cells swell, burst open and intracellular debris is released leading to an inflammatory response. Inflammation can damage neighboring cells, adding to the injury. On the other hand, cells that are intrinsically damaged, too old, or not needed, die by a programmed form of death, called *apoptosis*. Cells undergoing apoptosis can be identified by signature features: loss of mitochondrial potential (ability of mitochondria to produce energy), cell shrinkage as the cytoskeleton collapses, nuclear shrinkage/fragmentation, and loss of plasma membrane polarity [9]. The cell's plasma membrane blebs and the membrane-encased fragments of the dead cell components are called apoptotic bodies. The apoptotic bodies release "eat me" signals that signal macrophage cells to ingest them and recycle their contents. This tidy mechanism of packaging and clearing the debris of a dead cell happens rapidly and does not trigger inflammation [10,11]. Apoptosis is critical to maintaining tissue homeostasis, mentioned earlier. There are two forms of apoptosis: extrinsic apoptosis (triggered from outside the cell, by activating cell surface death receptors) and intrinsic apoptosis (triggered by damage inside the cell and controlled at mitochondria). Most chemotherapies kill cells by activating intrinsic apoptosis [12,13].

During my PhD, we used FLIM-FRET to study interactions of proteins in the Bcl-2 family, within the intrinsic cell death pathway. The Bcl-2 family proteins control a key step in intrinsic cell death, mitochondrial outer membrane permeabilization (MOMP). MOMP marks the ‘point of no return’ for the cell, since it leads to an irreversible release of proteins (SMAC and cytochrome C) from the intermembrane space. Release of these factors leads to activation of caspases, enzymes that “chew” up important proteins in the cell, ultimately resulting in the morphological changes mentioned earlier as the cell undergoes apoptotic cell death.

Bcl-2 family of proteins can be classified based on their structure. Bcl-2 proteins share homologous domains known as the Bcl-2 homology (BH) domains (Figure 1). Some Bcl-2 family proteins have up to four BH domains (multi-domain proteins), while others may have only one (BH3 only proteins). It is important to understand that multi-domain proteins can form a ‘pocket’ into which the BH3 domain of other Bcl-2 family proteins can bind. It is also important to note that many of the Bcl-2 family proteins have a membrane binding domain (MBD), and binding to the membrane can impact the proteins structure and function [14].

Bcl-2 family of proteins can also be classified by their function (Figure 1). Some Bcl-2 family proteins promote cell death (pro-apoptotic), while others promote cell survival (anti-apoptotic). Pro-apoptotic multi-domain *pore former* proteins, Bax and Bak, form homo oligomer pores on the mitochondrial outer membrane (MOM), leading to MOMP. Bax and Bak normally exist in an inactive state in the cell. When the cell becomes stressed, *BH3-only activator* proteins are activated and they bind to and directly activate the pore formers. *Anti-apoptotic* proteins are multi-domain proteins that bind to activated pore formers and BH3 activator proteins, thereby inhibiting pore formation and MOMP. Finally, *BH3-only sensitizer* proteins bind and inhibit anti-apoptotic proteins but cannot directly activate pore formers. The fine-tuned balance of the pro-apoptotic and anti-apoptotic signals in the cell determines if MOMP occurs. Furthermore, this balance is influenced not only by relative concentration of the Bcl-2 proteins but also by binding affinities, protein stability, localization in the cell, membrane binding and post translational modifications [15].

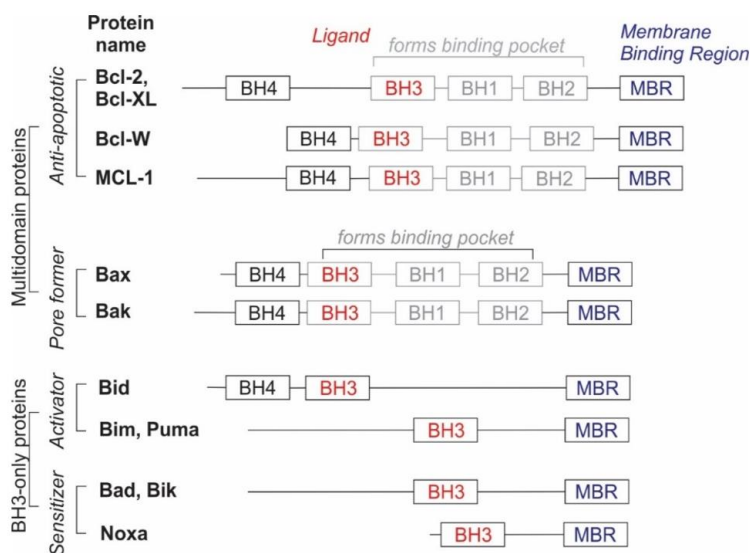


**Figure 2.1.** Diagram of Bcl-2 family homology domains. Proteins (named in bold) are represented by a line, where boxes along the line show Bcl2 homology (BH) domains 1-4 and the Membrane Binding Region (MBR). To the left of this figure, the structural classification (multi-domain or BH3 only) as well as functional classification (italics) is indicated. This figure was modified from [14].

Cancer cells can evade death by increasing the expression levels of anti-apoptotic proteins [15]. Thus, designing small molecules that inhibit anti-apoptotic Bcl-2 family proteins may promote cancer cell death. This is the same mechanism that BH3-only sensitizer proteins work and these inhibitors compete for binding to the same pocket as the BH3 domain. Therefore, these anti-apoptotic inhibitors are known as “BH3 mimetics”. Abbot Laboratories (currently named Abbvie) has developed BH3 mimetics targeting Bcl-2, Bcl-XL and more recently, Mcl-1. Their compound ‘ABT-199’ (Venetoclax) is a specific Bcl-2 inhibitor that was FDA approved in April 2016 for treatment of Chronic lymphocytic leukemia, making it the first BH3 mimetic cancer therapeutic. ABT-199 is showing promising results for treatment of some cancers as a single agent and others in combination with chemotherapeutics [16].

The success of ABT-199, has led to tremendous interest, by several pharmaceutical companies, to develop BH3 mimetics that target other Bcl-2 proteins. There is evidence that cancers may develop resistance to ABT-199 by switching their reliance to expression of another anti-apoptotic protein to evade death. Several clinical trials are now in progress

evaluating different Bcl-2 protein inhibitors [17]. In theory, combination of BH3 mimetics could be used to eliminate resistance.

Bcl-2 family of proteins include over 20 members. Each is regulated differently and have differences in affinity for binding one another. A review by Kale et al. (2018) highlighted that the majority of Bcl-2 family PPIs have only been measured for small BH3 peptides binding to truncated anti-apoptotic proteins in the absence of a membrane. Further, most BH3 mimetics have only been demonstrated to bind truncated anti-apoptotic proteins. Thus, there is need to measure full-length Bcl-2 family PPIs and BH3 mimetic efficacy using alternative methods such as FLIM-FRET. Fluorescence lifetime imaging allows us to investigate full length protein in their native cellular environment. This is achieved by looking at changes in fluorescence lifetime as energy transfer takes place between two fluorescently labelled proteins. The change in energy transfer is highly altered when even the slightest changes in the distance between the two proteins takes place. Which provides a way to probe weak protein-protein interactions with high accuracy. More details on this will follow in the coming sections. This work was started in the Andrews lab by Dr. Qian Liu [18,19]. In her work, Qian was limited to only measure less than 20 samples maximum in a single experiment. Here our aim was to achieve faster imaging to collect a full 384 well plate screen in less than an hour.

## **2.2 FRET for measuring protein-protein interactions**

A fluorophore is protein that can absorb and emit energy in the form of light. A fluorophore can be added to the N- or C-terminus of a protein of interest by cloning the fluorophore DNA up or downstream of the gene of interest, respectively. Tagging with a fluorophore allows visualization of the protein of interest in the cell by fluorescence microscopy [20]. Different fluorophores absorb and emit light energy at specific wavelengths. Selecting fluorophores that have different absorption/emission spectra allows simultaneous visualization of multiple tagged proteins in the cell. Binding between these two proteins can be measured by selecting a pair of fluorescent proteins that can undergo a dipole-dipole energy exchange process known Förster resonance energy transfer (FRET). In the next few sections we will examine how FRET serves a molecular level ruler to measure PPIs in live cells.

### **2.2.1 Förster resonance energy transfer.**

When a fluorescent molecule absorbs a photon, it remains in the excited state until it navigates means of giving off the energy and returning to the ground state (Figure 2). FRET takes place when a nearby fluorescent molecule can accept that energy via a non-radiative dipole-dipole interaction. The fluorescent molecule giving and receiving energy are referred to as the donor and acceptor respectively [6].

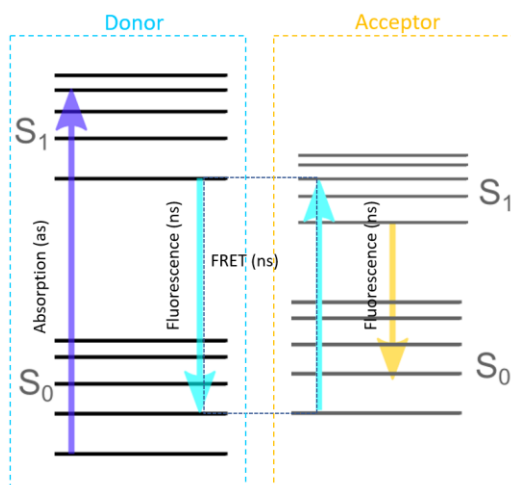


**Figure 2.2.** Schematic depiction of electron vibrational energy states that can occur during FRET. A donor molecule gets excited to the higher electronic energy state through photon absorption (purple arrow). The molecule can relax to the excited state by emitting a photon. In the presence of a nearby molecule a non-radiative energy transfer can take place between the ‘donor’ and the ‘acceptor’. The excitation energy of the acceptor must be equal to the energy difference between the excited state and the ground state for the donor.

Several parameters affect the efficiency of energy transfer: spectral overlap, the orientation of the dipoles, the quantum efficiency of the donor and the acceptor, and the distance between donor and acceptor.

Spectral overlap is the first property to consider when selecting a donor and acceptor pair. The emission spectra of the donor fluorescent molecule must sufficiently overlap with the excitation spectra of the acceptor. This rather an intuitive requirement since the energy of the emitted photon must equal the energy needed to excite the acceptor. In many of our experiments we use the donor, mCerulean3, and acceptor, Venus (Figure 3). The mCerulean3 emission overlaps with the Venus excitation.

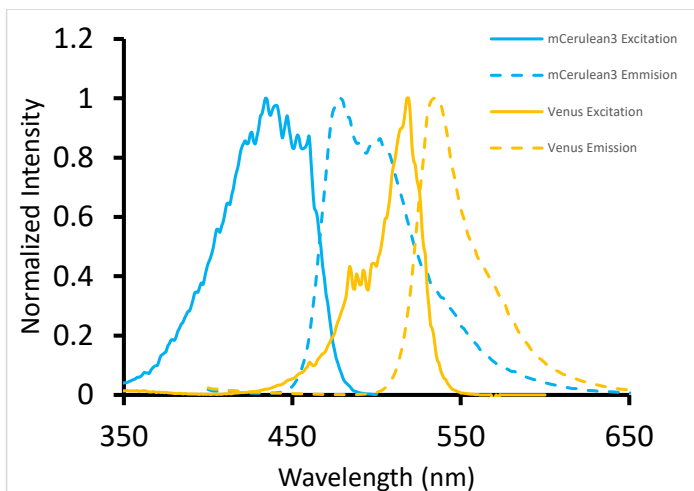


**Figure 2.3.** Spectral emission and excitation profiles for *mCerulean3* and *Venus*. Purified *mCerulean3* and *Venus* proteins (1  $\mu\text{M}$ ) used to measure spectra on a Tecan microplate reader in a 96 well quartz plate. *mCerulean3* excitation was measured with emission at 515 nm, and *mCerulean3* emission was measured with a fixed excitation at 440 nm. *Venus* excitation was measured with emission at 550 nm and *Venus* emission was measured with a fixed excitation wavelength of 520 nm. Background from buffer alone was subtracted, and raw data was normalized to the maximum for each spectral.

Tremendous work has been put into designing brighter fluorescent proteins that exhibit monoexponentially decaying fluorescence profiles [21]. In most biological environments, the dipole orientation of two fluorophores can be thought of as fixed on average. Rotational diffusion of fluorescent proteins allows sampling of many orientation states during image acquisition. To give rotation freedom, we include a short flexible linker region between the fluorophore and the fused protein of interest. It is worth noting that this assumption is not always valid, and some protein-protein pairs require linker optimization to provide a different orientation and/or closer proximity to the acceptor [22].

Most importantly, the efficiency of non-radiative energy transfer between an acceptor and donor is proportional to the inverse sixth power of the distance separating them as shown in:

$$E_{FRET} = \frac{1}{1 + \left(\frac{r}{R_0}\right)^6} \quad (1)$$

Where  $E_{FRET}$  is the energy transfer due to FRET,  $r$  is the distance between the donor and acceptor fluorophore,  $R_0$  is the distance at which the energy transfer is 50%. From

Equation 1, we can conclude that small changes in the distance  $r$ , results in large changes in the observed energy transfer. For this reason, FRET is thought of as a “molecular ruler” and is a measure of direct binding because FRET only occurs when the two proteins are within 10nm.

### 2.2.2 Methods of measuring FRET

#### Intensity-based methods

When FRET occurs, the fluorescence of the donor decreases while the acceptor fluorescence increases. Thus, change in acceptor or donor fluorescence intensity can be used to directly measure the rate of energy transfer. This is quite straight forward to do in a test tube because we can prepare 3 conditions, using exact concentrations of donor and acceptor:

1. Donor-labelled protein
2. Donor-labelled protein + unlabeled acceptor protein
3. Donor-labelled protein + acceptor-labelled protein

We add the donor to all wells, measure the donor alone, then add the unlabeled or labelled acceptor (2 and 3) and measure the change in donor fluorescence over time. If there is a larger decrease in fluorescence in 3 compared to 2 and 1, then FRET has occurred. A similar experiment can be done with labelled donor compared to unlabeled donor protein to quantify FRET by measuring the increase in acceptor emission. Using intensity changes to measure FRET is only accurate when all components in the system are known and controlled for.

Consider Figure 3 and note the emission profile of mCerulean3 (donor) trails into the emission spectrum of the Venus emission (acceptor). Further, the excitation source used to excite mCerulean3 (430-470 nm) can also excite the Venus. The overlap of the donor and acceptor excitation spectra is called acceptor crosstalk, and the overlap of the donor and acceptor emission spectra is called donor bleed-through. Both factors can be corrected for when the concentrations are known. However, slight changes in concentration will affect the measurement of FRET, making intensity-based methods error prone.

If we do not know the concentration of the donor and/or acceptor, then we cannot say whether fluorescence intensity detected is from the donor, acceptor or FRET. In a live cell system, we express proteins transiently do not know the concentrations. Therefore intensity-based FRET measurements are performed differently than in a test tube.

To measure FRET in cells some groups use the Acceptor Photobleaching method [23]. The donor and acceptor-labelled proteins are expressed in a cell, then the intensity of the donor and acceptor are measured before and after photobleaching the acceptor. As the

acceptor is photobleached, the donor emission increases and this is used to detect FRET in cells. Due to the requirement of imaging twice, this method is slow and not suitable for screening purposes. Photobleaching the acceptor exposes the sample to damaging levels of light energy. This method is also only a “single shot” view of FRET, as photobleaching is an irreversible process.

An alternative method of measuring FRET in cells is the 3-cube FRET method, which is not photo-destructive [24]. The sample is imaged 3 times, changing the filter cube each time:

1. Donor excitation & donor emission
2. Donor excitation & acceptor emission
3. Acceptor excitation & acceptor emission.

This method requires switching between 3 different configurations for every image acquisition. Depending on the microscope used, this may be time consuming. Measurements of 3-cube FRET also requires accurate measurements of FRET standards, as well as many mathematical corrections for crosstalk and bleed-through. This method is prone to false positives when two proteins are located on the same membrane in a cell, so proper negative controls are required for an accurate determination of binding.

As reviewed recently, FLIM is the most accurate and reliable method for measuring FRET in live cells [25]. I will describe this next.

## 2.3 FLIM-FRET

### What is lifetime?

The average time spent by a fluorescent molecule in the excited state is referred as *fluorescence lifetime*. Fluorescence lifetime is an intrinsic property of a population of fluorescent molecules. Release of a photon is a stochastic event, therefore, some fluorophores release energy immediately and others hold onto that energy longer. Overall, the number of photons released overtime follows an exponential decay. The lifetime can be measured as average time that the population of fluorophores emit a photon, or the point at which decay is  $1/e$  of the initial intensity.

Lifetime depends on the local environment. Changes, in pH or collisional effects (crowding or increase in temperature) can lead to changes in the lifetime. These changes in local environment represent alternative paths for energy loss and for return of the fluorescent molecule to the ground state. For example, increase in local temperature, increases the molecular vibration and provides the excited molecule alternative means to dissipate its energy.

### **Measuring changes in fluorescence lifetime to detect FRET**

FRET provides the donor fluorophore with new non-radiative means of returning to the ground state. Thus, the fluorescence lifetime decreases as the rate of energy transfer increases.

Measuring changes in donor lifetime is considered the most accurate approach to measure FRET in live cells. There is no need to correct for spectral bleed-through or concentration changes because lifetime is not sensitive to changes in concentration [6]. Fluorescence lifetime instrumentation requires a detector with high temporal resolution to sample the fluorescence decay, which significantly adds to the cost of equipment. In Dr. Fang's lab myself and others have worked on designing faster and more affordable instruments.

#### ***2.3.1 Time domain and frequency domain methods for FLIM-FRET***

Fluorescence lifetime can be accurately measured using either frequency domain (FD), or time domain (TD) methods. FD methods utilize a sinusoidally-modulated light source to excite the sample. As would be expected, the emitted signal also forms a sinusoidal profile, but that emitted signal is delayed in time (phase shifted) and demodulated. The phase shift and/or demodulation can be used to estimate the fluorescence lifetime [27]. FD-FLIM can be used to detect a large range fluorescence lifetimes. This is achieved by changing the modulation frequency. FD-FLIM systems require acquisitions at multiple frequencies for multi-exponential lifetimes.

TD methods use a pulsed laser source to excite the sample and measure the arrival time of the generated photons using a detector with high temporal resolution. The histogram of photon arrival time is used to construct the exponential decay. The measured fluorescence decay is then modeled using an exponential function to estimate the average fluorescence lifetime. TD-FLIM allows the user to visualize the lifetime decay thus the resulting measurements are easier to interpret and model (with FD-FLIM, the decay is in the sinusoidal form) [28].

Both FD and TD systems provide can be used to measure binding (FRET) in live cells (Figure 4).

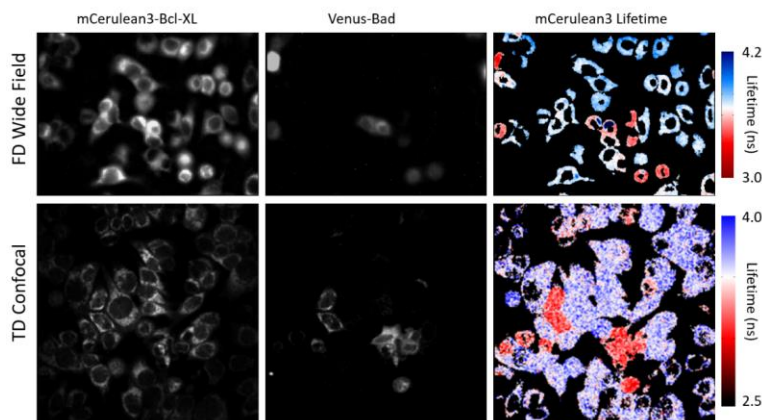


**Figure 2.4.** *Bcl-XL binding to Bad in live baby mouse kidney (BMK) cells.* (top) FD Wide field FLIM images acquired on a LIFA FLIM instrument. (bottom) TD confocal FLIM images acquired on our multiplexed confocal setup using time gated SPAD array (Chapter 4). Donor is mCerulean3 fused to Bcl-XL, and this protein is stably expressed in all BMK cells (left panel). Venus-Bad is transiently transfected into some cells (middle panel). Binding of Bcl-XL to Bad can be seen by change in lifetime (Right panel). Lifetime is represented on a pseudocolor scale.

FD-FLIM is typically more cost effective because modulated light sources and detectors don't require sub-nanosecond resolution. However, background and autofluorescence are more difficult to distinguish from the collected signal using a modulated light source. When multiple lifetimes are present (ie. FRET) a 'frequency sweep' is required (acquire at different modulation frequencies), making traditional FD-FLIM slower. Advanced frequency modulators, along with higher temporal resolution detectors, can be configured to avoid frequency sweeping. A modulated excitation profile can be created to be equivalent to the sum of harmonic frequencies (create a square modulated signal). Thus, multiple frequency sweeping can be avoided and faster imaging can be obtained [28].

From an engineering point of view, TD-FLIM data is much easier to bin and histogram photon arrivals, as well as model the decays. In most cases, the presence of multiple lifetimes can be easily evaluated using fitting and fit-free approaches [29]. With advancement in computational architectures like graphical processing units (GPUs), lifetime estimation can even be done on the detector itself prior to data storage [30,31].

The work in this thesis focuses on developing faster, confocal TD-FLIM imaging. We achieved this by combining confocal multiplexing approaches and new detector array technologies. In the next section we will examine how we process FLIM data to extract binding affinities.

## 2.4 Confocal FLIM imaging and protein-protein binding affinities

FLIM imaging can be implemented using both widefield and confocal techniques. Compared to widefield imaging, confocal scanning reduces the number of photons that can reach the detector. Decrease in photon counts leads to more time spent to acquire enough photons for lifetime determination. However, confocal FLIM offers several advantages for imaging biological samples, making it more suitable choice for screening applications. First, confocal imaging provides subcellular resolution information on the distribution of the fluorescently labelled proteins. This can be useful for a biologist to determine proper protein folding (no aggregation) and whether the protein goes to the expected location in the cell, which may be important for protein function. Second, confocal scanning rejects out of focus light, which results in higher contrast images (Figure 4, compare wide field and confocal scans). Better quality images provide more information for biologists to interpret. Third, confocal systems can be coupled to single photon counting detectors, for more quantitative imaging (more accurate detection of photon counts, which is proportional to the protein concentration). Lastly, by taking 2D confocal images in a z-stack we can reconstruct 3D images for optical sample sectioning. This has tremendous potential in screening applications, since there is a movement away from 2D to more physiologically relevant 3D cell culture models (organoids) [32]. For these reasons, the benefits to confocal FLIM outweigh the reduction in photon economy.

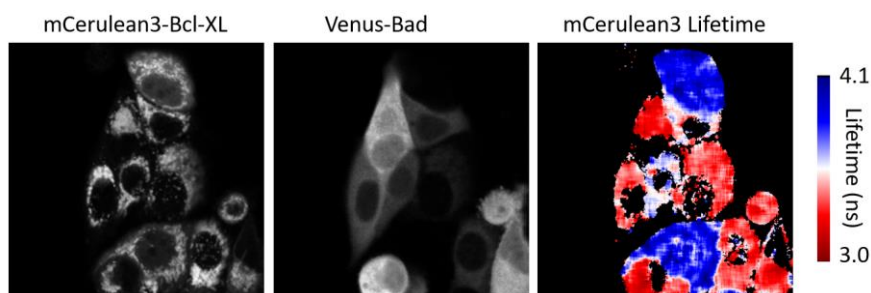


**Figure 2.5.** Example of fluorescence lifetime imaging used to measure binding between two Bcl-2 proteins. (left) Bcl-XL labelled using a cyan fluorescent protein (mCerulean3). (middle) Bad labelled with a yellow fluorescent protein variant (Venus). These images were acquired on the ISS-Alba single point confocal microscope. 100×100 field of view (256×256 pixels) acquired using 0.5 ms pixel dwell time. The total acquisition time was 32 s. The lifetime image was generated using a 7×7 nearest neighbour binning to reconstruct well sampled decays. Each decay was fit to a single exponential curve to estimate the lifetime.

Figure 5 shows an example of confocal FLIM image of a relatively small field of view compared to Figure 4. An image is reconstructed by scanning a laser beam across the sample in a raster motion. At each pixel, we measure the intensity of the donor (mCerulean3) and Acceptor (Venus) as well as the recorded arrival time for hundreds of

photons emitted from the donor. At each pixel several of the nearest neighboring pixels are binned, until we have enough counts to fit an exponential decay. Fluorescence lifetime is estimated at every pixel, providing a map of interactions across the entire image. Lifetime can only be estimated with sufficient photons, therefore in this confocal image there is no lifetime estimated for background or for some areas of the cell where there is very low donor concentration (the nuclear area= round circle inside cells). Nearest neighbor pixel binning is the most common way to analyze FLIM data, but effectively, this also reduces the resolution of the lifetime map (compare donor FLIM channel to donor intensity channel). In collaboration with Dr. David Andrews' lab, I have worked on improving lifetime image analysis by binning pixels within selected regions of interest prior to fitting (Appendix A). This work was not included in this thesis. However, a publication manuscript is in preparation to demonstrate the utility of the developed segmentation approach.

#### 2.4.1 Extracting binding curves from FLIM data

The confocal volume can be thought of as an observation volume. When scanned across the sample, we acquire independent measurements for binding between two fluorescently labelled proteins. As previously done by Liu et al., the donor labelled protein must be stably expressed in the cells and the acceptor labelled protein is transiently transfected. In Figure 5, see there is more variation in the acceptor (Venus-Bad) expression compared to the donor (mCerulean3-Bcl-XL) from cell to cell. This simulates performing a binding experiment in solution where one protein is fixed and the second is titrated in. Cells that have no acceptor (Venus-Bad) expression, have high fluorescence lifetime (no FRET). As the intensity of Venus-Bad increases, fluorescence lifetime decreases. Eventually, we reach a point where all the donor molecules in the confocal volume are undergoing FRET with an acceptor. Adding more acceptor will not further increase FRET efficiency.

The FRET efficiency can be determined by comparing the average donor lifetime in the presence and absence of donor:

$$E_{FRET} = 1 - \left( \frac{\tau_{DA}}{\tau_D} \right)$$

Where  $\tau_D$  is the fluorescence lifetime of the donor fluorophore alone, and  $\tau_{DA}$  is the fluorescence lifetime of the donor in the presence of the acceptor fluorophore.

Plotting the FRET efficiency as a function of the acceptor to donor intensity ratio can be used to construct binding curves (Figure 6 and Section 5.7.4). These binding curves can be only used to extract apparent dissociation constants ( $K_d$ )s (Section 5.7.5). In Appendix A, I will outline the work we have done to obtain more quantitative ( $K_d$ )s.

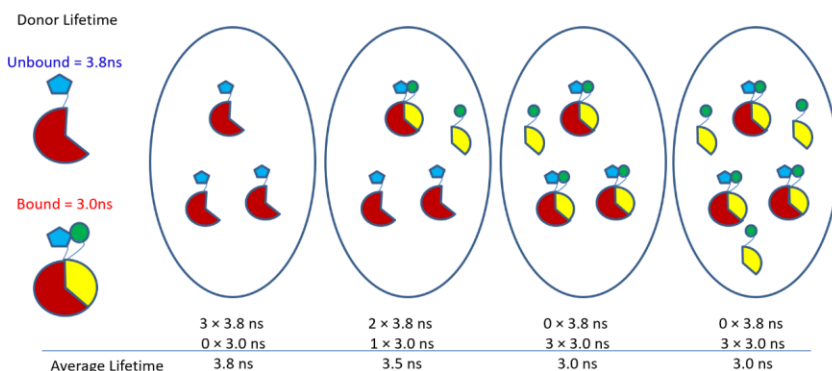


**Figure 2.6.** A schematic depicting how the average lifetime changes as a function of the acceptor to donor ratio. 2 proteins of interest are represented by the red and yellow shapes. Donor (blue pentagon) is fused to one protein of interest, and acceptor (green circle) is fused to another. Each large oval represents a confocal volume containing a number of donor- and acceptor-fusion proteins, and below each is the corresponding calculation of average lifetime. Unbound lifetime in this theoretical model is 3.8ns whereas bound lifetime (FRET) is 3.0ns.

### 2.3.2 Time correlation single photon counting

Time correlated single photon counting (TCSPC) is considered to be the gold standard method for measuring fluorescence lifetime [33]. Each time a single photon reaches the detector it is counted and the arrival time recorded. The arrival times of collected photons are stored using time bins as small as 50ps. To determine the lifetime, a histogram of all photon arrivals is reconstructed and fit to an exponential model. Traditional TCSPC detectors are composed of a single photon detector and a specialized computer card to perform the counting. The single photon avalanche photodiode (SPAD) is one of the most commonly used detectors.

In a SPAD detector, the energy from an incoming photon is converted to an electric current by cascading amplification of the signal across an electric field [34]. In detail, a SPAD consists of a reverse biased p-n junction that forms a depletion layer where charge is not allowed to pass through. Upon the absorption of a photon in the depletion layer, a free electron is generated. It gains kinetic energy in the applied electric field and knocks out other electrons creating new electron-hole pairs, which is repeated in a cascade of new electrons knocked out. The rapidly generated electron-hole pairs act as charge carriers across the depletion layer. The generated current can reach milliamperes which is large enough to detect. The voltage needs to be brought back to the original state to resume the detection process. An active circuit quencher resets the avalanche diode by quenching the applied voltage across the diode. The time required to do this is termed 'dead-time' since no photon can be detected. In a classical SPAD detector time stamping

is performed using a capacitor-based time-to-amplitude converter (TAC). As the ‘start signal’ is received the capacitor begins to charge linearly until the ‘stop signal’ (photon detected) is received. Cleverly, most TCSPC measurements are now done in “reverse mode”. In reverse mode the “start” signal is initiated only when a photon is detected, and the stop signal is connected to the reference excitation pulse. Since photon arrival is a stochastic event, reverse mode requires significantly less circuit resets [35].

For TCSPC only a single photon can be measured at one time, meaning sample photon generation must be limited to reduce the chance of two photons arriving simultaneously (photon pileup). Further, there must be enough time between photons to reset the detector (dead-time). The combination of these two limitations determines the “TCSPC limit” and limits the speed of acquisition in FLIM imaging. Excitation pulses used for majority of FLIM experiments are within 10-80 MHz (12.5-100 nanoseconds period). However, dead-times for current TCSPC SPAD detectors can range from 80 nanoseconds to 250 nanoseconds [24]. The relationship between the dead-time and pulse rate can be used to determine the experimental limit of TCSPC acquisition.

As a rule of thumb, the acquisition should be set such that one photon is registered every 20 pulses (5% TCSPC limit) [36]. Due to this limitation and the requirement for enough photons to determine lifetime, single confocal TCSPC instruments are slow. For instance, biological imaging is usually done using pixel dwell times in the range of 100 microseconds to 0.5 milliseconds. For a 256×256 pixel scan this results in acquisition times in the range of 6.5 seconds to 35 seconds. These acquisition times are not suitable for real-time imaging and screening applications. At maximum speed it would take days to acquire data for a 384-well plate. The work presented in this thesis focuses on bringing this time down to less than an hour. In the next section I will discuss engineering solutions presented by other groups, manufacturers and our lab to increase speed of TD-FLIM.

## **2.5 Engineering solutions for faster confocal TD-FLIM**

### ***2.5.1 Single point confocal TD-FLIM***

As mentioned earlier, the ‘dead-time’ is time when a photon cannot be detected due to detector circuit reset. Therefore, advances in circuit manufacturing results in faster imaging. In 2016 PicoQuant introduced the TimeHarp260 TCSPC card uses a phase-locked loop (PLL) to time the photon arrivals [37]. The design of the PLLs uses different phases to separate signals. The ‘start’ and ‘stop’ signals generate two waveforms (usually a square signal) which have different phases. The phase difference is then used to measure the difference between the two triggers. The design of the TimeHarp260 reduces the dead time to less than 2 ns, enabling higher rates of photon detection. In fact, the 1-2 nanosecond dead time associated with these cards are the result of the time needed to move the data to memory. This HydraHarp260 card can accurately detect 6 photons in every 20 laser pulses (operating at 30% TCSPC limit). PicoQuant demonstrated that live cell imaging can be performed on a single point confocal microscope using a 30  $\mu$ s pixel dwell time (1 frame per second using, 256×256 pixels, and 16  $\mu$ W power measured at the objective) [38,39].

Another approach to overcome the TCSPC limit, was implemented by The National Optics Institute's (INO) in their INO-FLIM hyperspectral (FHS) microscope. This system uses a single TCSPC card (HydraHarp400, <80 ns dead-time) however it splits the signal across 8 SPADs [40] (Figure 7). The signal collected from all the SPADs are synchronized to ensure that they are acting as a single detector. INO's design reduces the limitation imposed by the stochastic nature of photon arrival. We have used the INO-FHS microscope to image live MCF-7 cells stably expressing mCerulean3-Bcl-XL (Bcl-2 family member). We were able to scan the sample using a 50  $\mu$ s pixel dwell time, resulting in a ~4 s scan (256 $\times$ 256 pixels using <5  $\mu$ W power, measured at the objective). We measured an 8-fold increase in acquisition speed on the INO-FHS compared to a single point confocal microscope with a single SPAD (ISS-Alba, Table 1) [41]. In Chapter 3 we discuss the importance of keeping limiting the laser power to avoid sample photobleaching. The data for the photobleaching experiments are shown in Appendix B

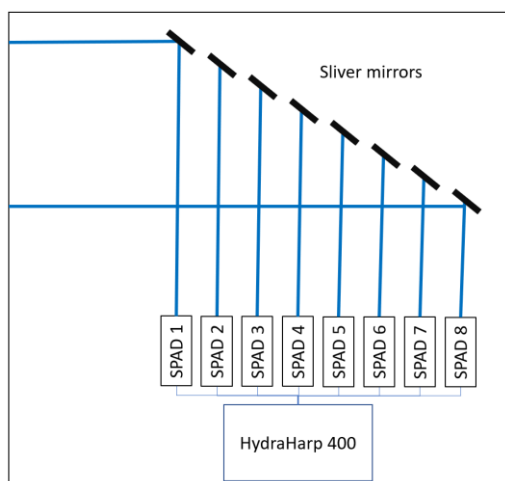


**Figure 7.** Schematic representation of the parallelized TCSPC detector in the INO-FHS microscope. A set of 8 silver mirrors (black rectangles) are used to divide the collected fluorescence signal across 8 SPADs, controlled by a single TCSPC card.

Different instruments have different designs and components, making it difficult to quantitatively compare their performance, even with the same sample imaged. However, we believe that the performance of FLIM microscopes should be benchmarked using biological samples as well as standard fluorescent dyes. Fluorescent dyes tell us how accurate the system is to measure a well-established standard. However, imaging biological samples is a more realistic test of the system's speed. Compared to standard fluorescent dyes, fluorescent proteins expressed in cells emit low photon counts. We report the speed

used to image biological samples on each system presented in this thesis. Table 1 provides a comparison for the three single point confocal systems, which will be useful for comparing to multiplexed confocal FLIM solutions in later sections.

	<b>ISS Alba (V5)</b>	<b>Zeiss LSM 780</b>	<b>INO FLIM HS</b>
<b>Detector</b>	SPAD	SPAD	8x Silicon SPADs
<b>TCSPC Card</b>	SPC-830 (Becker and Hickl)	TimeHarp 260 (PicoQuant)	HydraHarp 400 (PicoQuant)
<b>Detector dead time</b>	125 ns	<2 ns	<80 ns
<b>Time bin resolution</b>	195 ps	250 ps	64 ps
<b>Excitation pulse rate</b>	20 MHz	32 MHz	40 MHz
<b>TCSPC limit</b>	5%	30%	8x 5%
<b>Pixel dwell time</b>	0.4 ms	30 $\mu$ s	50 $\mu$ s
<b>Acquisition speed</b>	~30 s	1 s	<4 s
<b>Laser power at the objective</b>	<5 $\mu$ W	16 $\mu$ W	<5 $\mu$ W
<b>Acquisition by author</b>	Yes	No	Yes

**Table 2.1.** A comparison among three different commercial systems that use a single point confocal FLIM to image biological samples. The shown parameters are for images composed of 256 $\times$ 256 pixels.

Single point confocal microscopes remain the most widely used systems due to their versatility. These systems can be used for multiple applications such as FLIM, Fluorescence correlation spectroscopy (FCS), Fluorescence recovery after photobleaching (FRAP)[42,43]. As mentioned earlier, the goal of this thesis was to bring the screen time for a 384 well plate down to less than an hour and single point confocal systems cannot reach this goal (Table 1). In the next section, we will introduce confocal multiplexing as the solution to reach these speeds.

## 2.6 Multiplexed Confocal FLIM Systems for Screening Applications

Confocal multiplexing refers to increasing the number of excitation points used to scan the sample in a confocal microscope. Although many multiplexing designs have been proposed and implemented over the past few decades [ 44-46], only a handful are capable of confocal FLIM acquisition. A detailed comparison of several multiplexed FLIM systems have been presented by a previous PhD student in Dr. Fang's lab, Dr. Anthony Tsikouars, in his dissertation thesis [47]. Such a comparison will not be recreated here to avoid redundancy. Here I will compare the two current designs with the largest degree of confocal multiplexing: system built by Dr. Paul MW French's group and a system we built. Both systems deploy microlens arrays (MLAs) to achieve beam multiplexing and both are designed to be used as attachments to existing commercial microscopes. In the next section

we will present how FLIM imaging is achieved in these systems and later (Chapter 5) we will highlight the benefits to our design.

### ***2.6.1 Spinning disk multiplexed confocal FLIM***

Dr. Paul M. W. French's lab at Imperial College London University achieves high multiplexing by using a modern design of confocal spinning unit (CSU). The original design of a spinning disk (also known as a Nipkow disk), did not include MLAs [48]. Modern CSUs have added MLAs in a secondary disk to increase the light throughput. The first disk contains nested spirals of MLAs that create the foci array. The second disk contains matching spirals of pinholes to reject out of focus light. In our publication (Chapter 4) this is shown in Figure 1. Sample scanning using a CSU is achieved by the spinning disks. Even with one twelfth of a revolution, excitation foci cover the entire field of view. Modern CSUs, such as the CSU-X1 from Yokogawa) can have up to 20,000 pinholes and be spun at 10,000 rpm.

Since the spinning disk is always in motion, the emitted signal must be painted across a dense pixel array imager. This limits how time-resolved imaging is achieved with spinning disk systems. Time gated CCDs are currently the only detectors that can be coupled to CSUs for FLIM. Unlike TCSPC, the time gating approach collects photons within a set time window. Sampling the decay requires multiple acquisitions (minimum two) to estimate the fluorescence lifetime. A gated optical intensifier is composed of a multichannel plate (MCP) used to amplify the signal (intensity-based measurement). Grant et al., presented a fast spinning disk confocal system built for FLIM-FRET screening applications (Figure 8) [49,50]. Such systems are limited by the frame rate of the CCD (in this case 30 fps). Grant et al., imaged live cells expressing enhanced GFP protein and required integration times between 1-4 seconds for accurate determination of fluorescence lifetime.

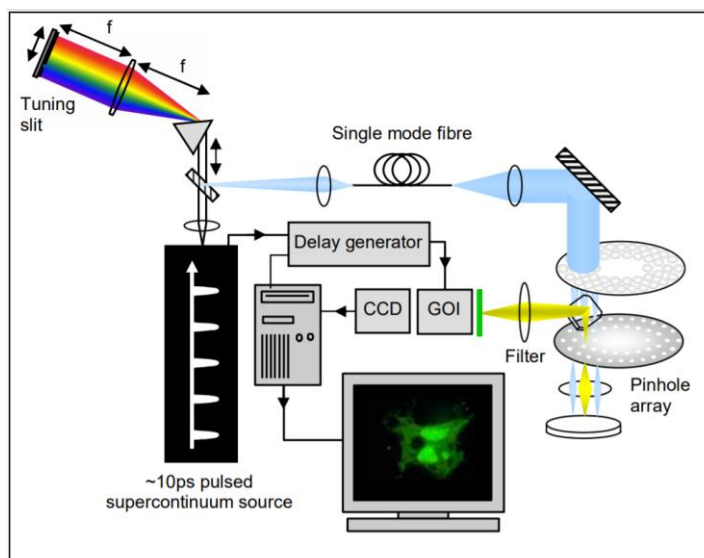


**Figure 2.8.** Schematic for the spinning disk confocal FLIM system. This diagram was copied from Grant et al., [ref]. This system included a pulsed white laser source, with a diffraction gradient to select the excitation wavelength. The excitation multiplexing was achieved using the CSU-19 Nipkow disk scan(right), which was coupled to the Olympus 1X81 microscope (not shown). FLIM imaging was performed using a photocathode gated optical image intensifier (GOI) coupled to a scientific grade CCD camera. Rapid FLIM imaging can be achieved with this system using only two time-gates (1 nanosecond gate width, not shown).

Thus far, Perkin Elmer was the only commercial company to offer a highly multiplexed spinning disk confocal FLIM instrument. The commercial Opera High Content Screening (HSC) platform included the option of adding a gated CCD for FLIM. Perkin Elmer discontinued this feature in their latest system, the Opera Phenix [51].

### 2.6.2 Microlens array and refractive window scanners for rapid FLIM imaging

Our solution uses MLAs and refractive window scanners to achieve the same level of confocal multiplexing as a spinning disk system (Chapter 4). The advantage of our design is that the collected fluorescence signal is de-scanned into fixed points that can be collected by a dense or a sparse pixel array detector. This means our attached can be coupled to a wider range of detectors for time-resolved applications. Figure 9 shows the schematic diagram of our multiplexed setup. Chapters 3-5 contain detailed descriptions of the optical setup.

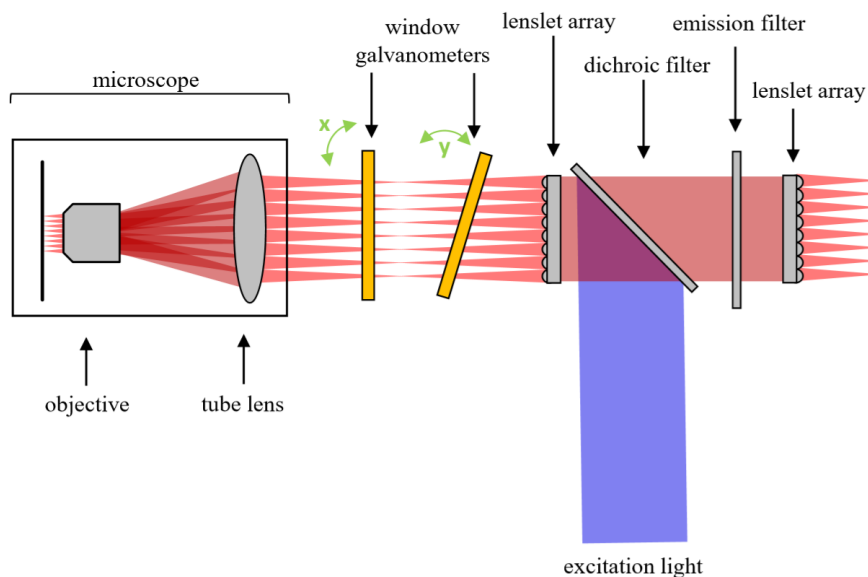


**Figure 2.9.** Schematic of our multiplexed approach using microlens arrays and refractive window scanners. MLAs are used to create a foci array, focused at the conjugate plane of the side port of an inverted fluorescence microscope. The foci array can be shifted along the x and y axes using a pair of refractive window scanners [52]. The collected fluorescence signal is de-scanned and relayed to a second MLA to recreate the fluorescence image collected from the sample.

Our design has evolved over the past 6 years, within three major iterations. The first prototype included a 2D-1D fibre array, with alternating fibre lengths, to interface to a streak camera. The characterization of the first prototype was presented in Dr. Anthony Tsikouras' thesis [47]. In summary, we were able to collect FLIM data for a standard *Convallaria* sample, however, the speed of the first prototype was limited by the linear sweep repetition rate of the streak camera (4 MHz). In the second iteration, we addressed this problem by switching from a linear to a sinusoidal sweeping unit (40 MHz). Since the fibre length difference must be half of the sweeping period, we also updated the 2D-1D array. Chapter 2 presents the full characterization of our second prototype. We were able to perform confocal FLIM imaging of fluorescent proteins expressed in live cells, however, the resulting speed did not meet our requirements for screening biological samples. Multiplexing was limited by the number of fibre inputs that could be coupled to the streak camera. For prototypes I and II we could achieve maximally  $10 \times 10$  multiplexing. The last iteration (prototype III), we increased the confocal multiplexing by 10-fold ( $32 \times 32$

excitation array). We coupled the multiplexed excitation scheme to a gated SPAD array to perform rapid FLIM imaging. Chapter 4 demonstrates the capacity of our third prototype to perform rapid FLIM imaging in live cells. With this setup, we were able to scan a large field of view ( $310 \times 310 \mu\text{m}$  using  $960 \times 960$  pixels, single channel) in less than a second. This speed meets our goal for theoretically scanning an entire 384 well plate in less than an hour. By adding a motorized stage and environmental controls in the future, this system would be suitable for biological screening applications. Table 3 summarizes our work and gives a comparison of our 3 prototypes to Paul French's spinning disk FLIM system.

	<b>Our Multiplexing System Prototype I</b>	<b>Our Multiplexing System Prototype II</b>	<b>Our Multiplexing System Prototype III</b>	<b>Spinning Disk FLIM</b>
<b>Number of focal points</b>	10×10	10×10	32×32	20,000
<b>Detector</b>	Streak Camera (Linear sweep)	Streak Camera (Sinusoidal sweep)	Time gated SPAD array	ICCD
<b>PDE (%)</b>	<5%	<5%	30%	35%
<b>Laser pulse rate</b>	4 MHz	40 MHz	40 MHz	50 MHz
<b>Time bin/gate size</b>	<50 ps	<50 ps	2 ns	1 ns
<b>Image size (pixels)</b>	400×400	300×300	960×960	256×236
<b>FOV limited by detector aperture</b>	No	No	No	Yes
<b>Acquisition time</b>	800 s	90 s	0.7 s	1-4 s
<b>Time Gated</b>	No	No	Yes	Yes
<b>Acquired by author</b>	No	Yes	Yes	No

**Table 2.2.** Comparison of highly multiplexed confocal FLIM setups.

### 2.7 Next generation detectors for multiplexed confocal FLIM

In section 2.3.2, we discussed how TCSPC measurements are typically conducted using a SPAD detector coupled to a specialized computer chip. These specialized cards perform the computations needed to 'time tag' the collected photons, data is stored on the chip, then transferred to the computer's memory.

TCSPC cards, have several advantages making them the most deployable solution in confocal FLIM microscopes. The performance of the TCSPC card is independent of

the specifications of the computer used for acquisition. Thus, detection performance is reproducible across any instrument using that card. These cards can be used to collect TCSPC information from multiple SPADs (Figure 7), which is ideal for multi-channel confocal acquisitions. Simultaneous excitation of two fluorophores can be achieved with excitation pulse interleaving. Lastly, the collection window of TCSPC cards can cover a wide temporal range (1-200 ns) [35] and the same instrument can be used to measure long or short lifetimes (Table 3).

<b>Class of fluorophores</b>	<b>Fluorescence lifetime range (ns)</b>
Endogenous fluorophores	0.1 – 7
Organic dyes	0.1 – 20
Fluorescent proteins	0.1 – 4
Quantum dots	10-30

**Table 2.3.** Example fluorescence lifetimes of different classes of fluorophores. Modified from [53]

These circuits are designed for high temporal resolution and versatility of use. However, the complicated circuits can only be coupled to a fixed number of input channels, which means they cannot be used for highly multiplexed FLIM.

### **2.7.1 Time-gated SPAD arrays for highly multiplexed FLIM**

In a traditional TCSPC acquisition, the SPAD is used to collect photons and the TCSPC card to determine arrival time. This separation between the detection and timing prevents classic SPADs to be created in array formats for multiplexed detection. Recent advances in Complementary Metal-Oxide Semiconductor (CMOS) technology overcomes this limitation by providing means to create complex circuitry within a small area. Each pixel contains a SPAD and circuitry needed to time the photon arrivals (SPAD array detector) [54]. These CMOS detectors are built in a variety of array formats, ideal for highly multiplexed FLIM imaging.

The 64×32 SPAD array detector (SPC3) we used in prototype 3 is commercially available from Micro Photon Devices and can measure time-gated FLIM. Two time gates can be collected simultaneously [55]. The SPC3 is easy to interface with a multi-beam array because its pixels have a large active area (30 μm diameter) and pitch (distance between two adjacent pixels). The pixels are sparsely arranged, which means this cannot be coupled to a spinning disk unit. We used a manual 3-axis stage to couple the SPC3 to our multibeam system. The acquisition frame rate for the entire sensor can reach 96,000 fps (50-150 nanosecond intraframe dead-time). The entire sensor is powered using a simple 5 V adaptor and is connected to the computer using a USB 3.0. The internal clock of the SPC3 is fixed to 50 MHz, which means that our total observation window is limited to 20 ns. This limits our system to accurately measure lifetimes above 5 ns, however, most fluorescent proteins have an average lifetimes less than 4 ns.

Time-gated SPAD arrays have many attractive features, including simple, rapid lifetime determination, elimination of background signal (autofluorescence) and reduction

of dark count rate (ignore counts outside the time gates). In chapter 4, we used a SPAD array detector to achieve rapid FLIM imaging in our third prototype. We used our system to measure lifetime in a biological sample in Chapter 4, Figure 4. To our knowledge, this is the first time a system with the same level of excitation multiplexing as a spinning disk can be coupled to an advanced sparse array detector. Table 3 highlights how our third prototype outperforms the spinning disk FLIM system in terms of speed.

### 2.7.2 TCSPC SPAD arrays for highly multiplexed FLIM

Engineers are continuously developing new improved SPAD arrays. SPAD pixels can be built with fully integrated time-to-amplitude converters (TACs) to perform TCSPC. This design fuses the collection and timing components of a TCSPC detector into a single pixel. We attempted to couple our third prototype to the Photon Force 32 (PF32), 32×32 SPAD array TCSPC detector. The camera is powered with a Field Programmable Gated Array (FPGA) to do on chip lifetime estimation using the center of mass method. Contrary to the SPC3 detector, the PF32 camera can run both as a master or a slave for TCSPC measurements [56,57].

In terms of practical implementation as a FLIM detector, we observed poor coupling efficiency out our multiplexed prototype 3. The PF32 has a small pitch size (50  $\mu\text{m}$ ) and active photon collection area (6  $\mu\text{m}$  diameter), making it extremely sensitive to detector movements. This due to the fact that complex pixel architectures require a larger number of transistors printed for each pixel, leaving less area for photon collection. Future improvements to our prototype should implement customized MLAs to improve the collection efficiency.

### References

1. Sun, J., Wei, Q., Zhou, Y., Wang, J., Liu, Q., & Xu, H. (2017). A systematic analysis of FDA-approved anticancer drugs. *BMC systems biology*, 11(5), 87.
2. Wheeler, H. E., Maitland, M. L., Dolan, M. E., Cox, N. J., & Ratain, M. J. (2013). Cancer pharmacogenomics: strategies and challenges. *Nature Reviews Genetics*, 14(1), 23.
3. Hanahan, D., & Weinberg, R. A. (2011). Hallmarks of cancer: the next generation. *cell*, 144(5), 646-674.
4. Collins, F. S., & Varmus, H. (2015). A new initiative on precision medicine. *New England journal of medicine*, 372(9), 793-795.
5. Lovell, J. F., Billen, L. P., Bindner, S., Shamas-Din, A., Fradin, C., Leber, B., & Andrews, D. W. (2008). Membrane binding by tBid initiates an ordered series of events culminating in membrane permeabilization by Bax. *Cell*, 135(6), 1074-1084.
6. Clegg, R. M. (2009). FRET and FLIM Techniques; ; Gadella, TWJ, Ed.
7. Kale, J., Osterlund, E. J., & Andrews, D. W. (2018). BCL-2 family proteins: changing partners in the dance towards death. *Cell death and differentiation*, 25(1), 65.

8. Singh, R., Letai, A., & Sarosiek, K. (2019). Regulation of apoptosis in health and disease: the balancing act of BCL-2 family proteins. *Nature Reviews Molecular Cell Biology*, 20(3), 175-193.
9. Chi, X., Pemberton, J., Nguyen, D., Osterlund, E. J., Liu, Q., Brahmabhatt, H., ... & Andrews, D. (2019). The carboxyl-terminal sequence of bim enables bax activation and killing of unprimed cells. *BioRxiv*, 554907.
10. Devitt, A., & Marshall, L. J. (2011). The innate immune system and the clearance of apoptotic cells. *Journal of leukocyte biology*, 90(3), 447-457.
11. Nagata, S. (2018). Apoptosis and clearance of apoptotic cells. *Annual review of immunology*, 36, 489-517.
12. Johnstone, R. W., Ruefli, A. A., & Lowe, S. W. (2002). Apoptosis: a link between cancer genetics and chemotherapy. *Cell*, 108(2), 153-164.
13. Kaufmann, S. H., & Earnshaw, W. C. (2000). Induction of apoptosis by cancer chemotherapy. *Experimental cell research*, 256(1), 42-49.
14. Shamas-Din, A., Kale, J., Leber, B., & Andrews, D. W. (2013). Mechanisms of action of Bcl-2 family proteins. *Cold Spring Harbor perspectives in biology*, 5(4), a008714.
15. Montero, J., & Letai, A. (2018). Why do BCL-2 inhibitors work and where should we use them in the clinic?. *Cell death and differentiation*, 25(1), 56.
16. Yecies, D., Carlson, N. E., Deng, J., & Letai, A. (2010). Acquired resistance to ABT-737 in lymphoma cells that up-regulate MCL-1 and BFL-1. *Blood*, 115(16), 3304-3313.
17. Sarosiek, K. A., & Letai, A. (2016). Directly targeting the mitochondrial pathway of apoptosis for cancer therapy using BH 3 mimetics—recent successes, current challenges and future promise. *The FEBS journal*, 283(19), 3523-3533.
18. Liu, Q., Osterlund, E. J., Chi, X., Pogmore, J., Leber, B., & Andrews, D. W. (2019). Bim escapes displacement by BH3-mimetic anti-cancer drugs by double-bolt locking both Bcl-XL and Bcl-2. *Elife*, 8, e37689.
19. Liu, Q., Leber, B., & Andrews, D. W. (2012). Interactions of pro-apoptotic BH3 proteins with anti-apoptotic Bcl-2 family proteins measured in live MCF-7 cells using FLIM FRET. *Cell Cycle*, 11(19), 3536-3542.
20. Schneider, A. F. L., & Hackenberger, C. P. R. (2017). Fluorescent labelling in living cells. *Current opinion in biotechnology*, 48, 61-68.
21. Markwardt, M. L., Kremers, G. J., Kraft, C. A., Ray, K., Cranfill, P. J., Wilson, K. A., ... & Rizzo, M. A. (2011). An improved cerulean fluorescent protein with enhanced brightness and reduced reversible photoswitching. *PloS one*, 6(3), e17896.
22. Alexandrov, Y., Nikolic, D. S., Dunsby, C., & French, P. M. (2018). Quantitative time domain analysis of lifetime-based Förster resonant energy transfer measurements with fluorescent proteins: Static random isotropic fluorophore orientation distributions. *Journal of biophotonics*, 11(7), e201700366.
23. Karpova, T., & McNally, J. G. (2006). Detecting Protein-Protein Interactions with CFP-YFP FRET by Acceptor Photobleaching. *Current protocols in cytometry*, 35(1), 12-7.
24. Elder, A. D., Domin, A., Kaminski Schierle, G. S., Lindon, C., Pines, J., Esposito, A., & Kaminski, C. F. (2008). A quantitative protocol for dynamic measurements of

- protein interactions by Förster resonance energy transfer-sensitized fluorescence emission. *Journal of The Royal Society Interface*, 6(suppl\_1), S59-S81.
25. Algar, W. R., Hildebrandt, N., Vogel, S. S., & Medintz, I. L. (2019). FRET as a biomolecular research tool—understanding its potential while avoiding pitfalls. *Nature methods*, 16(9), 815-829.
  26. Cheng, Z., Deen, M. J., & Peng, H. (2015). A low-power gateable Vernier ring oscillator time-to-digital converter for biomedical imaging applications. *IEEE transactions on biomedical circuits and systems*, 10(2), 445-454.
  27. Agronskaia, A. V., Tertoolen, L., & Gerritsen, H. C. (2003). High frame rate fluorescence lifetime imaging. *Journal of Physics D: Applied Physics*, 36(14), 1655.
  28. Chen, H., & Gratton, E. (2013). A practical implementation of multifrequency widefield frequency-domain fluorescence lifetime imaging microscopy. *Microscopy research and technique*, 76(3), 282-289.
  29. Ranjit, S., Malacrida, L., Jameson, D. M., & Gratton, E. (2018). Fit-free analysis of fluorescence lifetime imaging data using the phasor approach. *Nature protocols*, 13(9), 1979.
  30. Li, D. U., Arlt, J., Richardson, J., Walker, R., Buts, A., Stoppa, D., ... & Henderson, R. (2010). Real-time fluorescence lifetime imaging system with a 32× 32 0.13 μm CMOS low dark-count single-photon avalanche diode array. *Optics express*, 18(10), 10257-10269.
  31. Li, D. U., Tyndall, D., Walker, R., Richardson, J. A., Henderson, R. K., Arlt, J., ... & Charbon, E. (2011). Video-rate fluorescence lifetime imaging camera with CMOS single-photon avalanche diode arrays and high-speed imaging algorithm. *Journal of biomedical optics*, 16(9), 096012.
  32. Duval, K., Grover, H., Han, L. H., Mou, Y., Pegoraro, A. F., Fredberg, J., & Chen, Z. (2017). Modeling physiological events in 2D vs. 3D cell culture. *Physiology*, 32(4), 266-277.
  33. Becker, W. (2005). *Advanced time-correlated single photon counting techniques* (Vol. 81). Springer Science & Business Media.
  34. Ghioni, M., Gulinatti, A., Rech, I., Zappa, F., & Cova, S. (2007). Progress in silicon single-photon avalanche diodes. *IEEE Journal of selected topics in quantum electronics*, 13(4), 852-862.
  35. Becker, W. (2014). *The bh TCSPC handbook*. Becker & Hickl.
  36. Micro Photon Devices, “TCSPC measurements with the InGaAs/InP single-photon counter”, June 2014. [online].  
<http://www.micro-photon-devices.com/Docs/Application-note/InGaAs.pdf>
  37. PicoQuant, “TCSPC and time tagging electronics – TimeHarp260”, 2016 [online].  
<https://www.picoquant.com/products/category/tcspc-and-time-tagging-modules/timeharp-260-tcspc-and-mcs-board-with-pcie-interface#specification>
  38. Yavas, S., Machañ, R., & Wohland, T. (2016). The epidermal growth factor receptor forms location-dependent complexes in resting cells. *Biophysical journal*, 111(10), 2241-2254.

39. PicoQuant, "HydraHarp 400, multichannel picosecond event time and TCSPC module with USB interface", April 2019 [online]. <https://www.picoquant.com/images/uploads/downloads/hydrharp400.pdf>
40. Osterlund, E. J., Hirmiz, N., Tardif, C., & Andrews, D. W. (2019). Rapid Imaging of BCL-2 Family Interactions in Live Cells Using FLIM-FRET. In *BCL-2 Family Proteins* (pp. 305-335). Humana Press, New York, NY.
41. Saxton, M. J. (2005). Fluorescence correlation spectroscopy. *Biophysical journal*, 89(6), 3678.
42. De Los Santos, C., Chang, C. W., Mycek, M. A., & Cardullo, R. A. (2015). FRAP, FLIM, and FRET: detection and analysis of cellular dynamics on a molecular scale using fluorescence microscopy. *Molecular reproduction and development*, 82(7-8), 587-604.
43. LaVision BioTec, "TriM Scope II - Specifications," [Online]. Available: <http://www.lavisionbiotec.com/trim-scope-ii-specifications.html>.
44. Visitech International, "VT-Infinity3 2D Array Scanning Laser Confocal Microscope," [Online]. [http://www.visitech.co.uk/assets/vt-infinity-3flyer-\(2\).pdf](http://www.visitech.co.uk/assets/vt-infinity-3flyer-(2).pdf).
45. Thermo Fisher Scientific, "ArrayScan High-Content Systems," 2016. [Online]. Available: <http://www.thermofisher.com/ca/en/home/life-science/cellanalysis/cellular-imaging/high-content-screening/high-content-screening-instruments/arrayscan-hca-readers.html>
46. Tsikouras, A. (2017). *Development of a multifocal confocal fluorescence lifetime imaging microscope for high-content screening applications* (Doctoral dissertation). [https://macsphere.mcmaster.ca/bitstream/11375/21467/2/tsikouras\\_anthony\\_finalsubmission201704\\_PhD.pdf](https://macsphere.mcmaster.ca/bitstream/11375/21467/2/tsikouras_anthony_finalsubmission201704_PhD.pdf)
47. Oreopoulos, J., Berman, R., & Browne, M. (2014). Spinning-disk confocal microscopy: present technology and future trends. In *Methods in cell biology* (Vol. 123, pp. 153-175). Academic Press.
48. Grant, D. M., McGinty, J., McGhee, E. J., Bunney, T. D., Owen, D. M., Talbot, C. B., ... & Kennedy, G. T. (2007). High speed optically sectioned fluorescence lifetime imaging permits study of live cell signaling events. *Optics express*, 15(24), 15656-15673.
49. Margineanu, A., Chan, J. J., Kelly, D. J., Warren, S. C., Flatters, D., Kumar, S., ... & French, P. M. (2016). Screening for protein-protein interactions using Förster resonance energy transfer (FRET) and fluorescence lifetime imaging microscopy (FLIM). *Scientific reports*, 6, 28186.
50. Perkin Elmer, "Opera Phenix High Content Screening System," December 2013. [Online]. Available: [http://www.perkinelmer.com/labsolutions/resources/docs/BRO\\_011289\\_01\\_Opera\\_Phenix.pdf](http://www.perkinelmer.com/labsolutions/resources/docs/BRO_011289_01_Opera_Phenix.pdf)

51. Tsikouras, A., Berman, R., Andrews, D. W., & Fang, Q. (2015). High-speed multifocal array scanning using refractive window tilting. *Biomedical optics express*, 6(10), 3737-3747.
52. Berezin, M. Y., & Achilefu, S. (2010). Fluorescence lifetime measurements and biological imaging. *Chemical reviews*, 110(5), 2641-2684.
53. Caccia, M., Nardo, L., Santoro, R., & Schaffhauser, D. (2018). Silicon photomultipliers and SPAD imagers in biophotonics: advances and perspectives. *Nuclear Instruments and Methods in Physics Research Section A: Accelerators, Spectrometers, Detectors and Associated Equipment*.
54. Vitali, M., Bronzi, D., Krmpot, A. J., Nikolić, S. N., Schmitt, F. J., Junghans, C., ... & Zappa, F. (2014). A single-photon avalanche camera for fluorescence lifetime imaging microscopy and correlation spectroscopy. *IEEE Journal of Selected Topics in Quantum Electronics*, 20(6), 344-353.
55. Walker, R. J., Webster, E. A., Li, J., Massari, N., & Henderson, R. K. (2012, October). High fill factor digital silicon photomultiplier structures in 130nm CMOS imaging technology. In *2012 IEEE Nuclear Science Symposium and Medical Imaging Conference Record (NSS/MIC)* (pp. 1945-1948). IEEE.
56. Richardson, J., Walker, R., Grant, L., Stoppa, D., Borghetti, F., Charbon, E., ... & Henderson, R. K. (2009, September). A  $32 \times 32$  50ps resolution 10 bit time to digital converter array in 130nm CMOS for time correlated imaging. In *2009 IEEE Custom Integrated Circuits Conference* (pp. 77-80). IEEE. *Custom Integrated Circuits Conference* (2009).

## Chapter 3. Synchroscan Streak System

### Paper I – Cross-talk reduction in a multiplexed synchroscan streak camera with simultaneous calibration

Nehad Hirmiz,<sup>1</sup> Anthony Tsikouras,<sup>2</sup> Elizabeth J. Osterlund,<sup>3</sup> Morgan Richards,<sup>2</sup> David W. Andrews,<sup>3,4,5</sup> and Qiyin Fang<sup>1,2</sup>

<sup>1,5</sup>*School of Biomedical Engineering, McMaster University, 1280 Main Street West, Hamilton, Ontario, L8S 4L7, Canada*

<sup>2</sup>*Department of Engineering Physics, McMaster University, 1280 Main Street West, Hamilton, Ontario, L8S 4L7, Canada*

<sup>3</sup>*Department of Biochemistry, University of Toronto, 27 King's College Cir, Toronto, Ontario, M5S 1A8, 9 Canada.*

<sup>4</sup>*Department of Biochemistry and Biomedical Sciences, Main Street West, Hamilton, Ontario, L8S 4L7, Canada*

<sup>5</sup>*Biological Sciences, Sunnybrook Research Institute, University of Toronto, 2075 Bayview Ave., Toronto, Ontario, M4N 3M4, Canada*

Published in Optics Express; 27(16):22606-22614, 2019

Printed with permission

© 2019 Optical Society of America [doi: 10.1364/OE.27.022603]

**Introduction to paper**

This chapter describes how we coupled our multiplexed confocal setup to a commercial inverted microscope, while using the streak camera as a detector (Prototype II). We demonstrated how a 2D-1D fibre array, with alternating fibre lengths, can be used to reduce cross-talk. We present two operation modes for multiplexed detection with the streak camera. These modes are obtained by changing the electronic delay between streak sweep unit and the laser source. We refer to these modes as ‘inward’ sweeping and ‘outward’ sweeping. The two modes have different levels of cross-talk and different temporal windows.

In synchroscan sweeping, the time axis follows a sinusoidal pattern. Time linearization must be performed to extract accurate temporal measurements. We leverage on our multiplexing input to create a virtual grid that can be used to examine the timing profile across the streak. With this approach we experimentally show that there is asymmetry of the transient time effect as a function of sweeping direction. We collect FLIM data for standard Fluorescein and Coumarin-6 solutions. Finally, we examine the performance of the streak when used to image biological samples. We image live MCF-7 expressing mCerulean3-Bcl-XL. FLIM acquisition for live cells required 90 seconds. We attribute the long scan time to the low overall photon detection efficiency of the streak camera and loss of photons when coupling to a fibre array.

Although this work concluded the streak camera is not useful for live cell imaging. It demonstrated that the streak camera can be used as multiplexed detector suitable for ultrafast temporal events. In this setup we were limited by the number of fibres that can be coupled to the streak camera. Thus, we could only achieve a 10×10 multiplexing.

## Contents of Paper I

### Abstract

The streak camera is a picosecond resolution photodetector with parallel input capability; however, the degree of multiplexing is limited by crosstalk and temporal uncertainty in the sweeping field. We introduced a fixed time delay between adjacent fibers to reduce crosstalk in the synchroscan mode. The fixed delay and a tunable electronic delay between the input pulse and the synchroscan unit allows robust separation modes between the streaks, while spatial and temporal nonlinearities can be calibrated in. The efficacy of the design is demonstrated through a 100-fold multiplexed confocal fluorescence lifetime imaging microscope in live cells.

### 3.1 Introduction

The streak camera is a time domain photodetector used for pico- to femtosecond temporal detection from multiple input channels [1,2]. The streak camera is particularly useful for single-shot applications with non-repetitive dynamics such as X-ray free electron laser (FEL) pulse [3], pyrometry [4], pulsed polarimetry [5], and single-shot imaging [6]. Moreover, the streak camera has been applied to repetitive measurements in biomedical applications including fluorescence lifetime imaging (FLIM) [7-9], photoacoustic tomography [10,11], and optical biopsy [12,13]. Comparing to other time-domain detection techniques, the streak camera can measure multiple photons at once with high temporal resolution.

The streak camera achieves its temporal resolution by converting the time measurement into a distance measurement [14]. Briefly, incoming photons are converted into photoelectrons when entering the photocathode. The photoelectrons are amplified and accelerated when passing through a micro-channel plate (MCP) towards a phosphor screen along its traveling direction. A second sweeping electrical field orthogonal to the traveling direction is applied to deflect these electrons. The sweeping field varies in time, such that the deflection field applied to an incoming photoelectron depends on the original photon arrival time at the photocathode. As a result, the measured deflection distance on the phosphor screen corresponds to arrival time of the photon. During a single image acquisition many photon events are registered in the direction of the sweeping voltage, creating a “streak”. As a result, the temporal resolution of a streak camera is measured in the orthogonal deflection direction and typically in the range of femto- to picoseconds.

In a single-scan mode, the sweeping voltage is linearly applied in one direction. Deflection distance is linearly proportional to the arrival time of the incoming photon (linear time axis). The single sweep mode repetition rate is typically limited to a few MHz. To achieve higher repetition rate, the sweeping voltage can be applied in a sinusoidal

fashion in both directions [15], with the sinusoidal field is synchronized with a repetitive pulsed excitation source (synchroscan mode) achieving high repetition rate up to the GHz regime. The challenge with synchroscan mode is that the deflection distance of generated photoelectrons is no longer linear, resulting in a sinusoidal time axis.

Multiple channels can be acquired simultaneously by a streak camera; however, the number of channels is limited by crosstalk between adjacent channels [2,16]. To reduce such crosstalk in single sweep mode, we previously developed a fiber array with alternating fibers in two different lengths [17, 18]. As a result, light signal from adjacent channels reach the detector at different times and spatially separates the generated streaks on the readout image. The spatial separation significantly reduces the crosstalk in adjacent channels, thus allowing a higher degree of multiplexing. In this work, we extend the application of our alternating fiber design to a streak camera with a synchroscan sweeping unit.

The spatial non-uniformity of the electrical field contributes to temporal uncertainty of the measurements. With increased multiplexing, a much larger area of the streak field is used, artifacts from the d of the electrical field will lead to significant nonlinearities in the time domain. For high precision measurements, such errors need to be calibrated and corrected especially when multiplexing is used. Here we present an alternating fiber delay scheme to minimizing the crosstalk between multiplexed input channels, while a separate fiber delay bundle allows correction and calibration under the synchroscan mode. To demonstrate the efficacy of the presented design, we coupled the fiber-optic streak detector to a multiplexed confocal microscope and used it to measure the fluorescence lifetime generated by 100 input channels. We identified asymmetry of the transient time with respect to the sweeping voltage direction and corrected for these artifacts to accurately estimate fluorescence lifetime. The combination of alternating fiber design and temporal corrections pushes the streak camera to its full temporal detection capacity.

## **3.2 Experimental design**

### **3.2.1 Optical system setup**

Figure 1(a) shows the schematic of the implemented design. A 40MHz pulsed diode laser (3 mW, 60 ps LDH-P-C-440M, PicoQuant GmbH, Berlin, Germany) provides excitation at 440 nm. The beam is shaped into a uniform square field and reflected by a dichroic filter (Di01-R442-25x36, Semrock, Rochester, NY) to a microlens array (MLA) (500  $\mu$ m center-to-center pitch, square MLA, SUSS MicroOptics, Neuchâtel, Switzerland). A 10x10 foci array image generated by the MLA is then relayed to the side imaging port of an inverted fluorescence microscope (Axiovert 200, Carl Zeiss AG, Oberkochen, Germany). A 40x oil emersion objective (Fluar 40x/1.30 Oil, Zeiss) is used to create an image of the foci on the sample. The emitted fluorescence signal from each excitation spot is collected. The emission signal passes through the dichroic filter and an emission filter

(FF01-542/27-25, Semrock); then on to a second lenslet array. It is coupled to a 2D-1D fiber optic bundle (0.11 NA, fused silica,  $n = 1.44$ , 50  $\mu\text{m}$  diameter core, 125  $\mu\text{m}$  cladding), which guides the photons to the streak camera (SC-10, Optronis GmbH) through its 100 channel 1D end. The streak camera uses a 40 MHz synchroscan sweeping unit synchronized to the excitation source repetition rate. The readout imager used in the streak camera is a scientific CMOS sensor (sCMOS, PCO edge 5.5, pixel size 6.5  $\mu\text{m}$ ). Confocal images are constructed by raster scanning the generated foci across the sample using a window-based scanner (Fig. 1(a), yellow bars). The window scanners shift the foci image at the microscope's conjugate plane. One scanner shifts the image along the x-axis and the other along the y-axis. The operating principle and characterization of the scanning window design can be found with more details in our previous publication [19].

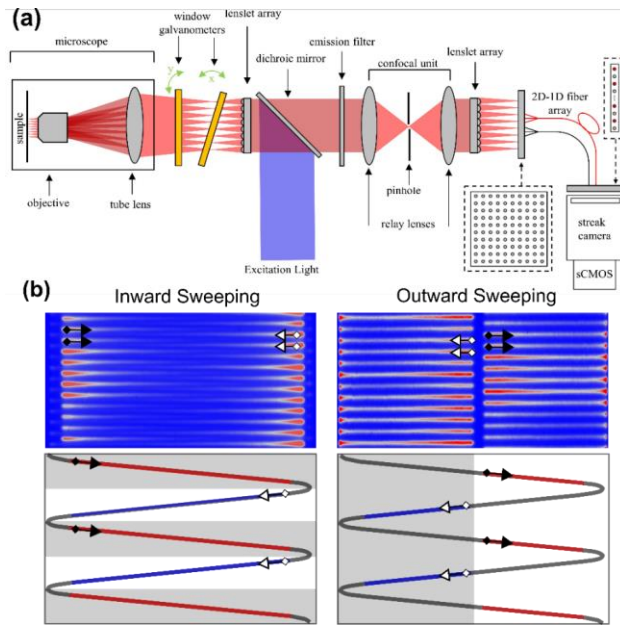


**Fig. 3.1.** (a) Optical setup of the multifocal confocal streak system. (b) Schematic illustrating inward (left) and outward (right) scanning modes. The generated streaks in both modes are illustrated above, with a blue-red pseudoscale (left) representing intensity of generated streaks in that image. The sinusoidal sweeping voltage profile is shown below each image; black and white triangles indicate the start of the streaks from alternating fibers, blue and red lines indicate the near-linear section of the sweep profile, which is used to generate the streaks in the above image. The black and white arrows in the image above correspond to arrows indicated on the sinusoidal profile below.

### 3.2.2 Alternating fiber approach to reduce crosstalk

Even though photons exiting the 1D fiber are tightly focused into the photocathode, the generation of photoelectric activity broadens the readout signal from the sCMOS sensor. There are multiple causes for such broadening including: electron discharge from one channel to another at the MCP, limited spatial resolution of the MCP and phosphor screen, and diffusion of photons generated at the phosphor screen to a larger area. These effects introduce intra-streak crosstalk in a multiplexed setting and limit the number of input channels. Previously, we introduced a 4.8 ns (1 m) difference in the alternating fiber between adjacent channels to split the streak formation across the readout camera, in single sweep mode [17]. For the synchroscan streak camera, the alternating fiber length needs to take into account the period of the sinusoidal sweep and its nonlinearity.

In our current system setup, we use a 40 MHz synchroscan unit, resulting in a 25 ns full sweep cycle (Fig. 1(b)). Adding a 12.5 nanosecond delay between consecutive fibers ensures that photons are split between two halves of the sweep cycle. Therefore, half the photons are collected as the sweeping voltage moves from left to right, whereas the other half are collected as the sweep moves from right to left. Furthermore, this fixed delay between alternative channels can be combined with an electronic delay between the excitation pulse and the synchroscan unit to achieve different streak separation modes. Figure 1(b) shows two of these modes which are referred to as ‘inward sweeping’ or ‘outward sweeping’ mode.

In the inward sweeping mode, the generated streaks start near the turnaround points of the sweeping voltage and are swept towards the center of the streak. In the outward sweeping mode, the streaks start at the center of the sweep and are swept towards the turnaround points. These modes offer flexibility in using the streak for different multiplexed settings. Inward sweeping extends each streak to use the full sweeping range and thus has a larger measurement time window, which is more suitable for longer temporal measurements. However, the streaks have higher amount of crosstalk as the time windows overlap. On the other hand, outwards sweeping is restricted to a shorter measurement window with reduced intra-streak crosstalk.

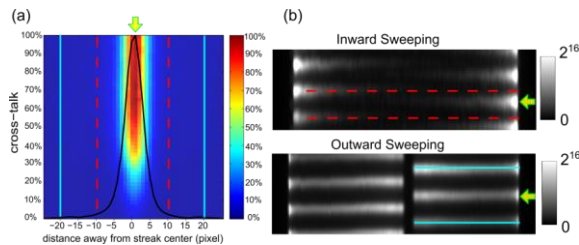


**Fig. 3.2.** (a) Normalized intensity map of a single streak. The black line shows the normalized intensity profile of the maximum intensity point on the streak perpendicular to the sweeping direction. The red dashed lines indicate the positions of the two adjacent streak to the central streak in inward scanning mode. The cyan solid lines indicate the positions of two streaks adjacent to the central streak in the outward scanning mode. This profile is used to determine the crosstalk as a function of distance away from the streak (in pixels). (b) Examples indicating corresponding location of the streaks of interest (yellow arrow) and the adjacent streaks (red dash lines and cyan solid lines). Pixel size: 6.5  $\mu\text{m}$ .

The crosstalk can be quantified by measuring the intensity spread of a single streak to adjacent streaks (Fig. 2(b)). We describe the crosstalk as the percentage of the maximum intensity as a function of distance away from the center of the streak (Fig. 2(a)). We measure this profile at the beginning of the fluorescence-generated streak where the highest crosstalk occurs (Fig. 2(a), black line). Figure 2(b) shows an example of the collected streak images for both inward and outwards modes. In our setup, we measured the distance between two neighboring streaks in the inward mode is about  $9 \pm 1$  pixels (Fig. 2(b), red dashed lines for two streaks adjacent to the central streak). This corresponds to  $\sim 10\%$  crosstalk. The distance between two streaks doubles for the outward mode (Fig. 2(a) and 2(b) cyan solid lines for two streaks adjacent to the central streak). Consequently, the crosstalk in the outward mode is reduced to  $< 1\%$ . Hence, we use outward for fluorescence lifetime imaging in section 4.0.

### 3.3 Image processing and Lifetime estimation

#### 3.3.1 Time axis linearization for a single streak

Time measurement in the streak is recorded as a deflection distance relative to the excitation pulse. In the single sweep mode, the deflection distance of an incoming photon is linearly proportional to its arrival time. In synchroscan sweeping, the time axis follows a sinusoidal pattern. Time linearization for a single streak is achieved by first determining the distance, measured in pixels, between the turnaround points for the sweeping profile. This distance ( $x$ ) can be then converted into time units using:

$$t = \frac{T \cos^{-1}\left(\frac{x-c}{A}\right)}{2\pi} \quad (1)$$

Where  $T$  is the sweep period,  $c$  is the sweep center and  $A$  is the sweep amplitude. These parameters are obtained by accurately localizing the position of the turnaround points for the sweeping profile for streaks generated on the sCMOS sensor. Experimentally, this is achieved by using a continuous light source. Non-synchronization of incoming photons generates line profiles where the intensity is inversely proportional to the deflection time at each pixel. Deceleration of the sweeping voltage at the turnaround points results in larger accumulation of photons, which identifies the

turnaround position. For the unsynchronized light the measured intensity can be modeled as:

$$I_{ideal} \propto \frac{1}{\sin(\cos^{-1}(\frac{c-x}{A}))} \quad (2)$$

Sub-pixel localization of the turnaround points requires estimation of the spread profile of photons coming from a single fiber, whilst the streak camera is set in non-sweeping mode (focus mode). Attempting to linearize the time axis without taking the point spread function (PSF) into account would result in an overcorrection of the non-linearity. Taking the PSF into account, the actual profile is:

$$I_{actual} \propto I_{ideal}(x) \otimes PSF(x) \quad (3)$$

We also corrected for other standard non-uniformities such as differences in the collection efficiency across the sCMOS sensor.

### 3.3.2 Time axis linearization for multiple streaks

When using the entire image sensor to collect a large number of streaks, the effects of temporal and spatial distortions become non-negligible. Barrel distortion (spatial) and transient time (temporal) effects must be corrected to ensure the timing accuracy of the collected photons is consistent for all streaks. In this section, we will present an experimental approach to quantify and correct both of these effects.

The optics that relay the image from the phosphor screen to the sCMOS sensor introduce barrel distortion. In the presence of barrel distortion, streaks at the top and bottom of the image are collapsed into a smaller number of pixels. Since the number of pixels used to capture the streak affects the temporal resolution, barrel distortion must be corrected for a given optical configuration to ensure that every streak is spread across an equal number of pixels at the sCMOS sensor.

Barrel distortion is corrected by imaging a grid of points with known distances between them and taking into account the resulting distorted image, a transformation map is numerically calculated using the following equation:

$$\begin{bmatrix} x_d \\ y_d \end{bmatrix} = \begin{bmatrix} x \\ y \end{bmatrix} \begin{bmatrix} k_1 r^2 + k_2 r^4 + k_3 r^6 \\ k_1 r^2 + k_2 r^4 + k_3 r^6 \end{bmatrix} \quad (4)$$

Where  $(x_d, y_d)$  is the position of the point in the deformed image,  $(x, y)$  is the position of the same point in the corrected image,  $r$  is the radial distance from the center and  $k_1, k_2,$  and  $k_3$  are radial distortion parameters. In most cases parameters beyond  $k_2$  have negligible

contribution and they are omitted [20]. Thus, the barrel distortion correction is determined by numerically solving  $k_1$  and  $k_2$  to estimate the inverse transform.

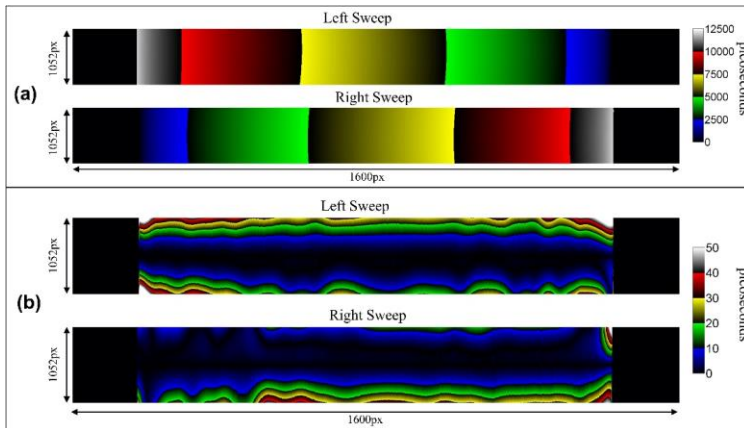


**Fig. 3.3.** (a) Left and right sweep time maps generated by interpolating the simulated grid using a delay generator. (b) Lag time map generated by taking each map and subtracting the time axis for the central horizontal line. Transient time asymmetry is observed when comparing the left map to the right map. Pixel size:  $6.5\mu\text{m}$

The transient time effect occurs because the sweeping voltage, at the center of the wavefront, moves slightly slower than on the edges. This effect results in the non-uniform distribution of the sweeping voltage from the center of the streak tube to the two edges. The grid mapping approach can also be used to correct for transient time effects [21]. However, the input of the streak camera does not permit imaging of a 2D grid. Instead, we simulate a grid by horizontally shifting the line of points generated by the 1D fiber input. This is achieved by simply changing the delay between the excitation source and the synchroscan unit, using fixed delay steps. The  $1 \times 100$  line of streaks is generated during a single acquisition. Using a  $510\mu\text{M}$  quenched Fluorescein dye with a very short lifetime ( $\sim 17$  ps, using  $12.2$  M NaI,  $\text{pH} > 9.0$ ), we generate short spot-like streaks. This is equivalent to estimating the instrument response function (IRF) in the absence of fluorescence signal for each individual fiber [22]. A digital delay generator (Picosecond Delayer, Micro-Photon Devices) is used to incrementally shift the spots by  $0.5$  ns after each acquisition. This process is repeated until the entire  $25\text{ns}$  period is covered resulting in  $50$  delays steps. We locate the position of each spot by its center of mass. The generated  $50 \times 100$  points are split into two sets of  $25 \times 100$  based on their sweeping direction. These two sets were used to distinguish the left sweeping from the right sweeping time maps (Fig. 3(a)). All points are equidistant both horizontally (temporally governed by fixed delay step) and vertically (spatially governed by the 1D input arrangement of the fibers) and can be used to estimate

the spatial and temporal distortion effects. Since the intra-distance between two adjacent fibers at the 1D input of the fiber optic is fixed, the distance between two vertically adjacent points must remain fixed for every vertical line on the simulated grid. This distance can be used in solving Eq. 4 to correct for the barrel distortion. The new grid, corrected for barrel distortion, represents the measured temporal grid for the entire streak. The full temporal map can be generated via interpolation.

Recall that the sweeping voltage is moving left and right in a sinusoidal motion, which means half the streaks generated appear flipped in the opposite direction (Fig. 1(b)). Temporal measurements, discussed in full detail later, indicate a discrepancy between the streaks decaying to the right compared to the left (data not shown). We generated time maps to examine this closer and correct for this effect (Fig. 3(a)). The transient time effect is caused by the lag of the sweeping wavefront at the center of the streak in comparison to the edges. We calculate a lag map by comparing every horizontal line to the central horizontal line in the generated time maps. Figure 3(b) demonstrates the asymmetric profile of the transient time effect with respect to the sweeping direction. These generated time maps can be used to extract the time axis for the streaks generated from fluorescent samples, as shown in the next section. It should be noted that these transient maps need to be measured for individual streak tubes at specific sweeping amplitude.

## 2.4 Multiplexing FLIM with streak camera

The alternating fiber delay scheme is used to collect fluorescence lifetime information from a  $10 \times 10$  multiplexed confocal microscope. FLIM experiments were performed using two standard fluorescent dyes, a fixed *Convallaria* sample, as well as a live cell sample expressing a fluorescently-labeled protein using the outward sweeping mode.

### 2.4.1 FLIM imaging and fluorescence lifetime estimation

As a reference, during each experiment we collected and average 300 streak frames for a solution of 10 $\mu$ M Coumarin-6 dissolved in ethanol with known lifetime of  $2.4 \pm 0.1$  ns [23], 10 $\mu$ M Fluorescein dissolved in 0.1M NaOH solution (pH 10) with a known lifetime of  $4.1 \pm 0.1$  ns [24] and a 510 $\mu$ M quenched Fluorescein with a known lifetime of 27ps [22]. Quenched fluorescein was used to determine the IRF for each individual streak as well as their position on the sCMOS camera. To perform a FLIM scan, the  $10 \times 10$  excitation points were raster scanned across the sample. At each step, a streak image was collected. The sCMOS integration time for each time step was 0.1 s. For standard fluorescent dyes a  $10 \times 10$  scan was acquired (10s total scan time). Each individual streak represents the fluorescence lifetime profile captured by individual foci at that point (Fig. 1(b)). Prior to extracting the lifetime decay from each streak image, background subtraction and barrel distortion corrections were performed. A rectangular region of interest (ROI) was drawn highlighting the boundary of each individual streak (Fig. 4(a)). For each ROI, the intensity

profile was summed and collapsed to a single line producing the non-linearized lifetime profile.

Fluorescent profiles were separated into left decaying and right decaying profiles. This annotation is important to determine the corresponding time map. The generated temporal maps (Fig. 3(a)) were used to extract the time axis for each individual streak. The ROI used for each individual streak was applied to the corresponding temporal map to determine the time axis. The time axis was used to linearize the extracted lifetime decays by Eq. 1. Each decay was fit to a single exponential profile by the Maximum Likelihood Estimation (MLE) algorithm [25] to determine the lifetime per pixel. We restricted the window of fitting to  $< 4.5$  ns (Fig. 4(b)) because the decays reach a turnaround point beyond 4.5 ns, where the time axis collapses to a single point and information about the photon arrival is lost.

The streak image analysis and lifetime extraction were achieved using a custom-built C++ software. ImageJ was used to false-color the lifetime maps and extract the average and standard deviation from each map, as shown in Fig. 4(b).

### 3.4.2 Fluorescence lifetime of standard fluorescent dyes

Figure 4(a) shows examples of normalized decays for  $510\mu\text{M}$  quenched Fluorescein (measured IRF), Coumarin-6 and Fluorescein solutions. Figure 4(b) shows the reconstructed FLIM images for both Coumarin-6 and Fluorescein, where lifetime is represented on a pseudo-color scale in the image and corresponding lifetime histogram (below). As expected, the estimated lifetime for Coumarin-6 was  $2.5 \pm 0.1$  ns. The estimated lifetime for Fluorescein was  $4.0 \pm 0.5$  ns.

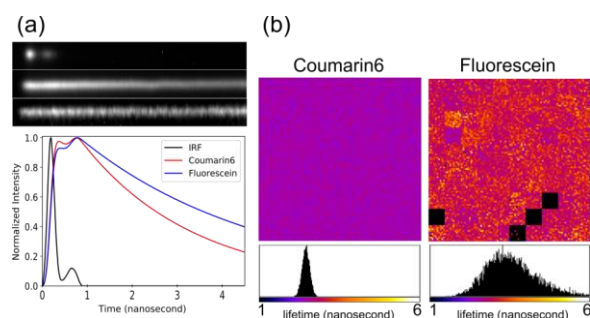


**Fig. 3.4.** (a) Sample streaks for quenched fluorescein (IRF), Coumarin-6 and Fluorescein are shown above. Corresponding linearized lifetime decays for the average of several of these streaks is plotted below. The IRF has a second hump, which is a characteristic of the pulsed diode laser operated at high power [26]. These humps were excluded from the delay experiments used to generate the time maps. (b) Fluorescence lifetime image of Coumarin-6 and Fluorescein solutions. Images were acquired at room temperature using a  $10 \times 10$

confocal scan. The dark squares are a result of dead fibers and were excluded from the analysis.

### 3.4.3 Confocal FLIM imaging of *convallaria* and live breast cancer cells

To demonstrate the confocality of the developed microscope with the streak camera as a multiplexed detector, we performed confocal FLIM imaging for a fixed *Convallaria* sample (*Convallaria Majalis* fixed sample, Leica, Wetzlar, Germany) and live MCF-7 breast cancer cells expressing a protein, Bcl-XL, tagged with a fluorophore, mCerulean3. We will refer to this protein fusion as “mCerulean3-Bcl-XL”.

MCF-7 cells expressing mCerulean3-Bcl-XL were seeded in a 384-well plate (Cell Carrier Ultra, Perkin Elmer) with 5000 cells/well and imaged 24 hours later. Bcl-XL is primarily localized at mitochondria, which are the sharp elongated features surrounding the dark (no protein expression) circular nucleus [27]. The cells were imaged on our streak system as well as on an ISS-Alba fluorescence microscope.

Imaging on the ISS was performed using a 60x water objective with a 445 nm pulsed laser (20MHz, LASOS Lasertechnik GmbH) excitation and a 479-40 bandpass filter. The excitation power was measured to be 4.5  $\mu$ W on average at the objective. The images shown in Fig. 5 (middle and right) were acquired for a 100 $\times$ 100  $\mu$ m field of view using a 265 $\times$ 256 pixels (391 nm pixel size), in 45s. The confocal pinhole unit was set to be 2.5 airy disk units (middle image). On the same microscope, the confocal pinhole was removed from the optical path to obtain a widefield image.

Confocal FLIM imaging was performed using a 40 $\times$  oil objective for a 125 $\times$ 125  $\mu$ m field of view divided into a 300 $\times$ 300 pixels (416 nm pixel size). The excitation power was measured to be 1.15 mW on average ( $\sim$ 11.5  $\mu$ W for individual foci). A 483-35 bandpass emission filter was used. The imaging was acquired using a 30 $\times$ 30 scan at 10 ms integration time resulting in a 90 s acquisition time. At each scan step, 100 streaks were collected. These streaks were converted into fluorescence lifetime decays following the procedure described in section 4.1. At the end of each scan, a FLIM cube (x-position  $\times$  y-position  $\times$  lifetime decay) was reconstructed by combining the fluorescence decays from all pixels.

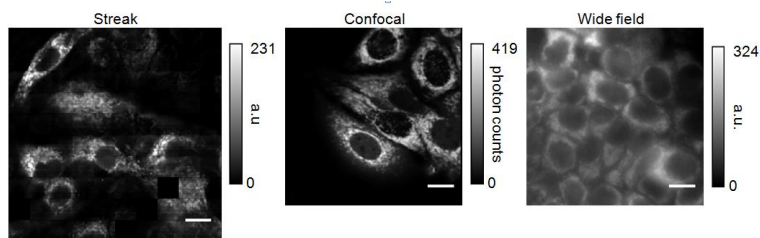


**Fig. 3.5.** Confocal images for live MCF-7 cells expressing mCerulean3-Bcl-XL. Images of the same sample were acquired using our multiplexed streak system (left), compared images acquired on an ISS-Alba in single point confocal mode (middle) and wide field mode (right). Dark squares in the streak image indicate the positions of the dead fibers, mentioned in Fig. 4. Scalar bar: 15  $\mu\text{m}$ .

As expected, compared to the standard fluorescent dyes, *Convallaria* and live cell samples emitted 10 times fewer photons. Estimation of lifetime from samples with poor photon economy was inaccurate on a single pixel basis. To compensate for this effect nearest neighbor binning was applied. A 2D pixel mask was generated by applying mean filtering to the intensity image prior to binning in order to exclude background pixels.

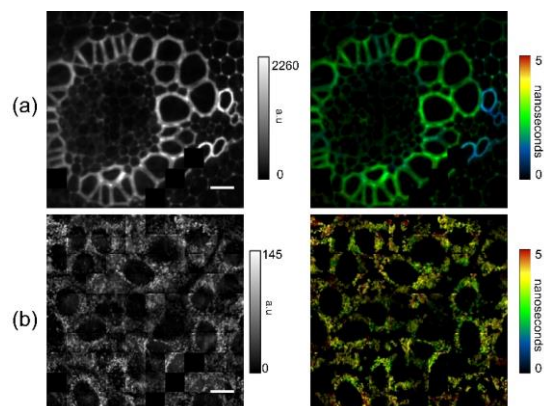


**Fig. 3.6.** Intensity weighted lifetime maps generated by fitting extracted lifetimes from data acquired on the streak microscope. Scalar bar: 15  $\mu\text{m}$ . (a) Confocal FLIM images of *Convallaria* and (b) live MCF-7 cells expressing mCerulean3-Bcl-XL.  $3\times 3$  binning was used for the *Convallaria* FLIM cube, while  $7\times 7$  binning was used for the MCF-7 FLIM cube.

mCerulean3 is an enhanced fluorescent protein with a single-exponential fluorescence lifetime (ex/em: 433/475 nm). In solution, the protein has a lifetime of  $4.1 \pm 0.1$  ns [28], while the expected lifetime of mCerulean3 fused to Bcl-XL is  $3.8 \pm 0.1$  ns [29]. The measured lifetime in live cells expressing mCerulean3-Bcl-XL was  $3.6 \pm 0.3$  ns (Fig. 6(b)); showing a single-exponential fluorescent lifetime. Local changes in lifetime can be seen in a *Convallaria* sample shown in Fig. 6(a). Photon weighted lifetime map of *Convallaria* shows ring like structures have different lifetimes; ranging from 3.1 ns to 1.7 ns. These measurements are in agreement with previously reported values [30].

### 3.5 Discussion and conclusion

Streak camera is one of the fastest photodetectors for measurement of ultrafast events, including up to attoseconds regime [31-32]. Besides its superior temporal resolution, streak camera can also be multiplexed to increase its throughput. Previous work by Qu et al. established the feasibility of synchroscan streak camera multiplexing [2]. In their implementation, the 1D input slit was replaced by an array of pinholes, where each pinhole generates a streak. The cross-talk depends on the intra-pinhole distance and the length of the generated streaks. Qu et al's approach is suitable for measuring short lifetimes, because in their system the streak can only extend a short distance before contaminating the adjacent streak. Our fiber array design with alternating fiber lengths separates light signal from adjacent channels into two different optical paths leading to spatial separation on the readout image sensor. We have demonstrated how this approach extends parallel acquisition capabilities of the streak camera, equipped with a synchroscan mode, to reduce cross-talk.

The design presented here offers flexibility for imaging streaks generated for both long and short time events. The alternating difference in fiber length is chosen to be half of the period of the laser repetition rate. When combined with the synchronization delay, different sweeping modes can be selected based on the signal and the degree of cross-talk between adjacent streaks, offering additional flexibility for users. Our multiplexing scheme can be further modified to create several different operation modes. For instance, introducing more than one delay length in the array can create more intricate streak separation arrangements.

Replacing the linear sweep unit with a synchroscan sweep unit significantly improves the overall acquisition speed; however, spatial and temporal distortion must be corrected. In a multiplexed setting, the generated streaks extend across the entire image sensor. Thus, spatial non-uniformity across the sweeping field produces temporal uncertainty of the measurements. We presented two crucial steps to ensure that temporal measurement conditions are consistent for all the streaks. First, non-synchronous light is used to locate the exact position of the turnaround points for the sinusoidal sweep profile. Second, temporal asymmetry in the sweeping field caused by lag of the field front at the center of the sweep in comparison to the edges is identified. This asymmetry depends on the sweeping direction. We simulated a grid by temporally shifting a 1D array of points while imaging a quenched fluorescein sample, to compute temporal maps used to extract the time axis. Alternatively, if quenched fluorescein is not within the desired excitation/emission window, direct reflection of the excitation light could be used to generate the same temporal map. Here we have also used this simulated grid to extract radial coefficients and correct for barrel distortion effects. Altogether these corrections are essential in a highly robust multiplexed synchroscan streak camera.

To demonstrate the efficacy of the design, we coupled the fiber-optic streak detector to a multifocal confocal microscope and used it to measure fluorescence lifetime images.

Commented [NH2]: Repeated paragraph pointed by Dr. Lo was removed.

FLIM images acquired with the streak system is comparable to those acquired with a commercial frequency domain confocal FLIM instrument in confocal and wide field mode. Looking at the sharpness of structures in the cell, the images taken on the streak system are superior to those taken in wide field mode, however, the ISS-Alba confocal images have better image quality. We have measured the full width half maximum profile of a fluorescent bead to be 510 nm (data not shown). We attribute this broadening in the point spread function to square lenslet aperture effects [33] as the MLAs used in this setup do not have a circular aperture masking applied to their surface.

The current MLA coupling efficiency to the fiber optic bundle is not optimized to fully reject out of focus light. Fluorescence spots imaged onto the fibre bundle are larger than the fibre core. This was caused by an f-number (F#) mismatch between the side port tube-lens for the microscope (F# 19) and the MLA (F# 17). Efficiency of light coupling to a fiber optic is highly dependent on the incident angle [34]. Angular mismatch between the MLA (angular variation  $\pm 1.5^\circ$ ) and the 2D fiber optic end (angular variation  $\pm 0.5^\circ$ ) in our system resulted in varied coupling efficiencies between fiber channels. Variation in coupling produces different signal to noise ratio (SNR) for each fiber, which makes our resulting images appear ‘patched’. This becomes more pronounced when imaging relatively dim samples, such as live cells. Further, lower SNR results in larger variation in the estimated fluorescence lifetime, as can be seen for Fluorescein in Fig. 4(b) (square patched) compared to Coumarin-6, which had much higher SNR.

Besides SNR, there are additional factors contributing to the uncertainty in lifetime estimation, e.g., the ratio of observation window to estimated lifetime. A known requirement for accurate estimation of lifetime using MLE is  $W / \tau > 1.5$ , where  $\tau$  is the lifetime  $W$  is the observation window [35]. The outward sweeping mode decreases crosstalk but it also reduces the observation window to 6.5 ns. Excluding the region at the turnaround points and considering the convolution with the IRF, the observation window containing the exponential decay is only 3.5 ns. Further, our fitting neglects the effect of folding decay at the turnaround points which effects the accuracy of lifetime estimation [36].

Sample photobleaching and the number of photons collected from the sample effect lifetime estimation. The expression of fluorescently labelled proteins in live cells is relatively dim compared to dyes. In addition, these proteins are often localized on membranes and have reduced diffusion rates. In order to collect data from the live cell sample, we extend the acquisition time to acquire sufficient photons. However, extended exposure also increases sample photobleaching, which resulted in the underestimation of mCerulean3 labelled Bcl-XL. In live cells, photobleaching reduces the number of photons collected from the fluorophore-fusion protein of interest while the contribution of auto fluorescence remains unchanged. The ratio of fluorescence signal to auto-fluorescence signal decreases with photobleaching resulting in underestimation of estimated lifetimes. We have replicated this effect on the ISS-Alba microscope, by exposing the cells to higher laser power and slower scan times (see Appendix B).

It should be noted that, in the case of FLIM, time-correlated single photon counting (TCSPC) is the most widely used technique [37-38]. Comparing to TCSPC, where a single photon is recorded within a single pulse, direct sampling technique such as the streak camera has the advantages of recording single short events and high temporal resolution. However, new multiplexing detector technologies have enabled multiple channel TSCPC [38] and sub-100 ps temporal resolution is sufficient for most FLIM applications.

In conclusion, we have developed a time delay scheme in a multiplexing synchroscan streak camera to minimizing the crosstalk between input channels as well as temporal nonlinearity. We have demonstrated the use of this technique in a FLIM setup to measure spatial lifetime variations in a fixed *Convallaria* sample as well as on live MCF-7 cells. Overall, we have demonstrated that the combination of our alternating fiber design and temporal corrections pushes the streak camera to be used as a highly multiplexed detector.

## References

1. Sarantos, C. H., & Heebner, J. E. (2010). Solid-state ultrafast all-optical streak camera enabling high-dynamic-range picosecond recording. *Optics letters*, 35(9), 1389-1391.
2. Qu, J., Li, J., & Niu, H. (2004, July). Fluorescence lifetime imaging microscopy based on a synchroscan streak camera. In *Three-Dimensional and Multidimensional Microscopy: Image Acquisition and Processing XI* (Vol. 5324, pp. 250-256). International Society for Optics and Photonics.
3. Gorgisyan, I., Ischebeck, R., Erny, C., Dax, A., Patthey, L., Pradervand, C., ... & Katayama, T. (2017). THz streak camera method for synchronous arrival time measurement of two-color hard X-ray FEL pulses. *Optics express*, 25(3), 2080-2091.
4. Floyd, E., Gumbrell, E. T., Fyrth, J., Luis, J. D., Skidmore, J. W., Patankar, S., ... & Smith, R. (2016). A high spatio-temporal resolution optical pyrometer at the ORION laser facility. *Review of Scientific Instruments*, 87(11), 11E546.
5. Smith, R. J., & Weber, T. E. (2016). A streak camera based fiber optic pulsed polarimetry technique for magnetic sensing to sub-mm resolution. *Review of Scientific Instruments*, 87(11), 11E725.
6. Liang, J., Zhu, L., & Wang, L. V. (2018). Single-shot real-time femtosecond imaging of temporal focusing. *Light: Science & Applications*, 7(1), 42.
7. Krishnan, R. V., Masuda, A., Centoze, V. E., & Herman, B. (2003). Quantitative imaging of protein-protein interactions by multiphoton fluorescence lifetime imaging microscopy using a streak camera. *arXiv preprint q-bio/0309022*.
8. Campillo, A., & Shapiro, S. (1983). Picosecond streak camera fluorometry-A review. *IEEE Journal of Quantum Electronics*, 19(4), 585-603.

9. Kusumi, A., Tsuji, A., Murata, M., Sako, Y., Yoshizawa, A. C., Kagiwada, S., ... & Ohnishi, S. (1991). Development of a streak-camera-based time-resolved microscope fluorometer and its application to studies of membrane fusion in single cells. *Biochemistry*, *30*(26), 6517-6527.
10. Zint, C. V., Uhring, W., Torregrossa, M., Cunin, B., & Poulet, P. (2003). Streak camera: a multidetector for diffuse optical tomography. *Applied optics*, *42*(16), 3313-3320.
11. Satat, G., Heshmat, B., Raviv, D., & Raskar, R. (2016). All photons imaging through volumetric scattering. *Scientific reports*, *6*, 33946.
12. Masilamani, V., Das, B. B., Secor, J., AlSalhi, M., Devanesan, S., Prasad, S., ... & Alfano, R. R. (2013). Optical biopsy of benign and malignant tissue by time resolved spectroscopy. *Technology in cancer research & treatment*, *12*(6), 559-563.
13. Glanzmann, T., Ballini, J. P., van den Bergh, H., & Wagnieres, G. (1999). Time-resolved spectrofluorometer for clinical tissue characterization during endoscopy. *Review of Scientific Instruments*, *70*(10), 4067-4077.
14. Hamamatsu, "Guide to Streak Cameras," [https://www.hamamatsu.com/resources/pdf/sys/SHSS0006E\\_STREAK.pdf](https://www.hamamatsu.com/resources/pdf/sys/SHSS0006E_STREAK.pdf), (2015).
15. Rieger, K., Caldwell, A., Reimann, O., Tarkeshian, R., & Muggli, P. (2017). GHz modulation detection using a streak camera: Suitability of streak cameras in the AWAKE experiment. *Review of Scientific Instruments*, *88*(2), 025110.
16. Ramanujan, V. K., Jo, J. A., Cantu, G., & Herman, B. A. (2008). Spatially resolved fluorescence lifetime mapping of enzyme kinetics in living cells. *Journal of microscopy*, *230*(3), 329-338.
17. Tsikouras, A., Ning, J., Ng, S., Berman, R., Andrews, D. W., & Fang, Q. (2012). Streak camera crosstalk reduction using a multiple delay optical fiber bundle. *Optics letters*, *37*(2), 250-252.
18. Yuan, Y., Papaioannou, T., & Fang, Q. (2008). Single-shot acquisition of time-resolved fluorescence spectra using a multiple delay optical fiber bundle. *Optics letters*, *33*(8), 791-793.
19. Tsikouras, A., Berman, R., Andrews, D. W., & Fang, Q. (2015). High-speed multifocal array scanning using refractive window tilting. *Biomedical optics express*, *6*(10), 3737-3747.
20. P Drap, P., & Lefèvre, J. (2016). An exact formula for calculating inverse radial lens distortions. *Sensors*, *16*(6), 807.
21. Silbernagel, C. T., Torres III, P., & Kalantar, D. H. (2004, October). A method for analyzing high-resolution time-domain streak camera calibration data. In *Advanced Signal Processing Algorithms, Architectures, and Implementations XIV* (Vol. 5559, pp. 435-442). International Society for Optics and Photonics.

22. Liu, M., Jia, M., Pan, H., Li, L., Chang, M., Ren, H., ... & Xu, J. (2014). Instrument response standard in time-resolved fluorescence spectroscopy at visible wavelength: quenched fluorescein sodium. *Applied spectroscopy*, 68(5), 577-583.
23. Guilford, J., Jaccson, R., Choi, C., & Bergmark, W. R. (1985). Solvent effect on emission yield and lifetime of coumarin laser dyes: requirements for rotatory decay mechanism. *J. Phys. Chem*, 89, 294-300.
24. Sjöback, R., Nygren, J., & Kubista, M. (1995). Absorption and fluorescence properties of fluorescein. *Spectrochimica Acta Part A: Molecular and Biomolecular Spectroscopy*, 51(6), L7-L21.
25. Laurence, T. A., & Chromy, B. A. (2010). Efficient maximum likelihood estimator fitting of histograms. *Nature methods*, 7(5), 338.
26. Poulet, P., Zint, C. V., Torregrossa, M., Uhring, W., & Cunin, B. (2003, July). Comparison of two time-resolved detectors for diffuse optical tomography: photomultiplier tube--time-correlated single photon counting and multichannel streak camera. In *Optical Tomography and Spectroscopy of Tissue V* (Vol. 4955, pp. 154-163). International Society for Optics and Photonics.
27. Kale, J., Osterlund, E. J., & Andrews, D. W. (2018). BCL-2 family proteins: changing partners in the dance towards death. *Cell death and differentiation*, 25(1), 65.
28. Mérola, F., Fredj, A., Betolngar, D. B., Ziegler, C., Erard, M., & Pasquier, H. (2014). Newly engineered cyan fluorescent proteins with enhanced performances for live cell FRET imaging. *Biotechnology journal*, 9(2), 180-191.
29. Liu, Q., Leber, B., & Andrews, D. W. (2012). Interactions of pro-apoptotic BH3 proteins with anti-apoptotic Bcl-2 family proteins measured in live MCF-7 cells using FLIM FRET. *Cell Cycle*, 11(19), 3536-3542.
30. Sparks, H., Görlitz, F., Kelly, D. J., Warren, S. C., Kellett, P. A., Garcia, E., ... & French, P. M. W. (2017). Characterisation of new gated optical image intensifiers for fluorescence lifetime imaging. *Review of Scientific Instruments*, 88(1), 013707.
31. Ossiander, M., Siegrist, F., Shirvanyan, V., Pazourek, R., Sommer, A., Latka, T., ... & Kienberger, R. (2017). Attosecond correlation dynamics. *Nature Physics*, 13(3), 280.
32. Gaumnitz, T., Jain, A., Pertot, Y., Huppert, M., Jordan, I., Ardana-Lamas, F., & Wörner, H. J. (2017). Streaking of 43-attosecond soft-X-ray pulses generated by a passively CEP-stable mid-infrared driver. *Optics express*, 25(22), 27506-27518.
33. Schreiber, P., Kudaev, S., Dannberg, P., & Zeitner, U. D. (2005, August). Homogeneous LED-illumination using microlens arrays. In *Nonimaging Optics and Efficient Illumination Systems II* (Vol. 5942, p. 59420K). International Society for Optics and Photonics.

34. Al-Hamdani, A. H., Rashid, H. G., & Ghayib, Z. R. (2006). Improvement of laser to fiber coupling efficiency using microlens technique.
35. Li, D. D. U., Ameer-Beg, S., Arlt, J., Tyndall, D., Walker, R., Matthews, D. R., ... & Henderson, R. K. (2012). Time-domain fluorescence lifetime imaging techniques suitable for solid-state imaging sensor arrays. *Sensors*, *12*(5), 5650-5669.
36. Leung, R. W. K., Yeh, S. C. A., & Fang, Q. (2011). Effects of incomplete decay in fluorescence lifetime estimation. *Biomedical optics express*, *2*(9), 2517-2531.
37. Moon, S., Won, Y., & Kim, D. Y. (2009). Analog mean-delay method for high-speed fluorescence lifetime measurement. *Optics express*, *17*(4), 2834-2849.
38. Wahl, M., Röhlicke, T., Rahn, H. J., Erdmann, R., Kell, G., Ahlrichs, A., ... & Benson, O. (2013). Integrated multichannel photon timing instrument with very short dead time and high throughput. *Review of Scientific Instruments*, *84*(4), 043102.

## Chapter 4. Multiplexed Confocal System

### **Paper II – Highly multiplexed confocal microscope with a refraction window scanner and SPAD array detector**

**Nehad Hirmiz,<sup>1</sup> Anthony Tsikouras,<sup>2</sup> Elizabeth J. Osterlund,<sup>3</sup> Morgan Richards,<sup>2</sup> David W. Andrews,<sup>3,4,5</sup> and Qiyin Fang<sup>1,2</sup>**

<sup>1,5</sup>*School of Biomedical Engineering, McMaster University, 1280 Main Street West, Hamilton, Ontario, L8S 4L7, Canada*

<sup>2</sup>*Department of Engineering Physics, McMaster University, 1280 Main Street West, Hamilton, Ontario, L8S 4L7, Canada*

<sup>3</sup>*Department of Biochemistry, University of Toronto, 27 King's College Cir, Toronto, Ontario, M5S 1A8, 9 Canada.*

<sup>4</sup>*Department of Biochemistry and Biomedical Sciences, Main Street West, Hamilton, Ontario, L8S 4L7, Canada*

<sup>5</sup>*Biological Sciences, Sunnybrook Research Institute, University of Toronto, 2075 Bayview Ave., Toronto, Ontario, M4N 3M4, Canada*

Accepted

Submitted to Optics Express

**Commented [NH3]:** The title and the contents of the paper have been changed to match revised and accepted final version of the paper

**Introduction to paper II**

In this article we demonstrate that our confocal multiplexing can be extended beyond the  $10 \times 10$  format, which was deployed in the previous paper. We increase our multiplexing by 10-fold and create a  $32 \times 32$  excitation points. In this setup, the 2D-1D fibre coupling array is removed and replaced with 2 relay lenses that can be used to couple to different detectors. The MLAs are picked such that their  $f$ -number matches the lens tube of another commercial microscope (Leica DM 6000B). The later provided experimental confirmation on the versatility of our design to be used as an attachment model for different commercial microscopes.

In this article we refer to our multiplexing scheme as tilt window multiplexing confocal (TWMC). We experimentally show that our system can be coupled to different detectors. We perform confocal imaging using both a CMOS (dense array detector) and a SPAD array (sparse array detector). Using a fixed *Convallaria* sample, we compare the quality of images to those collected on a spinning disk confocal. Finally, we perform live cell imaging for BMK cells expressing mCerulean3-Bcl-XL to evaluate the performance of the system for imaging biological samples.

## Contents of Paper II

### Abstract

#### 4.1 Introduction

Currently, the spinning disk confocal microscope is the most popular fast confocal imaging system. However, these instruments require a high pixel density camera detector, limiting their use in many applications. We have designed a multiplexed confocal scheme that performs raster scanning of a 32x32 foci array in which the output image is stationary after de-scanning. Our system can be coupled to a dense or sparse array detector, making it feasible to rapid time-resolved photon counting, single-photon detection, and apply to some super-resolution techniques.

Over the past decade, confocal microscopy has become a standard imaging tool for life science research, drug discovery, and clinical testing [1]. In a typical laser scanning confocal microscope, a single excitation volume is raster scanned across the sample [2], which is relatively slow for large size images and fast biological processes such as imaging of neural activity [3], volumetric tissue imaging [4], organ on a chip imaging [5], and high content screening [6].

Beam multiplexing offers a solution to increase the frame rate by simultaneously imaging the sample using multiple excitation points. Several multiplexing designs have been presented in the last decade, including Nipkow disk-based spinning disk confocal [7], Spatial light modulators[8] and Microlens Arrays [9].

The Nipkow disk-based approach is currently the most used commercial solution. The Nipkow disk generates a spiral patterned array of foci that uniformly cover the field of view (FOV) as the disk spins. The signal travels back through the same spinning disk and detected by a camera. As a result, although the foci array moves, the detector is stationary and can be read out after integrating the signal light over time. The spinning disc confocal technique offers a fast and straightforward solution for rapid confocal imaging. The design components are simple and low maintenance, making it a preferred choice for high-speed confocal microscopy [10]. As the foci array moves across the detector, typically a 2-dimensional camera with high fill factors is required since the collected signal is not fixed to a singular location. The collected signal is painted across many pixels as the disk spins. This feature prevents coupling the detected signal to emerging sparse pixel detectors, such as a 2D single-photon avalanche photodiode array (SPAD) [11], used in many microscopy techniques. Applications such as time-correlated single-photon counting (TCSPC) FLIM [12], multipoint fluorescence correlation spectroscopy (FCS) [13], entangled photons-based super-resolution microscopy [14], and time-resolved Raman [15] cannot use a spinning disk unit.

The Zeiss LSM series, “AiryScan” multiplexing technology can reach 8x multiplexing by elongating the excitation confocal volume laterally and using a unique array detector organized in a honeycomb, permitting multi-point sampling of the Airy disc (see Tab. 1). Essentially, the signal

from the single large excitation volume is spatially divided at the detector, allowing one to trace the signal to multiple excitation positions on the sample. When coupled to a TCSPC board for FLIM or FCS imaging microscopy, these systems are limited to 2x multiplexing. These systems are excellent for low excitation imaging but are not suitable for rapid time-resolved imaging.

In our previous work [16-17], we developed a tilted window scanner that can move a 10×10 foci array uniformly covering a square FOV. The returned signal is de-scanned by the same scanner making the foci on the detector stationary. A 2D-1D 10×10 fiber array was used to couple the signal to the input slit of a streak camera to achieve fluorescence lifetime imaging (FLIM). In that setup, the scale of multiplexing is limited to about 100 channels due to the resolution of the streak camera and the cross-talk from adjacent fibers [18].

In this work, we further developed this tilt window multiplexing confocal (TWMC) technique with a 32×32 foci array and a SPAD array detector to achieve high-speed confocal imaging. This technique has the potential to be extended to single-photon counting and time-domain applications. We compared our imaging results to a commercial spinning disk confocal system and demonstrated the feasibility of the system in rapid imaging applications.

**Table 4.1. Comparison of multiplexed confocal systems**

Parameter	<b>CSU-10B</b>	<b>TWMC</b>	<b>LSM 980 (CO-8Y)</b>
Detector	Hamamatsu C9100-12	SPC3 SPAD Array	GaAsP-PMT
Detector Quantum Efficiency	>90% (500-650 nm)	25% (320 nm), 50% (400 nm), 14% (650 nm)	30% (400 nm), 45% (550 nm), 40% (650 nm)
Detector Count Rate (1/second)	<1*	300	6000
Image Size (Pixel)	512×512	960×960	512×512
Field of View (μm, 40x Objective)	170 ×170	310×310	92×112
Pixel Size (μm)	0.33	0.32	0.18/0.22 (x/y)
Acquisition Time (seconds)	1.035	0.27	0.104 (maximum)

\* Cooled CCD

## 4.2 Optical Setup

The optical setup is presented in Fig. 1a. Multiplexing is achieved by generating a grid of  $32 \times 32$  foci, using a pair of MLAs (Advanced Micro-optic Systems, APO-Q-P300-R1.83). The output of a pulsed laser (470 nm PicoQuant, LDH-P-C-470) is expanded to a collimated  $10 \text{ mm} \times 10 \text{ mm}$  square beam such that it can cover the whole area of the  $32 \times 32$  MLA ( $9.6 \times 9.6 \text{ mm}^2$  and  $300 \mu\text{m}$  pitch). A dichroic mirror is used to reflect excitation light into the first MLA. This results in a foci array at the focal point of the MLA (3.92 mm after the MLA), which is then relayed through a pair of lenses to the conjugate plane of the microscope (side port, Leica DMI 6000 B). The microscope's tube lens relays the excitation to a Leica 40x objective (HC PL APO 40x/1.30 Oil CS2) is used to focus the excitation array onto the sample. When desired, the relay lenses can be adjusted to accommodate different microscopes tube lenses.

The fluorescence emission returns along the same light path, passing the first MLA, which collimates the signal. The collimated light passes the dichroic filter and is then projected onto a second MLA in order to recreate the grid of foci on the detector. A second pair of relay lenses are used to demagnify the foci array image by a factor of 2 to match the SPAD array pitch ( $150 \mu\text{m}$  pixel pitch). An emission filter (Semrock, FF01-483-25) is positioned between the relay lenses. Finally, the signal grid is collected by either a dense array complementary metal-oxide-semiconductor (CMOS) camera (QMQ042-MG-CM, Ximea, 60% quantum efficiency (QE) at 500-650 nm,  $13 \text{ e}^-$  RMS and effective pixel size of  $11 \mu\text{m}$ ) or a  $64 \times 32$  SPAD sparse detector (SPC3, Micro Photon Devices). For the SPAD detector, the individual pixel aperture serves as the confocal pinhole. For the dense CMOS sensor, the multipoint pinhole is virtually created through the selection of pixels where the tightly focused fluorescence spot has its maximum intensity.

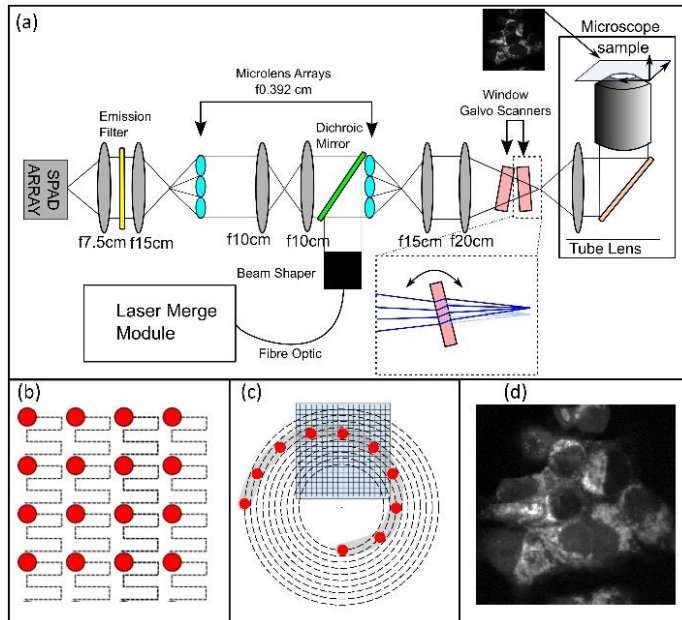


**Fig. 4.1.** The Multifocal Confocal. (a) Schematic diagram of our multiplexed confocal system attached to a microscope equipped with spinning disk unit. (b) Diagram illustrating multiplexed scanning in our Multifocal Confocal setup. Each red circle represents an excitation spot, and the dotted line is the path each spot takes when scanning the sample. Only 4x4 spots are shown for simplicity. (c) Illustration of how confocal scanning is performed in a spinning disk. The square grid indicates the imaging field of view determined by the size of the dense pixel detector. (d) Sample image of live cells scanned obtained on the system by the tilt window scanner.

Two window galvo scanners are positioned near the conjugate plane (Fig 1a, pink). The scanners shift the generated spots along the x and y direction in a raster pattern (Fig 1b). The 32x32 excitation foci are moved across the sample, to generate a confocal image. Since every focal point is moved across a small area of the image, the overall time to scan is reduced drastically.

### 4.3 Results and Discussion

Our setup can be easily extended to perform two channel acquisition. The laser merge module can be used to deliver the excitation pulses from two sources. It is even possible to simultaneously deliver two pulsed sources in an interleaving manner if the pulse rate per channel is adjusted 10 MHz. The dichroic filter can be replaced with a multi-bandpass filter to accommodate different excitations. Currently, we use half of the 64x32 SPC3 array. The other half could be used for simultaneous two-color detection. It is worth

noting that the SPAD array detector has different quantum efficiencies at different wavelengths (see Tab. 1), which would need to be accounted for in 2-color imaging modes.

Uniquely, SPAD array detectors require dedicated circuitry to acquire, store and transmit signal from each pixel. Consequently, spatial constraints limit the density of pixels, and these detectors have a low fill factor. Recent advances in CMOS printing have made it more affordable to create a large pixel array[19]. These sparse array detectors can be used in photon counting applications. Since our multifocal excitation array sparsely scans the sample, it is ideally suited to couple with SPAD array detectors (Fig. 1a).

To evaluate the performance of the image quality, scans of a standard fixed *Convallaria* sample (*Convallaria Majalis* fixed sample, Leica, Wetzlar, Germany) were acquired using both the conventional CMOS camera (Fig 2a) and the SPAD array detector (Fig. 2b). The *Convallaria* sample is excited at 470 nm using the pulsed laser (4 mW). Using a 30x30 step scan at 264  $\mu$ s pixel dwell time resulted in a total scan time of 270 ms. While visually, both images appear to have good quality, the cross-section profile measurements show the SPAD array images have significantly improved the signal to noise ratio (SNR) comparing to the conventional CMOS camera.

To compare the performance of the TWMC technique to that of a spinning disk, a commercially available spinning disk unit (CSU-10B, Yokogawa) was used through the bottom imaging port of the inverted fluorescence microscope. This dual confocal setup allows direct comparison of the speed and image quality of the two platforms, for the same standard fixed *Convallaria* sample. A 491 nm CW laser source (50 mW) is used with the spinning disk unit. To get similar structural details as acquired on multifocal confocal, an integration time of 1.035 s was used. The spinning disk uses an electron multiplying charged-coupled device (EMCCD, Hamamatsu C9100-12, 90% QE at 500-650 nm,  $<1 e^-$  RMS and effective pixel size of 16  $\mu$ m).

The SPC3 is composed of 64x32 SPAD detectors, which can run in single-photon counting or time-gated detection modes (Maximum QE is 50% at 440 nm, and active area diameter of 30  $\mu$ m). We used the single-photon counting mode and half of the sensor area (32x32 pixel). The pixel dwell time is 300  $\mu$ s resulting in a scan time of 307 ms for a 30x30 scan. Fig. 2b shows the confocal image for the *Convallaria* captured using the SPAD array. More details can be observed in Fig. 2b compared to Fig. 2a or c (see magnified images). Altogether, this demonstrates that we can successfully couple this confocal system to a dense pixel detector or a single-photon detector, making this a multifocal confocal attachment more versatile than a spinning disk. It is also worth noting that the EMCCD camera limits the spinning disk images to a 170x170  $\mu$ m FOV when using the 40x objective, while the TWMC images are 320x320  $\mu$ m.

Results presented in Fig. 2 demonstrate that scans for the same fixed sample is reproducible in our developed system. Direct comparison between the three systems was not feasible since the acquisition conditions are different. We next wanted to ensure that the system can be used to image biological samples where the excitation power is limited to avoid photobleaching.

Figure 3. Shows a sample confocal scan acquired using our tilt window multiplexing confocal for live MCF-7 breast cancer cells. The cells express a fluorescently-tagged Bcl-XL protein. Bcl-XL is primarily localized to mitochondria, which can be observed in confocal imaging of sub-cellular organelles [20]. In Fig. 3b, we have magnified a region of this image to highlight a single cell (yellow outline), where the round dark circle within each cell (red outline) are the nuclei. Bcl-XL is not present within the nuclei, as expected, but can be seen in the mitochondria-like structures throughout the cell. These confocal scans are similar to those acquired, for the same cell sample imaged using a commercial single-point confocal microscope (ISS-Alba) [20]. The ISS microscope uses a 445 nm excitation pulsed source (20 MHz, LASOS Lasertechnik GmbH). The excitation power at the objective was measured to be 4.5  $\mu$ W on average. The ISS-Alba uses a single SPAD detector and a 479-40 nm bandpass filter). A 100 $\times$ 100  $\mu$ m FOV was acquired in 33 s (0.5 ms pixel dwell time and a 256 $\times$ 256 scan).

On the commercial ISS-Alba, we determined the excitation power applied by Liu et al., at the objective was 4.5  $\mu$ W on average (data not shown). A 100 $\times$ 100  $\mu$ m FOV was acquired in 33 s (0.5ms pixel dwell time and a 256 $\times$ 256 scan) [20]. On the ISS-Alba, keeping this acquisition time constant, we measured the photobleaching rate for multiple scans at different laser powers. By examining the resulting intensity and lifetime measurements, we determined that powers above 5  $\mu$ W photobleached the sample (data not shown). Therefore, we limited the power on our system to match that of the ISS-Alba for imaging biological samples.

The ISS-Alba microscope uses a 445nm excitation pulsed source (20 MHz, LASOS Lasertechnik GmbH) and a single SPAD detector to measure fluorescence lifetime by single photon counting. Knowing the parameters used on the ISS-Alba for single photon counting, we can calculate that, using the same 5 $\mu$ W excitation on our system, our sample will emit photons at a rate much lower than a single photon per pulse.

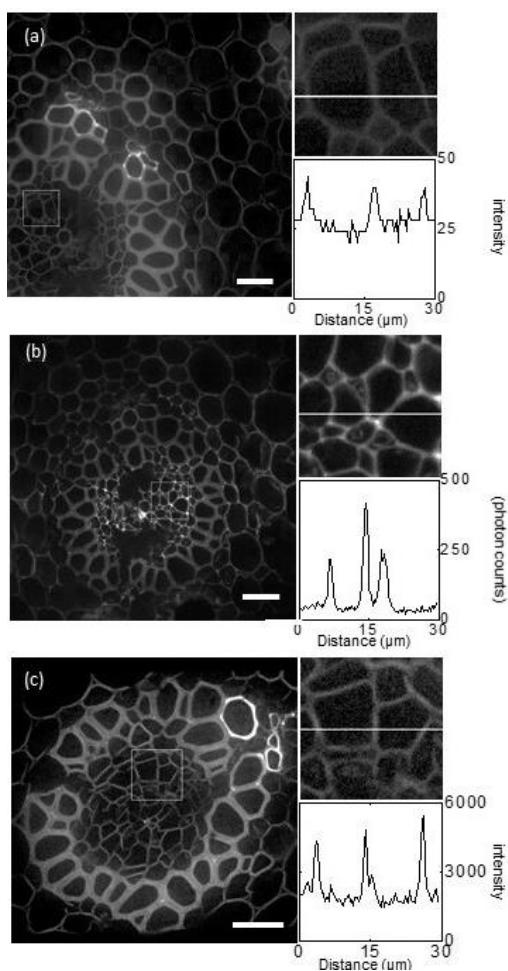


**Fig. 4.2.** Confocal imaging of fixed *Convallaria* slide in Multifocal Confocal and spinning disk unit. Different areas of the same fixed *Convallaria* slide were imaged (a-c). The full image for each is shown to the left. A 30x30  $\mu\text{m}$  area, from each image, is enlarged to the right, with the corresponding line intensity profile. For (a) and (c) the intensity measured in arbitrary units while the SPAD detector measures single photon counts (b). We used the Multifocal Confocal with Ximea CMOS camera (a) and with an SPC3 SPAD detector(b). In (c) we used the Spinning disk confocal. All scale bars are set to 30 $\mu\text{m}$

When imaging biological samples, the laser power for excitation is limited by the tolerance of the fluorophore for photobleaching. The fluorescent protein, mCerulean3, is a mutant of mCerulean designed to have enhanced brightness [21]. However, these fluorophores are incredibly dim in comparison to standard fluorescent dyes. Significant photobleaching of mCerulean3 was observed when the sample was excited with a laser power beyond  $5\mu\text{W}$  (average power measured at the objective, data not shown). Even with this low excitation power, the confocal image in Figure 3a was acquired in only 0.5 seconds on our system. This demonstrates that our multiplexing design is suitable for rapid confocal imaging of biological samples where generated photons are relatively low.

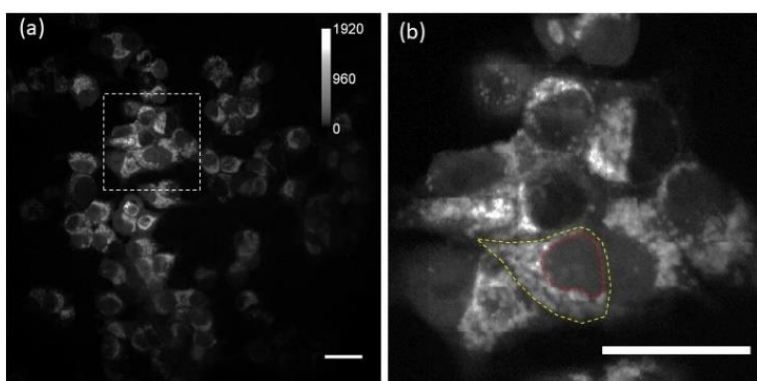


**Fig. 4.3.** (a) Confocal image of live MCF-7 cells expressing mCerulean3-Bcl-XL. Field of view is  $240\times 240\mu\text{m}$  scanned in  $30\times 30$  steps ( $960\times 960$  pixels), in 500 ms total scan time ( $550\mu\text{s}$  pixel dwell time). (b) An enlarged version of the indicated region of interest in (a). Scale bars are set to  $30\mu\text{m}$

The SPAD array offers another advantage when imaging biological samples with high autofluorescence background. The Autofluorescence signal can be gated out by choosing appropriate delay between the excitation pulse and the SPAD. This gating ensures that the performed imaging is less of a fringing modality.

Indeed, there are newer spinning disk designs with improved disk rotation speeds, which can be coupled to scientific CMOS (sCMOS) to image larger FOVs at faster speeds than the CSU-10B used in this comparison. These units, such as the CSU-X1 still require a minimum of 100ms integration time when imaging fluorescent proteins [22]. Our current scanning speed is as fast as these newer spinning disk systems. The TWMC system could be made even faster by operating the window scanners in continuous mode, rather than using a step and stop method.

The presented confocal system is an improved iteration of our previously developed confocal microscope [16]. The first prototype implemented a  $10\times 10$  MLA. With a  $32\times 32$  MLA, we were able to expand our multiplexing by 10-fold ( $32\times 32/10\times 10$ ). Our de-scanned detection

eliminates the need for a dense array detector and can instead be coupled to a sparse array detector such as the SPC3 SPAD array.

In conclusion, our multifocal confocal design provides a simple way to equip existing microscopes with fast confocal acquisition. The de-scanning of the multiplexed detection extends the applications of the proposed design for single-photon imaging applications, such as time of flight imaging, multipoint FCS, and FLIM-FRET.

## References

1. Pawley, J. (Ed.). (2010). *Handbook of biological confocal microscopy*. Springer Science & Business Media.
2. Wang, E., Babbey, C. M., & Dunn, K. W. (2005). Performance comparison between the high-speed Yokogawa spinning disc confocal system and single-point scanning confocal systems. *Journal of microscopy*, 218(2), 148-159.
3. Wevers, N. R., Van Vught, R., Wilschut, K. J., Nicolas, A., Chiang, C., Lanz, H. L., ... & Vulto, P. (2016). High-throughput compound evaluation on 3D networks of neurons and glia in a microfluidic platform. *Scientific reports*, 6, 38856.
4. Wan, H., Yue, J., Zhu, S., Uno, T., Zhang, X., Yang, Q., ... & Ma, Z. (2018). A bright organic NIR-II nanofluorophore for three-dimensional imaging into biological tissues. *Nature communications*, 9(1), 1171.
5. Peel, S., Corrigan, A. M., Ehrhardt, B., Jang, K. J., Caetano-Pinto, P., Boeckeler, M., ... & Kulkarni, G. (2019). Introducing an automated high content confocal imaging approach for Organs-on-Chips. *Lab on a Chip*, 19(3), 410-421.
6. Oppermann, S., Ylanko, J., Shi, Y., Hariharan, S., Oakes, C. C., Brauer, P. M., ... & Andrews, D. W. (2016). High-content screening identifies kinase inhibitors that overcome venetoclax resistance in activated CLL cells. *Blood*, 128(7), 934-947.
7. Oreopoulos, J., Berman, R., & Browne, M. (2014). Spinning-disk confocal microscopy: present technology and future trends. In *Methods in cell biology* (Vol. 123, pp. 153-175). Academic Press.
8. Lane, P. M., Dlugan, A. L., Richards-Kortum, R., & MacAulay, C. E. (2000). Fiber-optic confocal microscopy using a spatial light modulator. *Optics letters*, 25(24), 1780-1782.
9. Eisner, M., N. Lindlein, and J. Schwider. "Confocal microscopy with a refractive microlens–pinhole array." *Optics letters* 23.10 (1998): 748-749.
10. Jonkman, J., & Brown, C. M. (2015). Any way you slice it—a comparison of confocal microscopy techniques. *Journal of biomolecular techniques: JBT*, 26(2), 54.

11. Tsikouras, A., Peronio, P., Rech, I., Hirmiz, N., Deen, M. J., & Fang, Q. (2016, December). Characterization of SPAD array for multifocal high-content screening applications. In *Photonics* (Vol. 3, No. 4, p. 56). Multidisciplinary Digital Publishing Institute.
12. Seo, M. W., Kagawa, K., Yasutomi, K., Kawata, Y., Teranishi, N., Li, Z., ... & Kawahito, S. (2015). A 10 ps time-resolution CMOS image sensor with two-tap true-CDS lock-in pixels for fluorescence lifetime imaging. *IEEE Journal of Solid-State Circuits*, 51(1), 141-154.
13. Colyer, R. A., Scalia, G., Rech, I., Gulinatti, A., Ghioni, M., Cova, S., ... & Michalet, X. (2010). High-throughput FCS using an LCOS spatial light modulator and an 8×1 SPAD array. *Biomedical optics express*, 1(5), 1408-1431.
14. Unternährer, M., Bessire, B., Gasparini, L., Stoppa, D., & Stefanov, A. (2016). Coincidence detection of spatially correlated photon pairs with a monolithic time-resolving detector array. *Optics express*, 24(25), 28829-28841.
15. Kostamovaara, J., Tenhunen, J., Kögler, M., Nissinen, I., Nissinen, J., & Keränen, P. (2013). Fluorescence suppression in Raman spectroscopy using a time-gated CMOS SPAD. *Optics express*, 21(25), 31632-31645.
16. Tsikouras, A., Berman, R., Andrews, D. W., & Fang, Q. (2015). High-speed multifocal array scanning using refractive window tilting. *Biomedical optics express*, 6(10), 3737-3747.
17. Hirmiz, N., Tsikouras, A., Osterlund, E. J., Richards, M., Andrews, D. W., & Fang, Q. (2019). Cross-talk reduction in a multiplexed synchroscan streak camera with simultaneous calibration. *Optics Express*, 27(16), 22602-22614.
18. Tsikouras, A., Ning, J., Ng, S., Berman, R., Andrews, D. W., & Fang, Q. (2012). Streak camera crosstalk reduction using a multiple delay optical fiber bundle. *Optics letters*, 37(2), 250-252.
19. Burri, S., Maruyama, Y., Michalet, X., Regazzoni, F., Bruschini, C., & Charbon, E. (2014). Architecture and applications of a high resolution gated SPAD image sensor. *Optics express*, 22(14), 17573-17589.
20. Liu, Q., Leber, B., & Andrews, D. W. (2012). Interactions of pro-apoptotic BH3 proteins with anti-apoptotic Bcl-2 family proteins measured in live MCF-7 cells using FLIM FRET. *Cell Cycle*, 11(19), 3536-3542.
21. Markwardt, M. L., Kremers, G. J., Kraft, C. A., Ray, K., Cranfill, P. J., Wilson, K. A., ... & Rizzo, M. A. (2011). An improved cerulean fluorescent protein with enhanced brightness and reduced reversible photoswitching. *PloS one*, 6(3), e17896.
22. Schueder, F., Lara-Gutiérrez, J., Beliveau, B. J., Saka, S. K., Sasaki, H. M., Woehrstein, J. B., ... & Jungmann, R. (2017). Multiplexed 3D super-resolution

imaging of whole cells using spinning disk confocal microscopy and DNA-PAINT. *Nature communications*, 8(1), 2090.

## **Chapter 5. Multiplexed Confocal FLIM System**

### **Paper III – Highly multiplexed confocal fluorescence lifetime microscope designed for screening applications**

**Nehad Hirmiz,<sup>1</sup> Anthony Tsikouras,<sup>2</sup> Elizabeth J. Osterlund,<sup>3</sup> Morgan Richards,<sup>2</sup> David W. Andrews,<sup>3,4,5</sup> and Qiyin Fang<sup>1,2</sup>**

<sup>1,5</sup>*School of Biomedical Engineering, McMaster University, 1280 Main Street West, Hamilton, Ontario, L8S 4L7, Canada*

<sup>2</sup>*Department of Engineering Physics, McMaster University, 1280 Main Street West, Hamilton, Ontario, L8S 4L7, Canada*

<sup>3</sup>*Department of Biochemistry, University of Toronto, 27 King's College Cir, Toronto, Ontario, M5S 1A8, 9 Canada.*

<sup>4</sup>*Department of Biochemistry and Biomedical Sciences, Main Street West, Hamilton, Ontario, L8S 4L7, Canada*

<sup>5</sup>*Biological Sciences, Sunnybrook Research Institute, University of Toronto, 2075 Bayview Ave., Toronto, Ontario, M4N 3M4, Canada*

In press

Nature: Light Science and Applications

### Introduction to paper III

In this chapter, we demonstrated how rapid FLIM-FRET imaging can be achieved using our multiplexing approach and a time-gated SPAD array. We used standard fluorescent dyes to optimize the time-gates' position and width. Then we examined the system's accuracy in acquiring FLIM scans for fluorescent samples with known lifetimes. We used a fixed *Convallaria* sample to ensure that our system is well calibrated, both spatially and temporally. We examined the system can be used to measure changes in fluorescence lifetime due to FRET. We imaged HEK293 cells expressing tethered and untethered mCerulean3 and Venus fluorescent proteins.

Our system can be used to measure lifetime changes due to FRET and examine the interactions between mCerulean3-Bcl-XL and Venus-Bad (positive binding control). We demonstrate how this interaction can be inhibited by mutating the BH3 domain (negative binding control).

The large field of view and accurate lifetime estimation allow us to sample many cells with a varying level of PPIs. With as little as 4 Field of views we can construct protein-protein binding curves to extract relative binding affinity constant ( $K_d$ ). We use the extracted  $K_d$ s to examine the effects of two Bcl-XL inhibitors, ABT263 and A1131852 in disrupting the interaction between Bcl-XL and Bad.

In this setup, we did not have an automated stage or environmental control, to perform a full 384 well plate screen. However, our experiments provide a proof of concept on the applicability of our system in screening applications. In theory, we can collect 2 channel FLIM images (donor and acceptor channels) per FOV and 4 FOVs for an entire 384 well plate in less than 40 minutes.

## Contents of Paper III

Commented [NH4]: The reference number annotating was changed from superscript to brackets

### Abstract

Specificity of competitive small molecules can be demonstrated by measuring direct disruption of protein-protein interactions. Knowing a small molecule hits its target is important for predicting therapeutic outcome. Some proteins cannot be purified reliably, making it difficult to quantify on target drug binding in a test-tube. Alternatively, these proteins can be expressed in cells and Fluorescence Lifetime Imaging Microscopy-Förster Resonance Energy Transfer can be used to measure protein-protein interactions. Data acquisition on a traditional single point confocal microscope is very time consuming and only a few samples can be imaged daily. To address this challenge, we developed a 32×32 multiplexed confocal microscope, coupled to single-photon avalanche photodiode array with time gating capabilities for rapid fluorescence lifetime imaging. Here we demonstrate that we can capture a 320×320 μm field of view multi-channel confocal fluorescence lifetime images in less than 1.5 seconds. To provide an experimental model for a proof of concept, we studied the effect of two Bcl-XL inhibitors, ABT263 and A1131852 in disrupting the interaction between Bcl-XL and Bad. With only 4 fields of view, we can get full protein-protein binding curves and clearly show that A1131852 is a more effective compound for disrupting Bcl-XL binding to Bad. Our system could be used to collect binding data for a 384 well plate in less than 38 minutes. Our multiplexed confocal setup is therefore suitable for live cell interaction measurements in screening applications.

### 5.1 Introduction

Cellular mechanisms are carried out by large protein-protein interaction networks. Targeted therapeutics focus on designing small molecules that can disrupt a specific interaction, thereby causing a downstream effect in a biological pathway [1,2]. In drug development, primary high throughput screens are performed to find which compounds out of thousands, give a desired readout. Following up on these ‘hits’, or promising compounds, requires demonstration of the efficacy, as well as testing toxicity in cell-based assays [3,4]. Determining whether a drug truly inhibits its desired target is essential to understand its mechanism and for predicting therapeutic outcome. Selecting the appropriate experiments to test selectivity, reduces the chance of failure at later stages of drug development. Showing that a drug can specifically disrupt the interaction of two proteins is one way to show target selectivity in a protein-protein interaction network.

There are different biophysical approaches for measuring drug binding effects [5]. Isothermal Titration Calorimetry, for example, measures enthalpic changes due to protein-protein or protein-drug binding [6]. Surface plasmon resonance (SPR) measures binding by examining the accumulation of materials on surface immobilized target molecules [7]. However, these methods are all done in a test tube and require purification of the target protein, which may not be attainable.

An alternative is to express two proteins in a cell. Fusion of these proteins to fluorophores allows visualization by fluorescence microscopy. An interaction between the two fusion proteins can be detected by measuring Förster resonance energy transfer (FRET) between the two fluorophores. The rate of energy transfer is inversely proportional to the sixth power of the distance separating the two proteins. This dependency makes FRET a powerful molecular ruler because small changes in the distance result in large changes in the rate of energy transfer. FRET can be measured by a few different approaches [8].

The sensitized emission approach evaluates the increase in the acceptor intensity due to FRET [9]. Alternatively, the acceptor fluorophore can be photobleached, preventing FRET, and the difference in the donor fluorescence intensity before and after photobleaching can be used to quantify FRET [10]. These intensity-based approaches require multiple measurements while correcting for spectral bleed through. The signal to noise must be very high or there will be uncertainty in FRET estimation. Thus, measurement accuracy depends on the concentration of fluorescent molecules in the excitation volume.

Fluorescence lifetime imaging (FLIM) can measure FRET (FLIM-FRET) independently of concentration [11]. Single-photon or time-gated detectors are used to measure the arrival time of photons emitted by the donor fluorophore. The arrival time distribution can be used to determine the fluorescence lifetime, which is the average time a population of fluorescent molecules remains in the excited state before returning to ground state. Fluorescence lifetime is sensitive to environmental changes. For example, in the presence of an acceptor fluorophore, FRET provides the donor molecule with a new route to relax back to the ground state. Thus, FRET causes a decrease in the fluorescence lifetime of the donor. Unlike intensity-based approaches, there is no requirement for spectral correction. FLIM-FRET can be used to measure dynamic interactions over time because there is no sample photobleaching. FLIM-FRET imaging can be done in both widefield and confocal modes. Widefield imaging is fast but doesn't provide the spatial information that can be acquired with confocal [12].

Traditional confocal FLIM-FRET is time-consuming, and not suitable for high throughput screening [13]. Typical pixel dwell times on the order of 100 microseconds to 0.5 milliseconds. For a 256×256 pixels this results in acquisition times in the range of 6.5 seconds to 35 seconds. Confocal scanning creates sub-cellular level resolution interaction maps, which can be useful for determining how and where proteins function. Hundreds to thousands of photons must be collected at each pixel to accurately estimate the fluorescence lifetime. A single excitation point is scanned across the sample to create the image. In order to increase scan speed, the excitation and/or detection can be multiplexed [14-16]. Multiplexing refers to parallel excitation and/or detection of more than one point minimally, across the image sample. Confocal multiplexing methods, such as the spinning disk confocal offer a faster solution. However, spinning disk imaging requires spreading

Commented [NH5]: Dr. Lo comment. Fixed

the collected fluorescence signal on a dense array detector such as a CCD or CMOS, and cannot be coupled to a single photon detector. Furthermore, spinning disk FLIM deploys time-gated multichannel plates (MCPs), which have limited temporal resolution and can only acquire a single time-gate per scan. Spinning disk FLIM systems are currently not commercially available and are built by specialized research groups [17]. To push FLIM-FRET imaging into the early screening pipeline, we need a highly multiplexed confocal system that can be coupled to single-photon counting arrays, which are a rapidly maturing and increasingly affordable technology.

To address this challenge, we developed a multiplexed confocal imaging microscope, which collects the fluorescence signal in a de-scanning mode. The degree of multiplexing in our system is comparable to that of spinning disk. However, our fixed array collection design allows us to couple to not only dense detectors, but also sparse SPAD and fibre optic arrays for signal collection. In our previous work, we demonstrated how a 2D-1D fibre bundle can be used to couple our multiplexed microscope to a streak camera [18]. We addressed the limitations of the multiplexed confocal streak system for live cell imaging. In summary, the low coupling efficiency to the fibre array prevented rapid FLIM acquisition, while crosstalk effects limited the scalability of the design to  $10 \times 10$  multiplexing.

Here, improvements made on our previously published design will be discussed and demonstrated. In summary, we have increased multiplexing by ten-fold in both the excitation and detection. We use  $32 \times 32$  excitation points to scan the sample and couple the collected fluorescence emission to a fixed time-gated single-photon counting SPAD array. Directly coupling to a SPAD array has better coupling efficiency. Our multiplexing solution coupled to the SPAD array detector offers a high resolution and a rapid imaging platform suitable for fast confocal FLIM imaging. Finally, we measure the interaction between two proteins from the Bcl-2 family and demonstrate complex disruption by 2 known targeted small molecules in live cells.

## 5.2 Results

### 5.2.1 Design of the multiplexed confocal FLIM microscope

Excitation multiplexing is achieved by generating a grid of  $32 \times 32$  excitation points, using a pair of microlens arrays (MLAs) (Fig. 1.). The pulsed laser (470 nm PicoQuant, LDH-P-C-470), was chosen to be suitable for excitation of cyan and yellow fluorescent proteins. A beam shaper is used to expand the excitation light such that it can cover the  $32 \times 32$  MLA (Advanced Microoptic Systems, APO-Q-P300-R1.83). This MLA was chosen because it has an anti-reflection coating and an f-number that can be easily matched

to any existing microscope. A dichroic mirror is then used to reflect excitation light into the first MLA. This results in a foci array at the focal point of the MLA, which is then relayed through a pair of lenses to the conjugate plane of the Leica DMI 6000B microscope. The tube lens then relays the image to a Leica 40× objective (HC PL APO 40x/1.30 Oil CS2), which has a large NA which maximizes collection efficiency for live cell samples. The objective focuses the excitation array onto the sample.

When the signal reached the sample, the 32×32 excitation foci are scanned to generate a confocal image. A pair of window-based galvo scanners are positioned near the conjugate plane of the microscope<sup>19</sup>. The scanners shift the generated spots along the x and y direction in a raster pattern. Current scanning is performed in a step-and-stop pattern achieved by calibrating the galvos to move by a specified radial distance when a scan trigger is received. This trigger is controlled by an Arduino microcontroller (Arduino Uno R3). This scanning mode is easier to configure and calibrate but results in slower overall scanning acquisition. Since every focal point is moved across a small area of the image, the overall time to scan is reduced drastically.

The fluorescence emission returns along the same light path, passing the first MLA, which collimates the signal. The collimated light passes through the dichroic mirror and is then projected onto a second MLA in order to recreate the grid of foci. Finally, the signal grid is collected by the SPC3 detector (64×32 SPAD, Micro Photon Devices). A 2:1 pair of relay lenses are used to match the SPC3 150µm pixel pitch. An optical emission filter (Semrock, FF01-483-25) is positioned between the relay lenses to reject any excitation light that had leaked through the system. The SPC3 has a large active pixel area (30µm) which makes it easier to couple to in a multiplexed system. The MLA generates an array with a 300µm pitch. A CMOS sensor (Ximea, QMQ042-MG-CM) was used to confirm the pitch size after the second relay lens was indeed 150µm. This direct coupling to the SPAD array ensures maximal collection efficiency. A 3-axis manual translational stage was used to align the SPC3 array to the generated focal point. We found this setup to be extremely stable over time. The emitted photons are collected between two separate time-gates. Accurate estimation of fluorescence lifetime requires optimizing the position of these gates with respect to the excitation pulse.

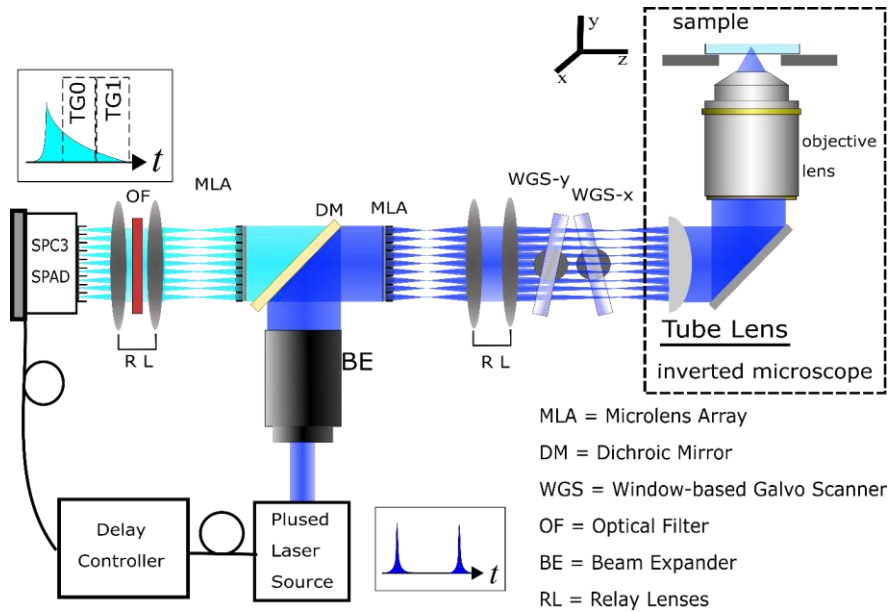


**Fig. 5.1.** The Multifocal Confocal FLIM Setup. Schematic diagram of our multiplexed confocal system attached to an inverted commercial microscope.

### 5.2.2 SPAD gate position and width selection

Rapid fluorescence lifetime determination is achieved by examining the ratio of photons collected within the two time-gates (TG0 and TG1). Prior to doing FLIM imaging, we optimized the location of the time-gates. We first made sure that the collection windows do not include the instrument response function (IRF), measured using a quenched fluorescein sample with a 27 picoseconds fluorescence lifetime, to determine the gate position (Fig. 2). A 2 ns window temporally shifted at 2 ns intervals, was used to precisely locate the IRF position [21]. The delay between the pulsed laser and the SPC3 SPAD array was then adjusted such that the start of the first time-gate was outside the IRF collection region. We also considered the size of the observation window permitted by the SPC3 SPAD detector (a 16 nm collection window) in choosing appropriate gate widths. Two non-overlapping equal size gates, 4 nanoseconds each, were chosen (Fig. 2). The size of a single gate is comparable to the longest expected fluorescent lifetime that was measured (fluorescein dye, 4.0 nanoseconds).

Commented [NH6]: Comment by Dr. Lo

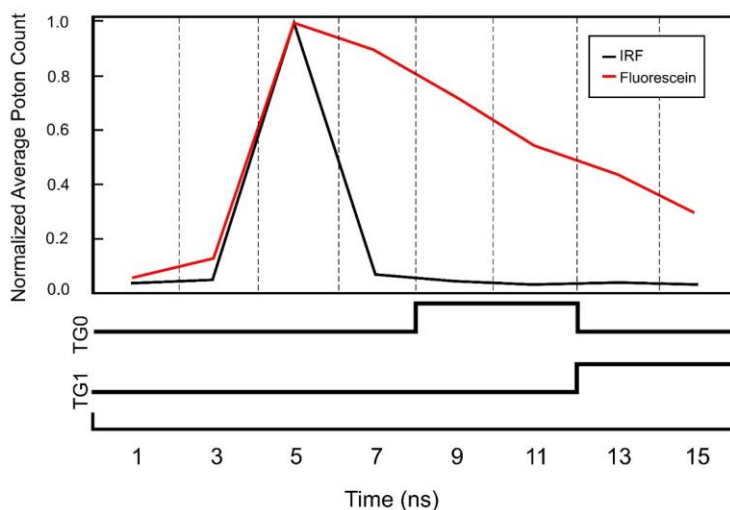


**Fig 5.2.** Time-gates position and size. Normalized profile IRF (black) and Fluorescein in 0.1mM NaOH (red). For rapid lifetime imaging, we choose two time-gates (TG0 and TG1). The position of the two 4ns time-gates is also indicated above the time axis. The permitted observation window for the SPC3 is 16 nanoseconds presented as the time axis limits.

### 5.2.3 Using standard fluorescent samples to calibrate the system

We imaged two standard fluorescent dye solutions with known lifetimes: 10  $\mu$ M Coumarin6 (Sigma Aldrich) dissolved in 100% ethanol (lifetime = 2.5 ns) and 10  $\mu$ M Fluorescein dissolved in 0.1 M Sodium Hydroxide (NaOH) (lifetime = 4.0 ns) (Fig. 3). Without calibration, the estimated lifetimes were  $2.5 \pm 0.2$  ns for Coumarin6 and  $4.0 \pm 0.2$  ns for Fluorescein (Fig. 3c).

We then imaged a fixed *Convallaria* slide (*Convallaria Majalis* fixed sample, Leica, Wetzlar, Germany) (Fig. 4). Lifetimes lower than 2 nanoseconds were measured for the large outer ring structures (Fig. 4), between 1.5-2.5 ns for the smallest innermost ring and between 2-3.5 ns in the intermediate ring structure (thicker borders).

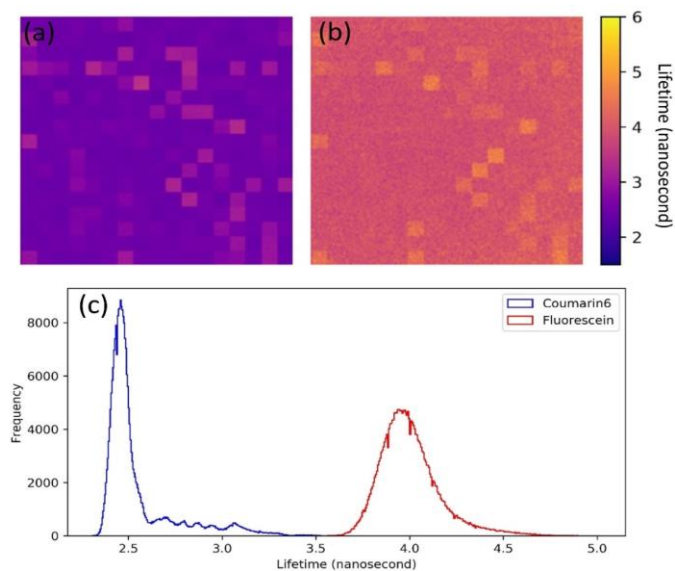


**Fig 5.3.** Lifetime maps of (a) Fluorescein in 0.1M NaOH, 10uM, (b) Coumarin6 in ethanol 10uM. (c) Histogram of both lifetime maps.

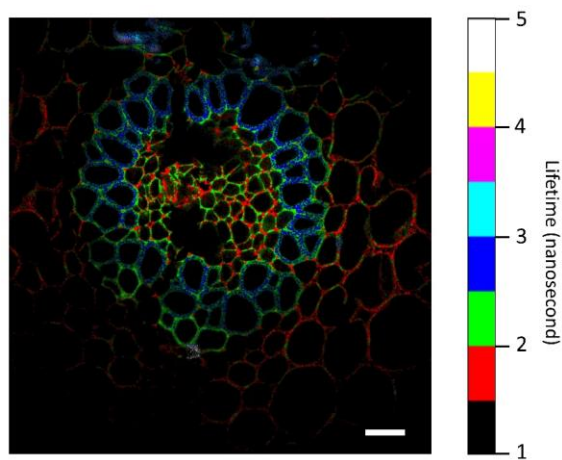


**Fig 5.4.** Photon weighted FLIM confocal image of *Convallaria*. Scale bar 30  $\mu$ m.

#### 5.2.4 FLIM FRET in live cells

To ensure that we can capture changes in lifetime, due to FRET in live cell samples, we first imaged cells expressing our Acceptor:Donor fluorescent proteins. We examined the changes in lifetime when the two proteins are linked together using a short amino acid linker. We transiently transfected Human embryonic kidney 293 (HEK293) cells with mCerulean3 fluorescent protein (donor alone) (Fig. 5a), mCerulean3 and Venus (Donor and Acceptor expressed separately in each cell) (Fig. 5b) and mCerulean3 tethered to Venus by a 13 amino acid linker (FRET standard) (Fig. 5c). The measured lifetimes for these samples were  $3.8 \pm 0.3$  ns,  $3.4 \pm 0.3$  ns, and  $2.9 \pm 0.2$  ns respectively (Fig. 5d).

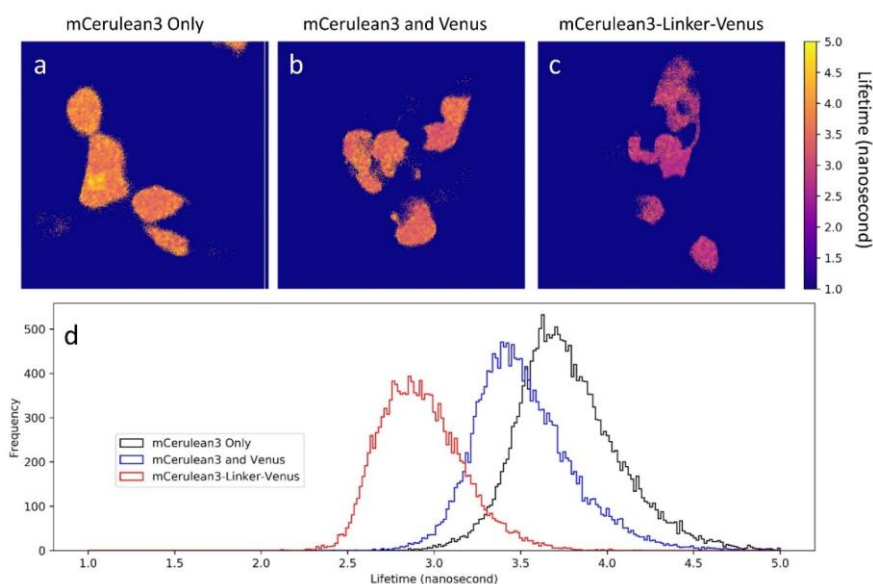


**Fig 5.5.** FLIM imaging of FRET Controls. Lifetime maps of HEK293 expressing mCerulean3 fluorescent protein only (a), mCerulean3 and Venus together (b), and mCerulean3 tethered to Venus using a 13 amino-acids linker (c). (d) shows the lifetime distribution of the three FOVs. The presented maps in (a,b and c) represent a  $78 \times 78 \mu\text{m}$  cropped regions of the full FOVs ( $310 \times 310 \mu\text{m}$ )

Changes in fluorescence lifetime can be caused by many environmental variables such as collisional effects or pH changes. This makes FRET measurements susceptible to generating many false positives. To ensure that changes in lifetime are the outcome of binding events, a negative binding control is prepared and imaged. We imaged the interaction of mCerulean3-Bcl-XL with Venus-Bad via FLIM FRET as shown in Figure 6.

mCerulean3-Bcl-XL is stably expressed in all the cells (see mCerulean3 channel). Venus-Bad (top panel) or Venus-Bad2a (Bottom panel) were transiently transfected in some of the cells (Venus channel). Cells with higher FRET activity have lower lifetimes (mCerulean3-Bcl-XL lifetime channel), as can be seen for cells transfected with Venus-Bad (see decreased lifetime is red) but not for Venus-Bad2a.

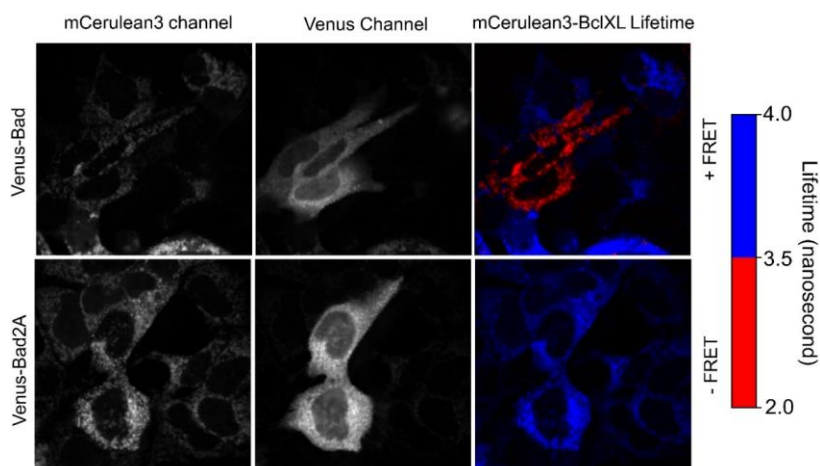


**Fig 5.6.** Confocal FLIM imaging of live MCF-7 stably expressing mCerulean3-BclXL. The top panel shows a zoomed region of cells transiently transfected with Venus-Bad (positive binding control). The bottom panel also shows a magnified region of cells transiently transfected with Venus-Bad2A (negative binding control). In the left panel we see the confocal image for the mCerulean3 channel. In the middle, we see confocal images for the Venus channel. The photon weighted FLIM image of the mCerulean3 is shown in the right panel. The fluorescence lifetime decreases (cells appear in red) when FRET is observed.

Figure 7 (left panel) shows the FRET efficiency maps for cells expressing mCerulean3-Bcl-XL with Venus-Bad (top) and Venus-Bad2A (Bottom). The ratio of the intensity of Venus:mCerulean3 (acceptor:donor) is shown in the left panel and the FRET efficiency in the center panel. To generate a binding curve, FRET efficiency is plotted as a function of the ratio of the acceptor:donor intensity for each pixel (Fig. 7) or region of interest(ROI) [19]. For Venus-Bad, the FRET efficiency rapidly increases with acceptor:donor ratio (sigmoid shape binding curve is observed). On the other hand, a curve is not observed for the Venus-Bad2A protein, indicating no binding to mCerulean3-Bcl-XL. We do observe some increase in FRET at very high expression levels of Venus-Bad2A (high acceptor:donor ratio) due to collisional effects (marked by a red circle).

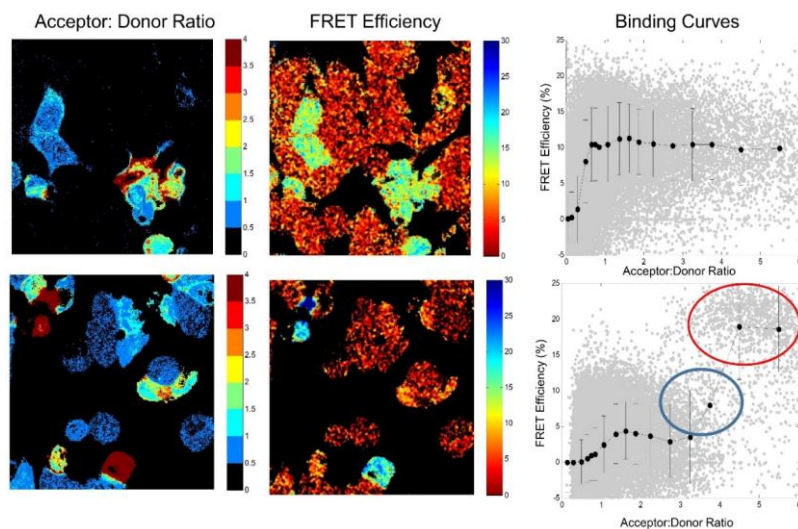


**Fig 5.7.** Binding information extracted from FLIM FRET images for positive and negative binding controls. (left) Acceptor to donor ratio image constructed by dividing acceptor intensity over donor intensity. (center) FRET efficiency map calculated from the lifetime image by comparing to the lifetime of mCerulean3-Bcl-XL without any acceptor. (right) plot of FRET efficiency vs acceptor:donor ratio obtained by plotting the non-zero pixels from FRET efficiency maps(center) and acceptor:donor maps(left) . A rapid increase in FRET efficiency, for the negative binding control, is caused by cells overexpressing Venus-Bad2A (red circle). The blue circle highlights the region where acceptor: donor ratio information is not acquired for a single FOV. The dots with bar are the average and standard deviation for the FRET efficiency at different Acceptor to Donor ratio bins.

Lastly, once we have established that we can measure binding between Bcl-XL and Bad, we tested the efficacy of two small molecules, specifically designed to inhibit the interaction between these two proteins. Binding curves and extracted apparent binding constants are shown in Fig. 8. Our results clearly show that 5  $\mu$ M of A1331852 ( $K_d=5.4$ ) is more effective in inhibiting the interaction between mCerulean3-Bcl-XL and Venus-Bad, than 20  $\mu$ M of ABT263 ( $K_d=0.62$ ).

The FRET efficiency, as seen in Fig. 8, reaches a saturation point indicating labelled donor population that can go through binding with a labelled acceptor has protein is fully bound and can not go through further interactions

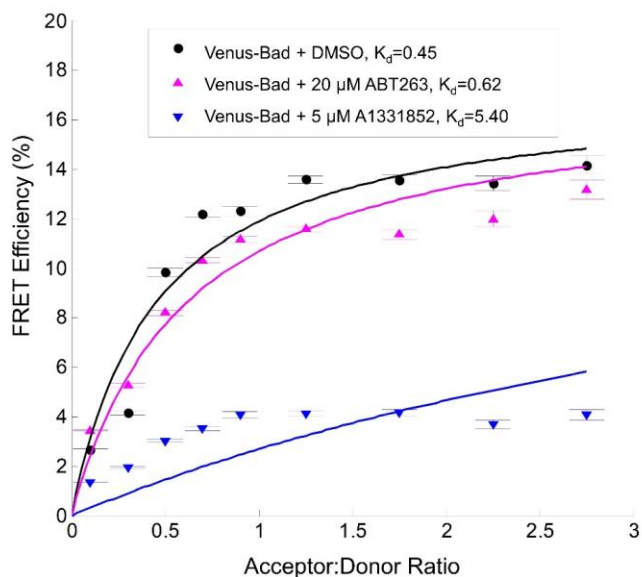


**Fig 5.8.** Effect of two Bcl-2 inhibitors (Abbvie ABT263 and A1331852) on binding between Bcl-XL and Bad. The binding curves were generated by binning data from 4 FOVs. The data points are averages obtained from each bin. The error bars represent the standard error. Each binding curve is fit a single site Hill equation (solid lines) to estimate the apparent  $K_d$ . The untransfected well was treated with dilution media (DMSO) used for the drugs to ensure that the media does not change the lifetime of the donor.

### 5.3 Materials and Methods

#### 5.3.1 Cell culture

All cell lines were incubated at 37°C, 5% v/v CO<sub>2</sub> and handled aseptically under fume hood. MCF7-mCerulean3-Bcl-XL human breast cancer cell line (Ref. 23) cells were passed 1 in 6, every 3-5 days and maintained in Alpha-MEM complete (10% FBS, 1% Penstrep) media + G418 (Wisent, 400-130-IG). HEK293 cells were passed 1 in 10, every 3 days and maintained in DMEM complete (10% FBS, 1% MEM-NEAA, 1% Penstrep) media.

#### 5.3.2 Transfection of MCF-7 breast cancer cells

**Day1:** Media from 10cm dish of confluent (80% covered dish) cells was aspirated. Wash with 3ml PBS. PBS was aspirated and 1ml of 2x Trypsin added and incubated for 2 minutes. 1ml complete media was added. 1ml of resuspended cells in 5ml Alpha-MEM complete media is diluted. A haemocytometer was used to count cells. The cells are then diluted to 160 cells/ $\mu$ l, then added at 25  $\mu$ l volume to each well for 4000 cells per well. One must avoid touching the bottom of the well to avoid washing cells off. A 40  $\mu$ l volume media is then removed, followed by addition of 65  $\mu$ l Alpha-MEM complete which is then followed by 50  $\mu$ l media removal (wash step). The well plate is then left at room temperature for 15 minutes, before returning them to the incubator, to allow the cells to settle at the bottom after the wash step. Cells are incubated overnight.

**Day 2:** 20 to 24 hours after the cells are seeded, cell transfection is carried out. First, a 5ml aliquot of Opti-MEM, TransIT X2 transfection reagent (Mirus, MIR 6005), Alpha-MEM complete media and DNA constructs (including Acceptor-fusion protein of interest and controls) are warmed in 37 $^{\circ}$ C water bath. Several 1.5ml tubes are labelled for each transfectant. In each tube, a 9  $\mu$ l OPTI-MEM (Gibco, 31985-070), 1  $\mu$ l transfectant DNA (100 ng/ $\mu$ l) and 0.3  $\mu$ l TransIT-X2 are added. Each tube is then briefly vortexed then centrifuged by 'burst'. This is followed by an incubation period of 15 minutes at room temperature. A 50  $\mu$ l of Alpha-MEM complete media is added and gently pipetted up/down. 25  $\mu$ l of transfection reaction is added to each well of cells seeded the previous day. Each transfection reaction is enough to transfect 2 wells with 10 $\mu$ l extra to account for any pipetting error. For 'untransfected' control well, 25  $\mu$ l of media plus transfection reagent are added (with no DNA added). Note that some proteins may not be expressed as quickly as others. We have found it can take up to 48 h after transfection to sufficiently express specific acceptor-fusion proteins.

To ensure that transfection has reached completion, wait 3-5 hours before changing the media. Remove media from each well and replace with fresh media to reduce the toxicity of transfection reagent. This is the ideal time to treat with a drug prior to complex formation. BH3 mimetics were diluted 1:1000 (stock solution was 5 mM A1331852 and 20 mM ABT263) in media and used to treat selected wells. A control dilution of the 1:1000 DMSO in media for the 'untransfected' well. The last step is crucial for ensuring that the diluted solvent has no effect on the donor lifetime.

### 5.3.3 FLIM acquisition

The FLIM Acquisition was controlled by a homebuilt interface, written in C++14 (Visual Studio 2015). Time-gate position, width and number of gates are specified and relayed to the SPC3 the C++ API provided with the SPC3. The number of steps per scan is also adjusted and relayed to the galvo drivers.

For FLIM imaging the SPC3 is set in a single time-gated mode. Two 4 nanosecond time-gates (mCerulean3 collection) or a single 8 nanosecond time-gate (Venus collection) were used. The scanning is performed such that the photons are collected for the entire sample at each time-gate.

The 470 nm diode laser was as the excitation source for all FLIM experiments. The emission channel is set by changing the emission filter. For quenched Fluorescein, Fluorescein, Coumarin-6 and the Convallaria standard samples, a 484-25 nm bandpass emission filter was used. For live cell FLIM-FRET measurements, the mCerulean3-Bcl-XL emission was collected using the 384-25 nm bandpass filter (donor channel), while the Venus labelled proteins were imaged using 535-40 nm bandpass filter (acceptor channel). The 470 nm excitation was used to excite the Venus labelled proteins as well. Only a single time-gate (8 nanoseconds width) was used when collecting the fluorescence signal in the acceptor channel. Plotting the intensity of mCerulean3-Bcl-XL only samples in donor channel against acceptor channel indicated a linear cross talk which is corrected for during data analysis.

#### 5.3.4 Image processing and lifetime estimation

The photons collected for each time-gate were saved into a separate image. For a two-gate scan, the two images were first combined to get a total intensity image, which was used to create a background mask. Pixels with low photon counts were excluded from the analysis. The mask was applied to both gated intensity images. For live cell FLIM imaging, a 5×5 pixel binning was applied to improve lifetime estimation. Masked pixels were excluded from the binning in the analysis.

Rapid lifetime determination (RLD) method was used to estimate the fluorescence lifetime. The lifetime image was calculated using:

$$\tau_{RLD} = \frac{-\Delta t}{\ln\left(\frac{D_1}{D_0}\right)} \quad (1)$$

Where  $\Delta t$  is the temporal separation between the beginning of the two gates,  $D_0$  and  $D_1$  are the photon count images at the first and second time-gates respectively.

#### 5.3.5 FRET efficiency and apparent binding affinity $K_d$

Stable expression of mCerulean3-Bcl-XL in the cells results in similar expression levels of the protein from one cell to the other. Transient transfection of Venus-Bad results in more variable expression levels among the cells. This variation in the acceptor:donor

ratio leads to variation in binding observed from one cell to the other, which can be used to extract apparent binding affinities from each sample. Each measured pixel is the result of the signal collected from the confocal volume at that point in the sample. Different pixels have different acceptor:donor ratio. The more acceptor there is the higher the probability for the donor to be in proximity to another acceptor and go through FRET. The changes in the lifetime as a function of acceptor:donor ratio can be used to extract the apparent binding coefficient between two proteins expressed in a cell population. The acceptor:donor ratio is simply calculated by dividing the acceptor intensity image over the donor intensity image. This ratio is plotted as a function of apparent FRET efficiency. Measuring changes in the donor lifetime remains one of the most reliable methods to estimate the FRET efficiency between the donor and the acceptor. The FRET efficiency can be easily calculated using:

$$FRET\ Efficiency\ \% = \left(1 - \frac{\tau_D}{\tau_{DA}}\right) \times 100\% \quad (2)$$

Where the  $\tau_D$  and  $\tau_{DA}$  are the fluorescence lifetimes of the donor in the absence and presence of the acceptor, respectively.  $\tau_D$  can be determined by examining the fluorescence lifetime of cells expressing only the donor labelled proteins. The plot of FRET efficiency as a function of acceptor:donor ratio, generated earlier, is used to extract the apparent  $K_d$ . FRET efficiency vs acceptor to donor ratio plots are binned, based on the acceptor:donor ratio, and fit using a single site hill equation:

$$Y = \frac{B_{max}X}{K_d + X} \quad (3)$$

Where  $Y$  is the observed binding measured using FRET efficiency.  $B_{max}$  is the maximum observed FRET efficiency between the donor and the acceptor (labelled proteins binding saturation limit).  $X$  is the amount of added binding protein which is inferred from the acceptor to donor ratio.  $K_d$  is the apparent binding coefficient, which measures the amount of acceptor to donor ratio observed when the FRET efficiency reaches 50% the  $B_{max}$ . To accurately estimate the changes in binding due to inhibition, the saturation point is fixed to that estimated in the positive control. In our case, the binding of Bcl-XL to Venus-Bad saturated at 15% FRET efficiency (See Fig. 5.8).

#### 5.4 Discussion

We developed a highly multiplexed confocal microscope (Fig. 1) to perform rapid FLIM imaging. In de-scanning mode, the fluorescence signal is coupled to a SPAD array, which is designed for high temporal acquisitions. Accurate measurement of fluorescence lifetime for the scanned samples required optimization of position and size of the SPAD time-gates (Fig. 2). In our system, we used standard fluorescent dyes to determine these parameters. Using overlapping time-gates of different sizes is recognized as the best gating

scheme for estimating lifetime [22]. However, the minimum stable gate size that can be generated by the SPC3 is 2ns and changing this gate size required updating the internal configurations of the SPC3. To simplify the configuration and make data acquisition less computationally demanding we used two contiguous 4ns time-gates.

Even with our straightforward non-overlapping gating choice, we were able to accurately measure the fluorescence lifetime for Coumarin6 ( $2.5 \pm 0.2$ ns) and Fluorescein ( $4.0 \pm 0.2$ ns) (Fig. 3a,b). The excitation light and emission filters are more suitable for imaging Coumarin6, therefore we observed tighter lifetime distribution for Coumarin-6 than Fluorescein (Fig. 3c). However, we note that the tails of both distributions are skewed to overestimate the lifetime. These SPAD pixels appear as square patches with overestimated lifetimes. These patches were expected due to differences in the photon detection response from one SPAD pixel to another (Fig 3a, 3b). Imaging a uniform sample, such as these fluorescent dyes, with a known lifetime allowed for correction of these differences across the detection field.

The fixed *Convallaria* sample (Fig. 4) is very bright and has unique structural properties that allow us to determine visually whether each subscan (squares in the images) align with neighbouring scans sufficiently. Furthermore, the *Convallaria* sample is typically used to demonstrate the feasibility of the system to measure multiple different lifetimes in the same sample. The measured lifetime observations agree with previously reported values for a *Convallaria* sample [23]. In Figure 4 we observe no ‘patching effect’ across the entire photon weighted FLIM image, demonstrating that our lifetime and scanner calibration steps (Fig. 2-3) are effective.

Imaging fluorescent proteins in live cells is a more challenging test for the performance of a FLIM microscope, due to the low photon emission compared to fluorescent dyes. We first tested our system using a standard fluorescent protein assay, where we express the donor alone (Fig. 5a), the donor with the acceptor (Fig. 5b) and the donor-fused to-acceptor (Fig. 5c). The previously reported lifetime of mCerulean3 expressed in cells was  $3.8 \pm 0.3$  ns [24]. In Figure 5d, the mCerulean3 and Venus distribution (blue) is visibly shifted compared to mCerulean3 only (Black). This is expected, due to the increase in random collisions when the donor and acceptor are expressed in the same cell. However, true FRET resulted in a much larger shift, as seen for the mCerulean3-linker-Venus construct (Red compared to black distribution). This demonstrates the feasibility for our system to be used by biologists to measure fluorescent lifetimes of proteins in cells.

Unlike these linker constructs, many proteins have restricted localization in the cell. For example, two proteins may both be localized in one organelle, and in that case, we would expect an increase in collisional effects. Consequently, proper controls are required to interpret FLIM-FRET data. Observed changes in lifetime can only be attributed to binding (FRET) with a negative control experiment: a point mutation in the binding site of

one of the proteins of interest disrupts binding but maintains the same ‘collisional’ effects (same localization in the cell) as the wild type protein.

We demonstrate the use of our system to measure FRET between mCerulean3 (Donor) fused to a protein, Bcl-XL, and Venus (Acceptor) fused to a protein, Bad. These are two members of the Bcl-2 family of proteins, which have been previously shown by FLIM-FRET to bind<sup>23</sup>. Bcl-XL and Bad proteins localize to both the cytosol and mitochondrial outer membrane. For the negative FRET control, we expressed Venus fused to Bad2A, where ‘2A’ indicates two critical residues in the BH3 ligand domain of Bad have been mutated to disrupt binding, as previously reported [25]. In cells Venus-Bad binds to mCerulean3-Bcl-XL and the change in lifetime is very well captured by our system (Fig. 6). There was no observed change in lifetime with the negative control protein, Venus-Bad2A, as previously published by Liu et al.

For screening applications, binding information must be captured by a fast and easy readout. For this purpose, we generate binding curves and need to fit the data to get meaningful information (Fig. 7). In order to fit the data, we convert changes in lifetime to % FRET Efficiency. By comparing the Venus-Bad and Venus-Bad2a curves, we can easily distinguish binding from collisions. Binding curves are usually generated by combining data from many Fields of Views (FOVs), for example, Osterlund et al., required 100, 100×100µm images/sample [26]. On our system, we acquired a large FOV (310×310µm) for two channel FLIM images (mCerulean3 and Venus) in less than 1.5 seconds. We can extract enough information to generate binding curves with as little as 1 FOV (Fig. 7). However, a single FOV may not contain transfected cells that fall in the full range of Acceptor:Donor ratios (for example, Fig. 7, blue circle). Therefore, we recommend taking at least 4 FOV per sample to capture more cells with varying Acceptor:Donor intensity ratios. The 4 images can be acquired in only 6s on our multiplexed system to generate full binding curves. In theory, our system could collect FLIM-FRET binding data for an entire 384-well plate of samples in less than 38 minutes, making it suitable for screening applications.

We used the same binding proteins, BclXL and Bad, to examine two small molecule inhibitors of Bcl-XL, ABT263 and A1331852 (Abbvie). Generated binding curves shown in Fig. 8 were fit to a single site Hill slope binding equation to extract the apparent binding dissociation constant ( $K_d$ ). A lower apparent  $K_d$  means higher affinity of binding. The  $K_d$  was higher with the addition of A1331852, compared to ABT263 or DMSO only. Therefore, A1331852 is a better inhibitor of this interaction (recently shown in Ref. 23). Altogether, this demonstrates that our system could potentially be used to perform a rapid FLIM-FRET screen for drugs that disrupt specific protein-protein interactions.

## References

1. Feng, Y., Wang, Q., & Wang, T. (2017). Drug target protein-protein interaction networks: a systematic perspective. *BioMed research international*, 2017.
2. Hayes, S., Malacrida, B., Kiely, M., & Kiely, P. A. (2016). Studying protein–protein interactions: progress, pitfalls and solutions. *Biochemical Society Transactions*, 44(4), 994-1004.
3. Kepp, O., Galluzzi, L., Lipinski, M., Yuan, J., & Kroemer, G. (2011). Cell death assays for drug discovery. *Nature reviews Drug discovery*, 10(3), 221.
4. Wildey, M. J., Haunso, A., Tudor, M., Webb, M., & Connick, J. H. (2017). High-throughput screening. In *Annual Reports in Medicinal Chemistry* (Vol. 50, pp. 149-195). Academic Press.
5. Rao, V. S., Srinivas, K., Sujini, G. N., & Kumar, G. N. (2014). Protein-protein interaction detection: methods and analysis. *International journal of proteomics*, 2014.
6. Drescher, D. G., Selvakumar, D., & Drescher, M. J. (2018). Analysis of protein interactions by surface plasmon resonance. In *Advances in protein chemistry and structural biology* (Vol. 110, pp. 1-30). Academic Press.
7. Periasamy, A., & Clegg, R. M. (2009). *FLIM microscopy in biology and medicine*. Chapman and Hall/CRC.
8. Algar, W. R., Hildebrandt, N., Vogel, S. S., & Medintz, I. L. (2019). FRET as a biomolecular research tool—understanding its potential while avoiding pitfalls. *Nature methods*, 16(9), 815-829.
9. Elder, A. D., Domin, A., Kaminski Schierle, G. S., Lindon, C., Pines, J., Esposito, A., & Kaminski, C. F. (2008). A quantitative protocol for dynamic measurements of protein interactions by Förster resonance energy transfer-sensitized fluorescence emission. *Journal of The Royal Society Interface*, 6(suppl\_1), S59-S81.
10. Karpova, T., & McNally, J. G. (2006). Detecting Protein–Protein Interactions with CFP-YFP FRET by Acceptor Photobleaching. *Current protocols in cytometry*, 35(1), 12-7.
11. Suhling, K., French, P. M., & Phillips, D. (2005). Time-resolved fluorescence microscopy. *Photochemical & Photobiological Sciences*, 4(1), 13-22.
12. Shotton, D. M. (1989). Confocal scanning optical microscopy and its applications for biological specimens. *Journal of Cell Science*, 94(2), 175-206.
13. An, W. F., & Tolliday, N. (2010). Cell-based assays for high-throughput screening. *Molecular biotechnology*, 45(2), 180-186.

14. Poland, S. P., Krstajić, N., Coelho, S., Tyndall, D., Walker, R. J., Devauges, V., ... & Suhling, K. (2014). Time-resolved multifocal multiphoton microscope for high speed FRET imaging in vivo. *Optics letters*, 39(20), 6013-6016.
15. Pawley, J. (Ed.). (2010). *Handbook of biological confocal microscopy*. Springer Science & Business Media..
16. Mikami, H., Harmon, J., Kobayashi, H., Hamad, S., Wang, Y., Iwata, O., ... & Nagasawa, K. (2018). Ultrafast confocal fluorescence microscopy beyond the fluorescence lifetime limit. *Optica*, 5(2), 117-126.
17. Kumar, S., Alibhai, D., Margineanu, A., Laine, R., Kennedy, G., McGinty, J., ... & Talbot, C. (2011). FLIM FRET Technology for Drug Discovery: Automated Multiwell-Plate High-Content Analysis, Multiplexed Readouts and Application in Situ. *ChemPhysChem*, 12(3), 609-626.
18. Hirmiz, N., Tsikouras, A., Osterlund, E. J., Richards, M., Andrews, D. W., & Fang, Q. (2019). Cross-talk reduction in a multiplexed synchroscan streak camera with simultaneous calibration. *Optics express*, 27(16), 22602-22614.
19. Tsikouras, A., Berman, R., Andrews, D. W., & Fang, Q. (2015). High-speed multifocal array scanning using refractive window tilting. *Biomedical optics express*, 6(10), 3737-3747.
20. HIRMIZ, N., TSIKOURAS, A., OSTERLUND, E. J., RICHARDS, M., ANDREWS, D. W., & FANG, Q. Multiplexed confocal microscope with a refraction array scanner and SPAD array detector. *Image*, 300, 6000.
21. Liu, M., Jia, M., Pan, H., Li, L., Chang, M., Ren, H., ... & Xu, J. (2014). Instrument response standard in time-resolved fluorescence spectroscopy at visible wavelength: quenched fluorescein sodium. *Applied spectroscopy*, 68(5), 577-583.
22. Tsikouras, A., Peronio, P., Rech, I., Hirmiz, N., Deen, M. J., & Fang, Q. (2016, December). Characterization of SPAD array for multifocal high-content screening applications. In *Photonics* (Vol. 3, No. 4, p. 56). Multidisciplinary Digital Publishing Institute.
23. Krstajić, N., Poland, S., Tyndall, D., Walker, R., Coelho, S., Li, D. D. U., ... & Henderson, R. (2013, May). Improving TCSPC data acquisition from CMOS SPAD arrays. In *European Conference on Biomedical Optics* (p. 879709). Optical Society of America.
24. Liu, Q., Leber, B., & Andrews, D. W. (2012). Interactions of pro-apoptotic BH3 proteins with anti-apoptotic Bcl-2 family proteins measured in live MCF-7 cells using FLIM FRET. *Cell Cycle*, 11(19), 3536-3542.
25. Liu, Q., Osterlund, E. J., Chi, X., Pogmore, J., Leber, B., & Andrews, D. W. (2019). Bim escapes displacement by BH3-mimetic anti-cancer drugs by double-bolt locking both Bcl-XL and Bcl-2. *Elife*, 8, e37689.

26. Osterlund, E. J., Liu, Q., & Andrews, D. W. (2015). The use of FLIM-FRET for the detection of mitochondria-associated protein interactions. In *Mitochondrial Medicine* (pp. 395-419). Humana Press, New York, NY.

## Chapter 6. Conclusions and Future Work

The development of a highly multiplexed confocal fluorescence lifetime imaging microscope, designed for screening applications, has been presented in this thesis. Here I provide a summary of the presented work, discuss some of the shortcomings of the design, and propose future work.

### 6.1 Summary

Milestones presented in this thesis include:

- 1- Used a 2D-1D fibre optic array to multiplex detection to a streak camera with a synchroscan unit. We established two different acquisition modes using this system, allowing the user to chose settings for reduced crosstalk or a larger temporal window.
- 2- Developed a calibration method to account for non-linearity of the time axis on a streak camera. Using our calibration, we were able to examine the temporal profile across the entire streak sensor and discovered asymmetry in the transient time effect as a function of the sweep direction. Our calibration method will be a useful tool for any system that has been designed with a streak camera as a multiplexed detector.
- 3- Designed and built a third prototype, of a highly multiplexed confocal microscope. Achieved a 10-fold increase in multiplexing compared to our previous design. We demonstrated that our system can be coupled to both sparse and dense array detectors. This work is important because we achieved the same level of multiplexing as a spinning disc confocal system, using an alternate multiplexing approach that allows for signal de-scanning.
- 4- We coupled our third prototype to a time-gated SPAD array and demonstrated that accurate lifetimes can be measured for standard and biological samples in less than 1 second. This meets the need for screening applications.
- 5- Compared the efficacy of two anti-cancer BH3 mimetic drugs, for disrupting Bcl-2 family protein-protein interactions in live cells. We did this only using 4 fields of view, demonstrating that compound sampling can be done in seconds.
- 6- We demonstrate with a few samples that we can image rapidly, however; we were unable to perform a full screen. There are still requirements that need to be met before this instrument could be marketed for industrial and academic screening purposes

### 6.1 System Resolution – Theoretical and Experimental Consideration

In a confocal system, the full numerical aperture ( $NA$ ) of the objective lens is reached when the back aperture is filled [1]. For the Leica HC-PL-APO 40x objective, used in our system, the back aperture has a diameter ( $D_{back\ aperture}$ ) of 20 mm. Using a 200 mm tube lens, one can determine the size ( $w$ ) of the focused excitation source at the conjugate plane of the microscope to fill the back aperture.

$$w = \frac{4\lambda f}{\pi D_{back\ aperture}} \quad (1)$$

Where  $f$  is the focal length of the tube lens. Using Eq. 1, we can determine that the excitation beam must be focused onto a  $\sim 3\ \mu\text{m}$  point. Using the same equation, we can calculate the spot size generated by an individual microlens is  $\sim 4\ \mu\text{m}$  (focal length = 3.92 mm, microlens aperture = 0.3 mm). Thus, the size of the light at the back aperture of the objective lens is reduced to  $\sim 15\ \mu\text{m}$ .

The partial filling of the back aperture will result in a reduction of the effective NA ( $NA_{effective}$ ).  $NA_{effective}$  can be determined using:

$$NA_{effective} = \frac{n}{\sqrt{(2f_{objective}/D_{back\ aperture})^2 + 1}} \quad (2)$$

Where  $n$  is the refractive index of the immersion oil and  $f_{objective}$  is the focal length of the objective lens.  $NA_{effective}$  is calculated to be  $\sim 1.19$  ( $n = 1.5$ ,  $f_{objective} = 5.7\text{mm}$ ) in our multiplexed confocal setup. From this we can conclude that there is  $\sim 10\%$  loss in resolution due to multiplexing.

Ignoring the cross-talk effects between neighbouring spots [2], we can determine the theoretical resolution limit of the system using:

$$LFWHM_{conf} = 0.5 \frac{\lambda_{em}}{NA_{effective}} \quad (3)$$

Where  $LFWHM_{conf}$  is the fullwidth half maximum of the diffraction limited spot in a confocal microscope and  $\lambda_{em}$  is the emission wavelength. Assuming that the  $\lambda_{em}$  is equal to 500 nm, then our resolution limit is  $\sim 210\ \text{nm}$ .

The system can operate at this resolution if the pinhole size is set to 1 Airy Unit, which is estimated using:

$$1\ \text{Airy Unit} = 0.61 \frac{\lambda_{em} M_{total}}{NA_{effective}} \quad (4)$$

Where  $M_{total}$  is the total magnification in the system up to the pinhole element. From Eq. 4, we can determine that the ideal pinhole in our system should be set to 20 micrometer ( $M_{total} \sim 0.6780$  in our system). The active area of the SPC3 SPAD array works as a fixed

pinhole with a size of 30 $\mu$ m. Our current pinhole setting is a 1.5 Airy Units. We can calculate the effective resolution using the following equation:

$$LFWHM_{effective} \cong 0.67 \frac{\lambda_{em}}{NA_{effective}} \sqrt{1 + AU^2} \quad (5)$$

Where  $AU$  is the size of the pinhole in Airy Units. Using Eq. 5 we can approximate the effective resolution of the system to be ~508 nm. These approximations are very close to the full width at half maximum measurements determined for small subcellular structures like the mitochondria.

### 6.3 Additions Needed to Make the System Screen Ready

Our current prototype is a proof of concept. We demonstrate with a few samples that we can image rapidly, however; we were unable to perform a full screen. There are still requirements that need to be met before this instrument could be marketed for industrial and academic screening purposes.

#### Necessary additions

##### *Stage automation, environmental controls and immersion objective*

The next step is to program the automated stage for position series acquisition and add an environmental chamber. Since we are currently using a Leica DM 6000B inverted microscope, I would install Leica's "Live On Stage" attachment, designed for this purpose [3]. This would require a CO<sub>2</sub> tank and water reservoir. The Live On Stage attachment encases the entire stage, which eliminates the need for a dark room. This attachment can be controlled through the microscope application programming interface to set the desired temperature (25 °C) and CO<sub>2</sub> levels (5 %). The experiments are carried at 25°C, consistent with historical experiments done by Liu et al. [4]. Though the cells are typically kept at 37°C in the incubator, we operate at 25°C because there is reduced collisional quenching, and the lifetime of mCerulean3 is 0.2ns longer, which extends the dynamic range of FRET detection.

In order to do full plate scans, typically a water objective is employed because this is replenishable over time. We are currently using an oil objective, but we have a water objective on the same system. For screening purposes, we need to add a specialized collar and source for water replenishment. Leica offers "The Water Immersion Micro Dispenser", designed for screening applications, which comes with a collar and dispenser [5]. Another important feature for live cell imaging across full plates is automated focus control. Our system is already equipped with this feature.

##### *Multi-channel acquisition*

Measuring proteins binding in the cell means having the donor and acceptor-fusion proteins expressed in the same cell. Therefore, our system is not realistically useful until we provide dual channel imaging. Our excitation source is delivered to the system using a fibre optic. Currently, we are using a single excitation pulsed laser to image both mCerulean3 and Venus. The two channels are acquired separately, which increases the acquisition time. We can improve this by delivering two pulsed sources in an interleaving fashion. This can be achieved by delaying one of the pulses in time (equal to half of the distance between two consecutive pulses). A multi-bandpass filter can be used instead of the current dichroic, while the second half of the SPC3 can be used to measure the added channel.

#### ***Body encasement***

We have already designed a simple encasement for the multiplexed attachment. This occupies a large footprint, making the system bulkier than needed. Future improvements can include folding some of the optical paths to reduce this footprint.

#### ***Scanner improvement***

Raster scanning is currently done in a 'step and stop' mode. The galvo scanners are programmed to move by a set radial distance, in steps. This mode is easier to implement however it limits the acquisition speed. The galvo scanners are designed for continuous scanning and in order to implement this in our system the galvo must be calibrated to synchronize to the detector. This will require additional programming. Continuous scanning will improve the imaging speed.

#### ***Software***

As discussed in chapter 4, our current prototype uses a simple graphical user interface (GUI) built in C++. The software can be used to set time-gate position, width and scan parameters. The user can also choose a saving directory but currently has to identify the file name. This software is not suitable for complex screen acquisitions and requires significant improvements. These include adding features for programmed position series, field of view selection, time series, laser power and an environmental control panel. Within this software, the user should be able to perform quick lifetime estimation to test system performance prior to starting sample acquisition. Other useful features include optical configuration controls. Another important feature for screening is the inclusion of metadata in the acquired images. This includes information about the well position, field of view, scan time and acquisition parameters. Standard formats such as the open microscopy tiff (OM-TIFF) can be selected for this purpose.

#### ***Extra features to add***

#### ***SPAD array improvements***

The SPC3 SPAD array can only acquire two time-gates at once. Although, we can accurately measure lifetimes using rapid lifetime determination approach (RLD), we are still not sampling the entire fluorescence decay. Extracting quantitative binding information requires analyzing the full fluorescence decay, which can be collected using advanced detectors like the Photon Force 32 (PF32) TCSPC SPAD. As mentioned in chapter 1, we failed to couple our system to the PF32 TCSPC SPAD array due to its low fill factor. We expect, adding a custom built microlens array will solve this issue by focusing the collected light on the small active area of these pixels [6]. Each microlens will be directly attached to the SPAD pixels.

Another limitation to the SPC3 detector used in our third prototype, is low detection efficiency in the far-red wavelengths (14% efficiency at 650nm, which decreases towards infrared region). This will impact the speed of our system in applications such as deep tissue imaging, where red and far red proteins are used [7]. New SPAD designs are needed to address this issue in the future [8].

#### *Alternative imaging modalities*

While the system was designed for FLIM applications, our multibeam design has potential use for other applications. With a single photon counting detector multipoint fluorescence correlation spectroscopy could be performed [9]. Our lab also plans to test newer SPAD arrays (with denser pixel format) that can be used for hyperspectral FLIM imaging. The space between the sparse focal points can be used to spectrally disperse the collected signal, using a diffraction element (most likely a prism). This will enable our system to perform rapid hyperspectral imaging (with or without FLIM).

One limitation to acquiring FLIM instrumentation for many labs is the high cost of pulsed lasers. Our multiplexed confocal attachment can be modified to perform Frequency-domain FLIM. The excitation source can be switched to a highly modulated light emitting diode, which is a much cheaper option [10]. The time gated detector we used in prototype III can be used for FD-FLIM [11].

## **6.4 Multiplexed Two-Photon Imaging**

### **6.4.1 Advantages and Limitations**

Two-photon (2P) fluorescence imaging of biological samples has gained tremendous importance in the last two decades [12]. 2P microscopy has enhanced imaging depth and is less damaging to samples. This imaging method enables the study of biological specimens, in three dimensions at high resolution. 3D tissue culture and in vivo imaging are gaining popularity since 2D cultures do not accurately represent how cells grow in the

body. Advances in two-photon imaging are being driven by the adoption of these 3D cell cultures models [13]. There is a growing need for faster two-photon scanning microscopes to image these complex disease models. Poland et al., have demonstrated that their multiplexed two-photon excitation system can achieve rapid imaging of live cells [14]. Their system deploys a spatial light modulator to multiplex the excitation beam (8×8 beamlets).

Our developed system can be easily configured to perform multiplexed two-photon imaging. This can be carried out by replacing the photon excitation source with a two-photon laser such as the Ti-Sapphire pulsed laser. Using two-photon excitation will remove the requirement for a pinhole array, or a pixel aperture to serve as a fixed set of pinholes. FLIM imaging can be carried using a time-gated or a TCSPC SPAD array.

Practically, there is a limitation on the degree of multiplexing that can be deployed with a two-photon excitation. To ensure that two photons will be simultaneously absorbed by a fluorophore, a significant amount of laser power must be used for excitation. Typical live cell imaging using two-photons requires a  $>1$  mW (measured at the objective per excitation spot) [15]. New diode-pumped Ti-Sapphire lasers can output 450-750 mW [16]. Thus, the degree of multiplexing can be limited by the output power of the laser source used.

#### **6.4.2 Two-Photon FLIM FRET**

Two-photon FLIM FRET imaging can also be achieved in our system. Interleaved excitation coupled to two-time gated/correlated detectors would be the ideal configuration. Interleaved excitation can be simply achieved by splitting the excitation source between two pathways. A delay can be added to one of the pathways. It must be equal to the half of the time between two consecutive pulses. One of the detectors will be in sync with the laser source, while the other is delayed by the same amount of interleaving delay. Interleaving will reduce the collection temporal window to half of its original size. For a Ti-Sapphire laser pulsed at 80 MHz, a non-interleaved window is 12.5 ns and it is half of that with an interleaved scheme. Thus, for imaging fluorescent proteins with lifetimes close to 4 ns, an incomplete decay model must be used to accurately estimate lifetime [17].

For non-interleaved imaging, donor emission in the acceptor channel must be estimated and corrected [18]. Although, the observed fluorescence lifetime and emission spectrum do not change with two-photon excitation [19], the absorption spectrum is broader [20]. This will lead to a larger degree of spectral cross-talk that must be accounted for.

#### **6.5 Future Applications of the Scanned Multibeam System**

The simplicity of the proposed multibeam generation and scanning approach, has large potential applications beyond confocal microscopy. Examples of such applications include multibeam stimulated emission depletion microscopy (STED) [21], multipoint FCS [22], and multibeam on-chip imaging [23]. In the next section, we will explore how our multiplexed system can be extended to perform super-resolution using a multibeam STED technique.

#### **6.5.1 Multibeam Fluorescence Correlation Spectroscopy**

FCS provides a biophysical approach to quantitatively measure important information from live cells [24], such as fluorophore concentration, diffusion coefficient, and molecular interactions. FCS is very sensitive technique and can be used to measure protein concentrations at endogenous levels (nanomolar concentrations can be measured) [25]. FCS could be used to characterize the protein expression map across different cellular organelles.

Like TCSPC, FCS requires the collection of enough photons to accurately reconstruct the autocorrelation function [26]. Thus, high resolution FCS measurements are not typically acquired. Instead, the user randomly chooses points at different parts of the cell and measures the particle count. Multibeam FCS will extend the spatial resolution of these particle count maps.

The accuracy of acquired FCS measurements depend on the experimentally determined size of the confocal volume [27]. FCS can be used to determine the effective size of the confocal volume. This is typically done by collecting correlation data from fluorophore solutions where either the diffusion coefficients or concentrations are known. FCS could be used to determine the effective confocal volumes in our multiplexed setup.

#### **6.5.2 Multibeam STED for Super-resolution**

Multibeam STED is a logical extension of the a multibeam confocal microscope. A STED microscope can be thought of as a confocal microscope with a depletion laser added to the optical path [28]. The purpose of the depletion laser is to minimize the illumination area at the imaging plane. This is achieved by shaping the depletion excitation into a doughnut like profile that surrounds the main excitation beam. The fluorescent molecules exposed to the depletion beam are switched off through stimulated emission. The detected photons are generated from the small excited point, at the center of the doughnut, where the depletion is not effective.

The doughnut shaped profile of the depletion laser is classically achieved using a phase retarding plate. These plates are typically designed to have spiral phase steps to introduce twisting of the light beam around the travel axis. When imaged on a plane, the observed intensity creates a doughnut like profile [29].

The most anticipated challenging aspect of a multibeam STED microscope, is the generation of a multiplexed depletion array that overlaps with the confocal excitation array. Görlitz and Guldbrand et al., have achieved a 3x3 STED multiplexing using a spatial light modulator, a mirror and a quarter wave plate (QWP) [30]. In their design, the helical phase profile is achieved by double passing the multiplexed depletion beams through the QWP.

Yan et al., have developed vortex fibres, specifically designed for STED imaging [31]. Their fibres are created using compact UV-written fibre-grating to generate orbital angular momentum of the electromagnetic wave passing through the fibre. Their design greatly simplifies the co-alignment of the excitation and the depletion beams. One possible way to leverage on their design, is to create a vortex fibre array coupled to an MLA to achieve multibeam STED imaging.

Another option for creating an array of vortexed excitation beams is through laser-induced metasurfaces to geometrically manipulate the light phase. Drevinskas et al., have demonstrated that they can use femtosecond lasers to alter the surface of a 300 nm thick a-Si:H films to create an array of micro-converters with polarization gratings [32]. The authors show how their micro-converter arrays can be used to generate an array of excitation beams with doughnut like profiles. These converter arrays represent a close cousin of the MLAs deployed in our design and can be used to extend our system to STED imaging.

It is worth noting that coupling the multiplexed signal to a time-gated SPAD can be used to perform time-gated STED imaging. Moffitt et al., have demonstrated that the spatial resolution of STED can be improved by encoding the spatial information in the fluorophore's lifetime. The authors have theoretically shown that the time gating excitation and detection can improve the spatial resolution by 50 %. This improvement is limited to fluorophores with lifetimes between 100ps to a few nanoseconds.

### **6.5.3 Multiple Detection Modules**

The work in this thesis different detectors can be used to collect different information about the generated fluorescence signal. Intensity-based measurements can be easily acquired using a simple off the shelf camera. High-temporal detectors such as the SPAD array can be used to collect fluorescence lifetime information.

Dimensionality of detected signal can be easily expanded to include spectral information. Adding a diffraction element prior to the detector can spectrally disperse the collected fluorescence signal. With our de-scanning solutions, multiplexed spectral imaging can be added as an additional detection module.

SPAD arrays are increasingly replacing standard detectors used in many microscopy applications [33]. Denser arrays with better time resolved performances are

actively being developed and manufactured. New signal collection geometries are now more possible than ever. The expansion of the SPAD technology will be a tremendous boost to our design. In fact, our lab is currently taking steps to building new prototypes where diffraction elements and dense SPAD arrays can be used to collect spectrally resolved fluorescence lifetime imaging [34].

## 6.6 Conclusion

Fluorescence lifetime imaging microscopy (FLIM) can be used to measure the interactions between full length proteins in their native cellular environment. It is a very powerful tool and it provides information about cellular responses caused by molecular changes. Although FLIM has been used to measure the efficacy of small molecules targeting certain protein-protein interactions (PPIs), current instruments do not meet the speed required for large scale screens. This thesis provides a potential solution. Successive improvements made in three prototypes, resulted in our creation of the Multiplexed focal Confocal system. This instrument can be used for rapid FLIM imaging of biological samples. In fact, we recorded data in less than 1 second. Extrapolating from this, we propose that our system is suitable for FLIM-FRET screening applications.

## References

1. Wilson, T. (2011). Resolution and optical sectioning in the confocal microscope. *Journal of microscopy*, 244(2), 113-121.
2. Shimozawa, T., Yamagata, K., Kondo, T., Hayashi, S., Shitamukai, A., Konno, D., ... & Kosugi, Y. (2013). Improving spinning disk confocal microscopy by preventing pinhole cross-talk for intravital imaging. *Proceedings of the National Academy of Sciences*, 110(9), 3399-3404.
3. Leica, “Live On Stage – Environmental Equipment for Leica Inverted and Upright Microscopes” May 2019 [online]  
[https://downloads.leica-microsystems.com/Leica%20DMi8%20for%20Live%20Cell%20Imaging/Brochures/Leica\\_Incubation\\_Systems-Brochure\\_EN.pdf](https://downloads.leica-microsystems.com/Leica%20DMi8%20for%20Live%20Cell%20Imaging/Brochures/Leica_Incubation_Systems-Brochure_EN.pdf)
4. Liu, Q., Leber, B., & Andrews, D. W. (2012). Interactions of pro-apoptotic BH3 proteins with anti-apoptotic Bcl-2 family proteins measured in live MCF-7 cells using FLIM FRET. *Cell Cycle*, 11(19), 3536-3542.
5. Leica, “Water Immersion Micro Dispenser – Automatic supply of water immersion during experiments” 2012. [online]  
[https://downloads.leica-microsystems.com/Leica%20Water%20Immersion%20Micro%20Dispenser/Brochures/Water\\_Immersion\\_Micro\\_Dispenser-Flyer\\_en.pdf](https://downloads.leica-microsystems.com/Leica%20Water%20Immersion%20Micro%20Dispenser/Brochures/Water_Immersion_Micro_Dispenser-Flyer_en.pdf)
6. Antolovic, I. M., Burri, S., Bruschini, C., Hoebe, R., & Charbon, E. (2015). Nonuniformity analysis of a 65-kpixel CMOS SPAD imager. *IEEE Transactions on Electron Devices*, 63(1), 57-64.
7. Ntziachristos, V., Bremer, C., & Weissleder, R. (2003). Fluorescence imaging with near-infrared light: new technological advances that enable in vivo molecular imaging. *European radiology*, 13(1), 195-208.
8. Kalyanov, A., Jiang, J., Lindner, S., Ahnen, L., di Costanzo, A., Pavia, J. M., ... & Wolf, M. (2018, April). Time Domain Near-Infrared Optical Tomography with Time-of-Flight SPAD Camera: The New Generation. In *Optical Tomography and Spectroscopy* (pp. OF4D-5). Optical Society of America.
9. Kagawa, K., Takasawa, T., Bo, Z., Seo, M. W., Imai, K., Yamamoto, J., ... & Kawahito, S. (2014, March). 10× 10-pixel 606kS/s multi-point fluorescence correlation spectroscopy CMOS image sensor. In *Imaging, Manipulation, and Analysis of Biomolecules, Cells, and Tissues XII* (Vol. 8947, p. 894713). International Society for Optics and Photonics.
10. Herman, P., Maliwal, B. P., Lin, H. J., & Lakowicz, J. R. (2001). Frequency-domain fluorescence microscopy with the LED as a light source. *Journal of Microscopy*, 203(2), 176-181.

11. Raspe, M., Kedziora, K. M., van den Broek, B., Zhao, Q., de Jong, S., Herz, J., ... & Jalink, K. (2016). siFLIM: single-image frequency-domain FLIM provides fast and photon-efficient lifetime data. *nature methods*, 13(6), 501.
12. Rakotoson, I., Delhomme, B., Djian, P., Deeg, A., Brunstein, M., Seebacher, C., ... & Oheim, M. (2019). Fast 3-D imaging of brain organoids with a new single-objective planar-illumination two-photon microscope. *Frontiers in neuroanatomy*, 13, 77.
13. Walsh, A. J., Castellanos, J. A., Nagathihalli, N. S., Merchant, N. B., & Skala, M. C. (2016). Optical imaging of drug-induced metabolism changes in murine and human pancreatic cancer organoids reveals heterogeneous drug response. *Pancreas*, 45(6), 863.
14. Poland, S. P., Krstajić, N., Monypenny, J., Coelho, S., Tyndall, D., Walker, R. J., ... & Li, D. D. U. (2015). A high speed multifocal multiphoton fluorescence lifetime imaging microscope for live-cell FRET imaging. *Biomedical optics express*, 6(2), 277-296.
15. Alexander, N. S., Palczewska, G., Stremplewski, P., Wojtkowski, M., Kern, T. S., & Palczewski, K. (2016). Image registration and averaging of low laser power two-photon fluorescence images of mouse retina. *Biomedical optics express*, 7(7), 2671-2691.
16. Gürel, K., Wittwer, V. J., Hoffmann, M., Saraceno, C. J., Hakobyan, S., Resan, B., ... & Südmeyer, T. (2015). Green-diode-pumped femtosecond Ti: Sapphire laser with up to 450 mW average power. *Optics express*, 23(23), 30043-30048.
17. Leung, R. W. K., Yeh, S. C. A., & Fang, Q. (2011). Effects of incomplete decay in fluorescence lifetime estimation. *Biomedical optics express*, 2(9), 2517-2531.
18. Wallrabe, H., & Periasamy, A. (2005). Imaging protein molecules using FRET and FLIM microscopy. *Current opinion in biotechnology*, 16(1), 19-27.
19. Volkmer, A., Subramaniam, V., Birch, D. J., & Jovin, T. M. (2000). One-and two-photon excited fluorescence lifetimes and anisotropy decays of green fluorescent proteins. *Biophysical journal*, 78(3), 1589-1598.
20. Stoltzfus, C. R., Barnett, L. M., Drobizhev, M., Wicks, G., Mikhaylov, A., Hughes, T. E., & Rebane, A. (2015). Two-photon directed evolution of green fluorescent proteins. *Scientific reports*, 5, 11968.
21. Vicidomini, G., Bianchini, P., & Diaspro, A. (2018). STED super-resolved microscopy. *Nature methods*, 15(3), 173.
22. Goda, K., Ayazi, A., Gossett, D. R., Sadasivam, J., Lonappan, C. K., Sollier, E., ... & Wang, C. (2012). High-throughput single-microparticle imaging flow analyzer. *Proceedings of the National Academy of Sciences*, 109(29), 11630-11635.
23. Peel, S., Corrigan, A. M., Ehrhardt, B., Jang, K. J., Caetano-Pinto, P., Boeckeler, M., ... & Kulkarni, G. (2019). Introducing an automated high content confocal imaging approach for Organs-on-Chips. *Lab on a Chip*, 19(3), 410-421.
24. Krichevsky, O., & Bonnet, G. (2002). Fluorescence correlation spectroscopy: the technique and its applications. *Reports on Progress in Physics*, 65(2), 251.
25. Mahen, R., Koch, B., Wachsmuth, M., Politi, A. Z., Perez-Gonzalez, A., Mergenthaler, J., ... & Ellenberg, J. (2014). Comparative assessment of fluorescent transgene methods

- for quantitative imaging in human cells. *Molecular biology of the cell*, 25(22), 3610-3618.
26. Li, D. U., Tyndall, D., Walker, R., Richardson, J. A., Henderson, R. K., Arlt, J., ... & Charbon, E. (2011). Video-rate fluorescence lifetime imaging camera with CMOS single-photon avalanche diode arrays and high-speed imaging algorithm. *Journal of biomedical optics*, 16(9), 096012.
  27. Buschmann, V., Krämer, B., Koberling, F., Macdonald, R., & Rättinger, S. (2009). Quantitative FCS: determination of the confocal volume by FCS and bead scanning with the microtime 200. Application Note PicoQuant GmbH, Berlin.
  28. Inavalli, VVG Krishna, et al. "A super-resolution platform for correlative live single-molecule imaging and STED microscopy." *Nature methods* 16.12 (2019): 1263-1268.
  29. Barboza, R., Bortolozzo, U., Clerc, M. G., Residori, S., & Vidal-Henriquez, E. (2015). Optical vortex induction via light-matter interaction in liquid-crystal media. *Advances in Optics and Photonics*, 7(3), 635-683.
  30. Görlitz, F., Guldbrand, S., Runcorn, T. H., Murray, R. T., Jaso-Tamame, A. L., Sinclair, H. G., ... & French, P. M. (2018). easySLM-STED: Stimulated emission depletion microscopy with aberration correction, extended field of view and multiple beam scanning. *Journal of biophotonics*, 11(11), e201800087.
  31. Yan, L., Kristensen, P., & Ramachandran, S. (2019). Vortex fibers for STED microscopy. *APL Photonics*, 4(2), 022903.
  32. Drevinskas, R., Beresna, M., Zhang, J., Kazanskii, A. G., & Kazansky, P. G. (2017). Ultrafast laser-induced metasurfaces for geometric phase manipulation. *Advanced Optical Materials*, 5(1), 1600575.
  33. Castello, M., Tortarolo, G., Buttafava, M., Deguchi, T., Villa, F., Koho, S., ... & Vicidomini, G. (2018). Image scanning microscopy with single-photon detector array. *bioRxiv*, 335596.
  34. Lagarto, J. L., Credi, C., Villa, F., Tisa, S., Zappa, F., Shcheslavskiy, V., ... & Cicchi, R. (2019). Multispectral Depth-Resolved Fluorescence Lifetime Spectroscopy Using SPAD Array Detectors and Fiber Probes. *Sensors*, 19(12), 2678.

## **Appendix A - Coupling dynamic segmentation with the phasor approach of lifetime estimation for fast and quantitative analysis of large FLIM-FRET datasets**

Even with multiplexing and fast FLIM imaging, we are still only collecting a few hundred photons per pixel. To include sufficient photons for decay analysis, the nearest neighbour binning approach is most commonly used; at each pixel the decay is reconstructed by binning photons from neighbouring pixels. In most commercial systems and automated analysis regions of interest are then overlaid on this constructed "FLIM image" and within that region of interest (ROI) the average lifetime is calculated.

Here we propose ROI selection prior to pixel binning is a superior method of analysis for 3 reasons:

1. Pixels that contribute to the decay belong to the sub cellular region analyzed.
2. Time of analysis is significantly reduced because fitting is most computationally expensive step.
3. Each region of interest contains high photon counts which can be fit to more suitable, complex mathematical models.

We combine this ROI selection with the Phasor approach for fit-free analysis of complex lifetime decays.

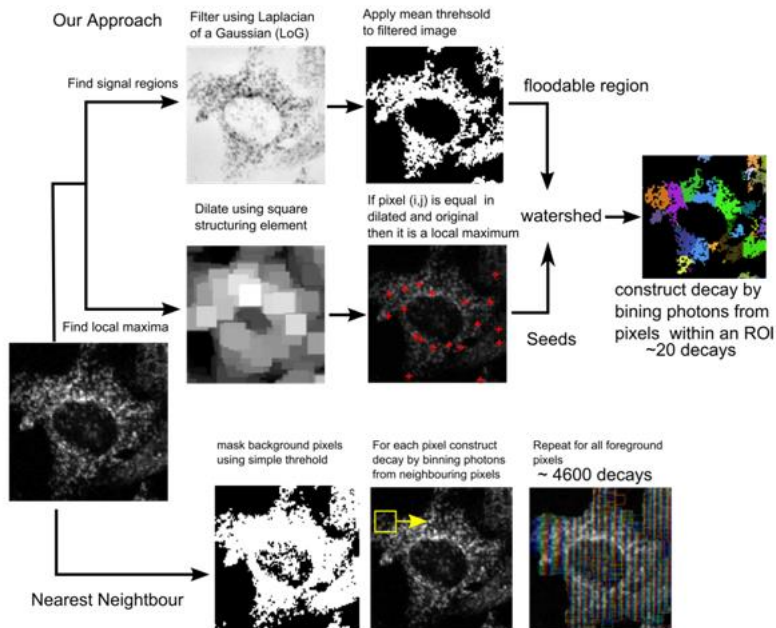


**Fig 1-** Our segmentation approach which uses seed controlled watershed algorithm. I have also shown the commonly used nearest neighbour binning approach for comparison purposes.

Here we want to demonstrate how a simple segmentation approach (using structural information) can be used to extract sub cellular ROIs. The decays are generated by binning photon counts for pixels within the same region. This generated well sampled decays which can be analyzed to determine the bound fraction (see Figure 2).

In essence this is a global bound fraction estimation using all the decays extracted from a single well (fit free and computationally inexpensive). Since our decays are very well sampled, the Phasor shows a nice linear distribution which can be easily fit to a line. The distance along the line in the phasor space is the measure of bound fraction within an ROI.

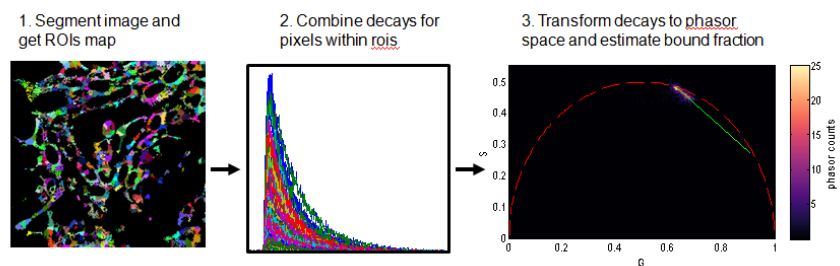


**Fig 2.** Rapid fit free analysis for large data sets. Decays are constructed by combining photon histograms from pixels belonging to each ROI. A Fourier transform of each decay is used to get a phasor representation of the decays. Phasor analysis is used to extract donor bound fraction.

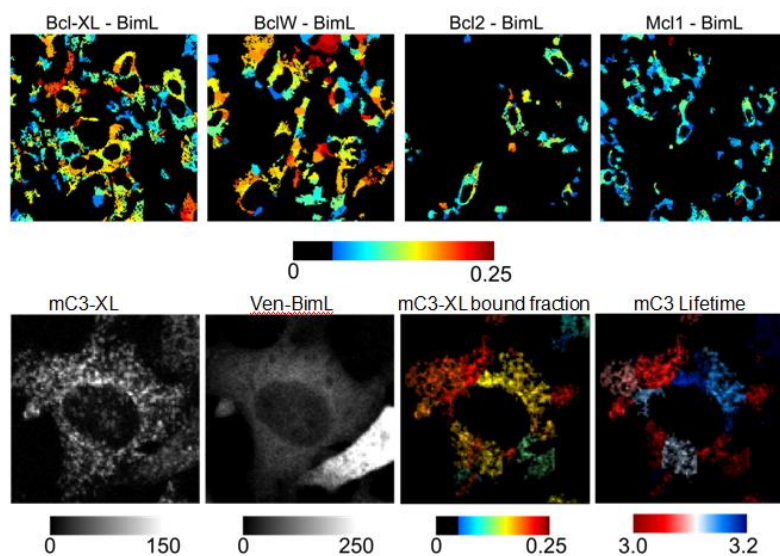


**Fig 3.** Sample and cell level variation in Bcl-2 bound complexes. Bound fractions can be used to reconstruct semi-quantitative binding curves for several Bcl-2 PPIs. Bound complex fraction is plotted as a function of acceptor intensity

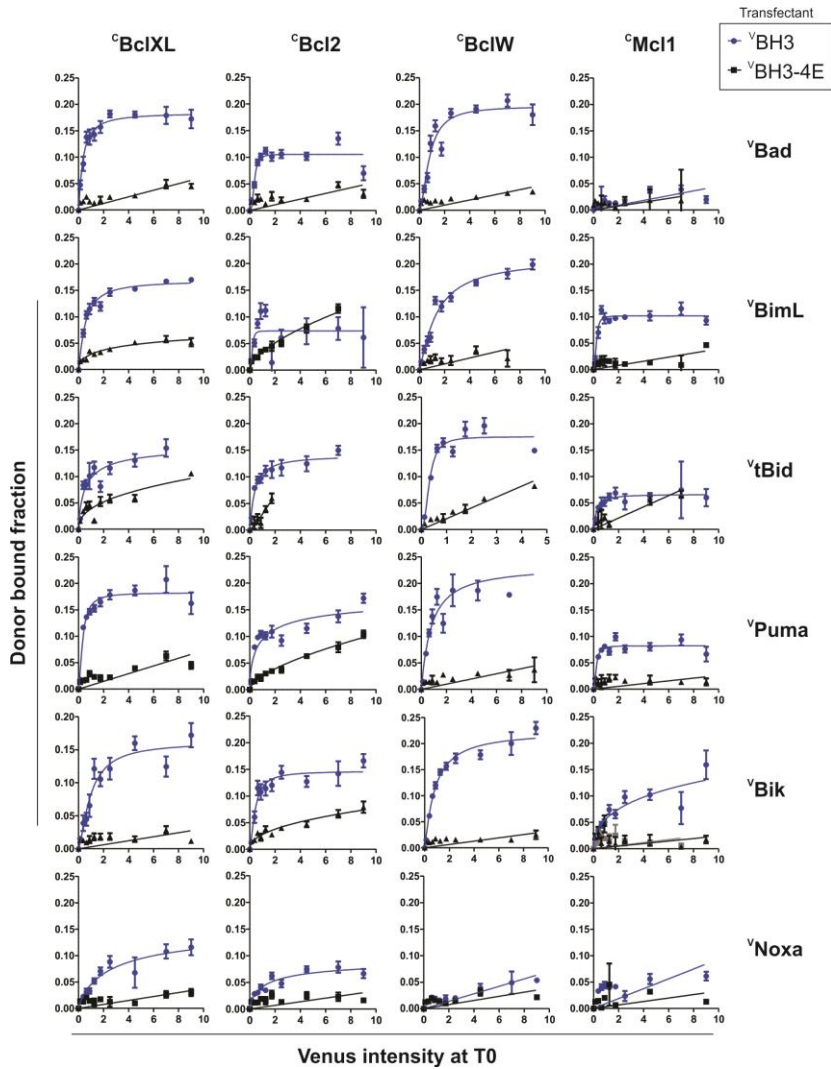


**Fig 4.** Semi-quantitative binding curves of 24 unique protein-protein complexes measured in live cells. 4 different cell lines: BMKd3 expressing  $^c$ BclXL,  $^c$ Bcl2,  $^c$ BclW or  $^c$ MCL1 were transiently transfected with  $^v$ BH3 proteins listed on the right panel. For each BH3 protein (Blue curves), a '4E' mutation was made in the BH3 domain which is known to disrupt binding between Bcl2 family proteins (black curves). Data was plotted in Graphpad Prism and fit to a linear or to a Hill Slope equation depending on the goodness of fit.

## **Appendix B – Effect of photobleaching on fused mCerulean3 fluorescent protein in live cells**

Excitation sources in the range of 430-470 are typically used to excite the mCerulean3 fluorescent protein. Blue range excitation can also excite endogenous proteins and result in autofluorescence generation. In most cases, the fluorescent photons generated are orders of magnitude larger than the photons generated through autofluorescence. Thus, their contribution to the overall estimated lifetime is negligible. However, this assumption does not hold true when the excitation power is increased (perhaps to image faster, or gain more photons). High excitation power photobleaches the fluorescent protein and increases the autofluorescence contribution, which will lead to underestimation of the fluorescence lifetime.

Prior to any FLIM-FRET experiments, we determine this power threshold to ensure that our sample will not photobleach. For our live cell samples (BMK, HEK293 and MCF-7) expressing mCerulean3-Bcl-Xl we have determined that the laser power should remain at  $<5\mu\text{W}$  (on average) measured at the objective. For multiplexed confocal systems, this measurement should be determined for a single excitation spot (total power/number of foci). Here we present some of these measurements collected on a single point confocal system (ISS-Alba) and demonstrate the effect of photobleaching on mCerulean3-Bcl-XL expressed in live MCF-7 cells. We examine changes in intensity and estimated lifetime as a function of laser power and pixel dwell time.

It is important to note that this threshold was calculated for single scan in a field of view. For multiple scan imaging (temporal FLIM), the power should be significantly reduced.

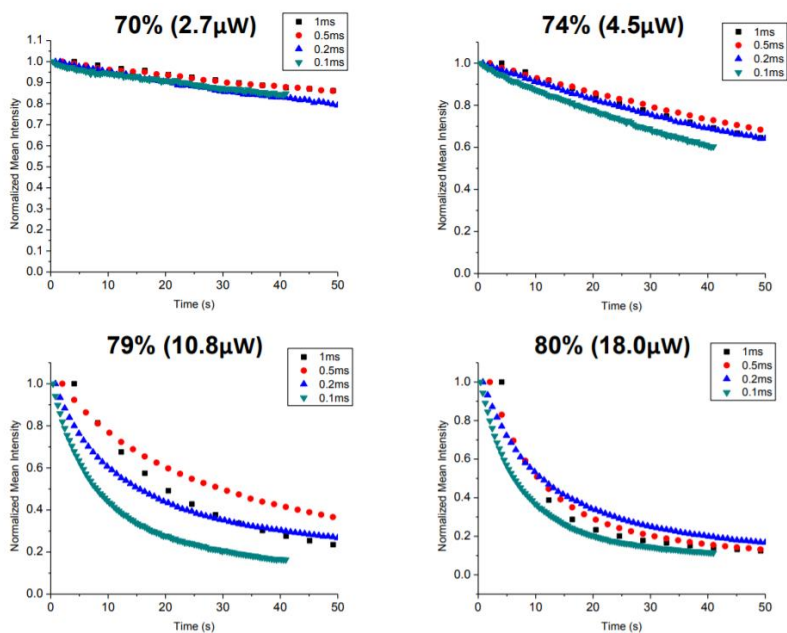


**Fig 1.** Effect of photobleaching on the intensity of mCerulean3-Bcl-XL expressed in live MCF-7. For single image acquisition (first few scans) at 4.5μW the normalized intensity is very close to 1.0.

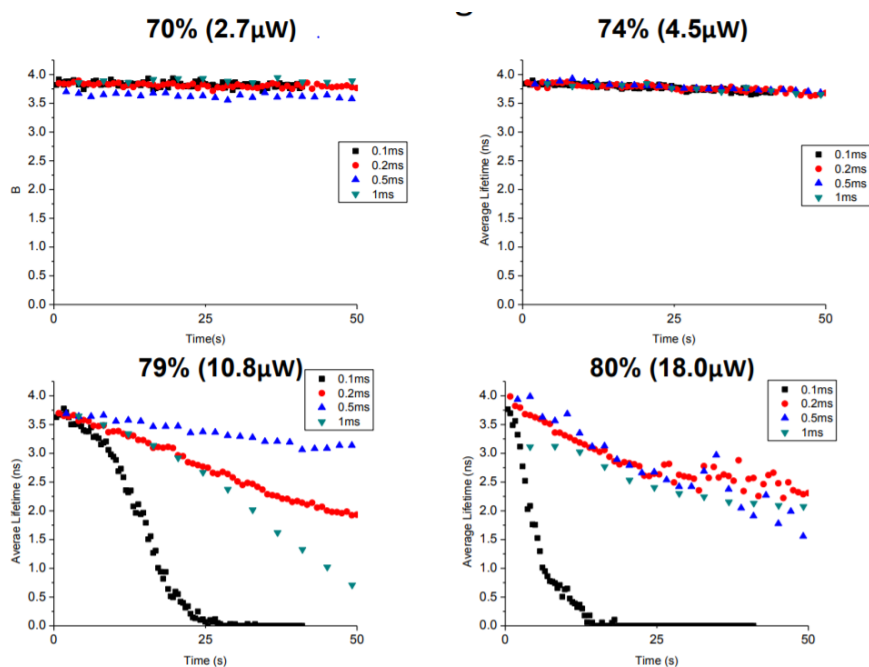


**Fig 2.** Effect of photobleaching on the lifetime of mCerulean3-Bcl-XL expressed in live MCF-7. For multiple image acquisition at 4.5  $\mu\text{W}$  the fluorescence lifetime measured for mCerulean3 remains at 3.8 nanoseconds.

## Appendix C – Properties of Refractive Window Scanners

Scanning in most single point confocal microscopes is performed using mirror galvanometers. These orthogonal mirrors are used to change the light beam trajectory in a raster mode. The lateral shift for mirror scanners is linearly proportional to the tilt angle:

$$\Delta d \cong 2f\phi \quad (\text{Appendix C Eq.1})$$

Where  $f$  is the focal length of the focusing lens,  $\Delta d$  is the lateral shift, and  $\phi$  is the tilt angle. Mirror-based galvanometers can be used to scan multibeam arrays. However, this must be done while the beams are collimated, which requires additional two lenses prior to the scanning unit.

For multibeam scanning using a mirror-based scanner, linear approximation between the tilt angle and the lateral shift is no longer appropriate. A portion of the beams will have a larger incident angle to the normal of the mirror surface and will result in non-linear scanning. Several solutions have been developed to mitigate this non-linearity scanning effect. However, these corrections lead to additional optical elements and more complex arrangements.

Refractive window scanners provide a simple solution for scanning multibeam arrays. These scanners don't require additional lenses to collimate the beams, and maintain linearity between the tilt angle ( $\phi$ ) and the lateral shift ( $\Delta d$ ).

$$\Delta d \cong \phi \cdot t \cdot \left(\frac{n-1}{n}\right) \quad (\text{Appendix C Eq.2})$$

Where  $n$  is the refractive index of the window material and  $t$  is the thickness of the refractive window.

It is worth noting that the small angle approximation is only valid for small tilt angles. For highly multiplexed beam arrays, such as the ones used in our prototypes, this approximation remains valid. For cases where the required shift per excitation beam is large, refractive window scanners suffer from the nonlinearity effect as well.

Our refractive windows are made of fused silica, which has a low chromatic dispersion in the visible range. For the window parameters selected, excitation light at 440 nm ( $n = 1.46635$ ) will allow  $\pm 250 \mu\text{m}$  at  $8.92^\circ$ .

In our system, we use the 6230H galvanometer scanners from Cambridge Technology. These scanners can operate at 8 KHz oscillation frequency, have a 99.99 % linear linearity over  $20^\circ$ , and can support load weight up to 267 grams. Our current scanning is done at a  $30 \times 30$  steps. Our Live cell imaging is performed at 50 microseconds pixel dwell time. The scanners are now operating in a “step and hold” mode. For continuous scanning,

at the same pixel dwell time, will result in scan oscillation at 330 Hz. This is way below the capacity of the resonant scanners.